Structure Function Paradigms of Organic Electrooptic Materials

Peter V Johnston

A dissertation
submitted in partial fulfillment of the
requirements for the degree of

Doctor of Philosophy

University of Washington

2016

Reading Committee:

Gary Drobny, Chair

Dennis (Mike) Heinekey

Rob Synovec

Program Authorized to Offer Degree:
Chemistry

University of Washington

Abstract

Structure Function Paradigms of Organic Electrooptic Materials

Peter V Johnston

Chair of the Supervisory Committee:
Professor of Chemistry Gary Drobny
Chemistry

Organic Electrooptic Materials have been demonstrated and commercialized as active components in telecommunications systems. Application of organic materials to electrooptic switching devices could result in large gains in terms of size weight and power figures of merit. This is because organic materials exhibit large electrooptic coefficients, ultra-fast femto-second response times, submicron chipscale integration, and highly tunable absorption via synthetic manipulation of the sp^2 hybridized π system responsible for electroopic response; however, due in part to deficiencies in thermal stability and preferential non-centrosymmetric bulk-phase ordering, these materials have not been able to overcome engineering barriers to realize their full potential. This work approaches the problem of thermal stability by invoking structure function paradigms of organic materials and re-engineering existing molecular structures with large electrooptic response for improved device performance. Incremental changes in molecular structure are observed to have significant effects on glass transition temperature, poling efficiency, maximum electrooptic coefficent, and device conductance, with minimal changes in optical properties in the bulk phase. A notable increase in glass transition temperature with no significant reduction in electrooptic response is observed. [1] Solid-state device engineering concepts to eliminate unwanted current during the poling process are presented with experimental evidence to support the efficacy of reducing current, and thus increasing the electric field, during poling. [2] Real device measurements are also included to demonstrate the full potential of state-of-the art materials. [3]

TABLE OF CONTENTS

LIST OF FIGURES

LIST OF TABLES

ACKNOWLEDGMENTS

In addition to recognizing the unending patience and guidance of Gary Drobny, Phil Reid, Larry Dalton, Bruce Robinson, Delwin Elder, Paul Hopkins, and Christine Luscombe. I'd also like to express sincere appreciation to Amanda Myhre, Carrie DeMartini, Treg Isaacson, and Michaela Wehner; the Skagit Valley College and the Skagit Valley College Foundation, the McIntyre Family; the Western Washington University Department of Chemistry and the University of Washington Department of Chemistry, especially Gojko Lalic, Steven Matthews, Betsy Raymond, Tim Clark, Dan Gamelin and all of the staff, post-doctoral, graduate, and undergraduate students who collaborated in this body of research especially, Denise Bale, Ilya Kosilken, Meghana Rawal, Andreas Tillack, Kerry Garret, Jinsheng Song, Nathan Phillips-Sylvain, Colin Tang, Sol Kim, Anthony Fok, Uyen Tram, Vivianna Gonzales, Roberto Gonzales, and William Prabowo. Additionally I would like to thank the Koos group, the Karlsruhe Institute of Technology, and the Institute of Electromagnetic Fields. This material is based upon work supported by the National Science Foundation under Grant Number (DMR-1303080, DMR-1005819, and DMR-0120967). Any opinions, findings, and conclusions or recommendations expressed in this material are those of the author(s) and do not necessarily reflect the views of the National Science Foundation. The authors acknowledge partial financial support from the Air Force Office of Scientific Research (FA9550-10-1-0558, FA9550-15-1-0319, and FA9550-09-1- 0682).

DEDICATION

for Jin Wenwei

Chapter 1

INTRODUCTION TO ORGANIC ELECTROOPTIC MATERIALS FOR TELECOMMUNICATIONS

1.1 Organic Eectrooptics for Telecommunications

1.1.1 Global Telecommunication

Global Telecommunication (telecom) in the 21st century is limited by the efficacy of the materials and systems that facilitate electrical-optical-electrical signal transduction. The telecom network stands today as a conglomeration of transcontinental optical cables and venerable copper-wire telephone technologies, the latter of which are rapidly being phased out in order to meet increasing demand for high-speed bandwidth. The need for electrooptic (EO) transduction is both a result of a co-evolution of technology with infrastructure, and the various conveniences and limitations of electrical versus optical signal carriers and processors. Unlike electronics, guided optical communications offers very large bandwidth, low long-range attenuation, and predictable performance over very large distances; however, short-range information processing and storage needs are most conveniently met with electronics. Electrooptic materials (EOM) are thus required as active components in telecommunication systems to seamlessly integrate electronic devices and optical networks into a global communication platform. [6–9]

1.1.2 Limitations of Current Technologies

Electrical to optical signal transduction can be explained in terms of modulation of an optical signal by an applied DC electric field. Intensity, phase, and polarization of an optical field can all be modulated through a change of the material properties with respect to the applied field.

The Mach-Zehnder interferometer is one example of an intensity modulation device. [10] In such a device the signal beam is concentrated into a waveguide structure comprised of

the EO material. The path of the waveguide is split into two channels where a DC field is applied, causing a change of the index of refraction of the material. The voltage required to off set the phases of light in each channel such that a maximum destructive interference is observed, V_π, is the voltage that coresponds to a phase shift of π; at this voltage when the two channels are recombined into a single waveguide the result is destructive interference. Such a device can be used to modulate the intensity of light as it travels through the waveguide structure, and this change in intensity is then translated as a binary 1 or 0 digital output, often referred to as on-off keying. [6]

1.1.3 Lithium Niobate and Other Current Technologies

The current commercial EOM of choice for telecommunications applications is lithium niobate ($LiNbO_3$). There are also several commercially available organic and inorganic electrooptic crystals, including beta barium borate (BaB_2O_4), lithium triborate (LiB_3O_5), potassium dideuterium phosphate (KDP), and 4-N,N-dimethylamino-4'-N'-methyl-stilbazolium tosylate (DAST) to name a few. The organic materials found in this work are intended to be incorporated into a device as an amorphous film (i.e., non-crystalline), and are similar in molecular structure to materials that have already been commercialized by companies such as Lumera, Soluxra, and Gigoptix; however, at the time of writing this, it is likely that these products have not reached the level of commercial success enjoyed by $LiNbO_3$. The success of $LiNbO_3$ is largely based on it's robust and transparent character. $LiNbO_3$ is an inorganic crystalline material and must be recrystallized from a melt at temperatures above 1257 °C (far above device operating temperatures). The crystal must then be carefully cut into thin chip-scale sized wafers, polished, and painstakingly placed into an EO device; this process makes it quite difficult to scale down device footprints beyond the limitations of the mechanical component required to assemble a device in this way. Additionally, due to the very high dielectric constant, velocity mismatch is problematic. EO response is high compared to other crystalline materials, but low compared to state of the art OEMs. The EO activity of $LiNbO_3$ is related to movement of ions within the crystal lattice at rates measurable in milliseconds. These limitations all result in suboptimal device path-lengths

on the order of 10 cm. Yet, despite its limitations, $LiNbO_3$ is favored commercially, because it is highly stable at device operating temperatures, and has little or no absorption at telecom wavelengths, and because industry has developed around these limitations. $LiNbO_3$ is sturdy and predictable but cannot sustain demand for more bandwith. The bandwidth crisis associated with the first internet boom in the late 1990s and early 2000s was largely ameliorated with clever engineering such as wave division multiplexing, but as demand for band width continues to grow and both consumer and military applications require more and faster data transfer by smaller and lighter devices we are approaching another bandwidth bottle-neck. $LiNbO_3$ has reached the limit of efficacy in terms of chip-scale and power consumption, and will simply not meet projected demand due to inferior EO susceptibility, velocity mismatch and rigid processing requirements described above. [6, 11] The increasing trend in global demand for smaller, faster, more energy efficient commercial communication devices inevitably leads to the discussion of organic materials.

1.1.4 Advantage, Trade-offs, and Evolution of Organics

OEMs display significant advantages over their inorganic analogues in terms of processing, fabrication, and device operation. OEMs can be solution processed and spun cast onto devices, circumventing the need for high temperature melt crystallization, cutting, polishing, etc., and thus allowing for even smaller chip foot prints. The optical and mechanical properties of organic materials are highly tunable for specific device applications, architectures, and fabrication methods through alteration of the molecular and resulting supermolecular structure. Under optimal poling conditions the highest performing OEMs have been shown to have EO activity over an order of magnitude larger than that of $LiNbO_3$. Electrooptic activity of OEMs is a result of perturbing the π electron system, which is measurable in terms of femtoseconds, orders of magnitude faster than the ionic motions of lattice elements responsible for EO response in $LiNbO_3$; this translates to broader bandwidth, lower power consumption per bit, smaller device footprints, and more flexibility with regards to processing methods than commercial inorganic materials. [12] Additionally, lower dielectric constants of organic materials translates to better velocity matching which in turn trans-

lates to less complex device structures. It's actually quite amazing, considering all of these exciting features of OEMs, that there has not been a revolution in the industry already.

1.1.5 Challenges in Developing High Performance Organic Electrooptic Materials

Despite the various advantages listed above, $LiNbO_3$ remains the most widely used commercial material; several major challenges remain for OEMs. Absorption at telecom wavelengths can sometimes be problematic and must be considered. More problematic however, is that organics with spectacular molecular nonlinearity generally do form acentric crystals, and therefore must be processed in a manner that traps them in an amorphous state, and then poled at elevated temperatures in an electric field to introduce the requisite acentric order of the bulk phase. [2,12–15] Poling organic material in a device can be experimentally challenging and, if the glass transition temperature, T_g, of the OEM is near or below the operating temperature of the device, the material will undergo catastrophic *in-situ* de-poling. To break the commercial barrier and surpass the commercial success of $LiNbO_3$, OEMs must be both high-performing and thermally robust.

1.1.6 Historical Advances

Early research into OEMs was limited to acentric crystalline materials. [16, 17] In the 1980s it was realized that organic molecules with large optical nonlinearity (chromophores) could be doped into an organic polymer and oriented in an electric field at or near the T_g of the polymer. [18, 19] Doping a chromophore into an amorphous plastic host eliminated the need to grow acentric crystals as well as the phonon absorption associated with lattice interactions observed in crystalline materials, and served as a platform to minimize inter-chromophore interactions through the concept of loading density and site isolation. Doping molecules into a polymer host allowed the study of molecules with increased dipoles and non-centrosymmetric crystal structures.

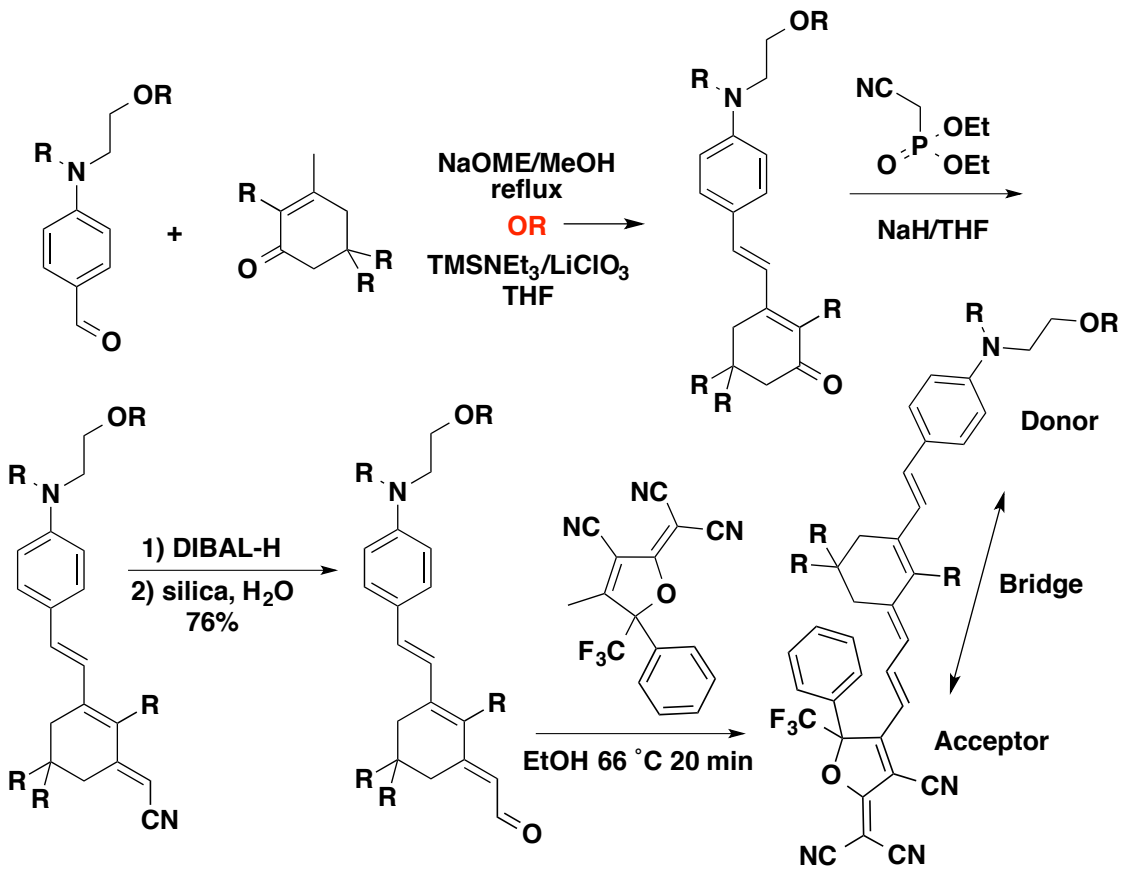

Figure 1.1: The general synthesis of CLD class chromophores.Inverse doping is carried out by substitution at the R positions with various functional groups taken from polymers or small molecules with desirable traits such as high T_g or transparency at specific wavelengths.

Inverse Doping of Polymeric Materials Onto Chromophore Structures

In the early 2000s the prevalent paradigm was that EO chromophores required a host material. Host materials included polymethyl methacrylate (PMMA) or poly-carbonate (APC or BPC) among other more exotic specialized host systems. [5] The polymer host served two functions. First, it provided a matrix to isolate chromophores from one another and thus reduce intermolecular interactions that favor non-centrosymmertic ordering (referred to as site isolation effects). Second, the host provided stability and transparency required for device fabrication and operation. [20, 21] By 2010 monolithic and binary chromophore molecular glasses were demonstrated as high performance EO materials that did not require a host; however, this was often at the expense of both conductivity and thermal stability. [22–24] The increase in EO activity and poling efficiency achieved by removing the polymer host from the system can be largely attributed to dramatic increases in number density. These and other figures of merit can be further enhanced by careful engineering of the molecular structure exterior to the chromophores electronic structure. Additionally, poling of monolithic materials allow for probing of the intrinsic properties of the chromophore, which may be valuable information relative to our understanding of guest-host systems.

Intelligent inverse doping is carried out by invocation of structure function paradigms in organic materials via the addition of moieties covalently linked to the chromophore at various synthetically accessible attachment points (figure 1.1), provided that those moieties induce energetically favorable acentric order, increase thermal stability, increase localized fields, and reduce leakage current during poling. Individual molecular subunits of polymeric materials with high T_g can be incorporated into the molecular structure of an electrooptic chromophore and the resulting material will likely have a higher T_g. Individual molecular subunits of polymeric materials with low conductivity can be incorporated into the molecular structure of a high-beta chromophore and the resulting material will likely have a lower conductivity. One must simply look towards the literature for organic polymers with the desirable traits and master the synthetic process required to produce a hybrid material. This approach has been proven to lead to higher number density materials with improved ordering and increased thermal stability as well as increased polarization at the T_g; indeed,

while there are many parameters that can be affected by this approach, some monolithic materials have been reported to have improved order over others. [22,23,25] While it is desirable to eliminate unnecessary fabrication steps, material properties of monolithic materials can be further improved post-poling through lattice-hardening via the introduction of cross linkable moieties, but this is also a matter of invoking structure function paradigms with the additional consideration of post-polarization reactivity. [22, 24, 26]

1.1.7 Overcoming Challenges in Device Integration

As mentioned above, $LiNbO_3$ is challenging to incorporate into devices with exceedingly small foot prints. OEMs also face challenges in terms of device fabrication and integration.

Solution processing is a highly favorable trait. The organic material is readily dissolved in an appropriate organic solvent and applied to a surface with wave-guiding features, such as silicon strip or slot waveguide (figure 4.1). The resulting film is then dried *in vaccuo*. In this way organic material can be applied to slot waveguides as small as 40 nm in width, [27] that is at least 32 times smaller than the wavelength of the light in the slot! Spin casting from solution phase, however, generally results in an isotropic material with no second-order electrooptic response. Low melt-temp acentric organic crystals have been deployed [28], but to date chromophores with very large molecular electrooptic response are, with a few exceptions, found to crystallize in a centrosymmetric fashion, if they display a crystal phase at all. [22, 29, 30] For these reasons it is necessary to pole OEMs at the material's T_g. This problematic fabrication step has often led researchers to discrepancies regarding the efficacy of one material as it pertains to multiple unique device architectures. The requisite poling temperature and depoling temperature figures of merit are governed by the preferred (or available) fabrication methods and the device operating temperature respectively.

The intrinsic electronic properties of the material deployed as the electrodes, the distance in which the field is distributed, and additional fabrication requirements (such as cure temp or the introduction of cladding layers) must all be considered before a novel material can be launched commercially.

Maximizing acentric order and minimizing optical loss in materials with exceptionally

large EO susceptibilities while maintaining the desired mechanical and optical properties required for device fabrication and functionality are crucial to the commercial viability of organic EO materials over inorganic EO materials like $LiNbO_3$. The chapters that follow demonstrate experimental control over material properties through synthetic modification of known chromophore structures (chapter 2), address the issues of conductivity during poling as a device engineering issue (chapter 3), and give examples of real working devices that incorporate organic EO materials (chapter 4).

Chapter 2

STRUCTURE-FUNCTION RELATIONSHIP EXPLORATION FOR ENHANCED THERMAL STABILITY AND ELECTRO-OPTIC ACTIVITY IN MONOLITHIC ORGANIC NLO CHROMOPHORES [1]

2.1 Abstract

We have developed a series of novel monolithic materials based on molecules previously explored as dopants in guest-host systems to study intrinsic structure-function relationships in organic electro-optic (EO) materials. In a library of EO molecules with varied bridge segments, molecular modification of the donor with bis(tert-butyldiphenylsilyl) groups led to improvement in formation of amorphous films and led to enhanced poling efficiency. Further modification to include a carbazole site-isolation group on the bridge effectively reduced intermolecular interactions, led to a material with poling efficiency of approximately 3 $(nm/V)^2$, and an increased glass transition temperature to 20-40 °C higher than similar reported monolithic materials. This level of thermal stability is comparable to common guest/host systems, which incorporated poly(methyl methacrylate) (PMMA) as the host. Our research showed that π-bridge length and type impacted first molecular hyperpolarizability, β, of a chromophore, which is accordingly reflected in the EO response. These findings further promote the utility of monolithic materials for their increased EO behavior and improved thermal stability, making this material system a competitor of guest-host systems in commercial applications.[http://dx.doi.org/10.1039/C6TC00358C]

2.2 Introduction

Decades of research have resulted in structure-function paradigms regarding organic electro-optic (EO) materials, [24, 31–33] a critical component of optoelectronic devices for telecommunications, computing and sensing. [34–37] Molecular structures that give rise to large optical nonlinearity have been developed; however, one major challenge is the realization of large EO coefficients (r_{33}) when integrating glassy materials with large molecular hyperpo-

larizability (β) into a real device architecture. Several parameters should be improved for optimum r_{33}: β, number density (ρ_N) and acentric order ($\langle\cos^3\theta\rangle$). When acentric order is introduced by electric field poling, [19, 38] strong dipole-dipole interactions among chromophores must be minimized to optimize $\langle\cos^3\theta\rangle$. [39, 40] Guest-host material systems were heavily utilized in organic EO materials research previously. [20, 23] Such systems allow the EO chromophore to be diluted in a polymer host, which minimizes the interchromophore electrostatic attraction and allows for higher $\langle\cos^3\theta\rangle$ during electric field poling. The chromophore loading in guest-host systems is typically $\sim$25 wt%; however, increasing ρ_N is desirable if the product $\rho_N\langle\cos^3\theta\rangle$ is to be increased. The limitation of r_{33} associated with guest-host systems motivates further investigation of improved EO materials with maximized $\rho_N\langle\cos^3\theta\rangle$.

Monolithic-chromophore molecular glasses, with the host polymer entirely removed yet the chromophore remaining amorphous, have shown promising EO performance in the state-of-the-art silicon-organic hybrid (SOH) and plasmonic-organic hybrid (POH) modulators. [3, 25, 41–44] Recent studies have confirmed effective approaches to increase acentric order of such high number-density ($\rho_N > 4 \times 10^{20} molecules/cm^3$) materials, leading to greatly improved $\rho_N\langle\cos^3\theta\rangle$. One of these approaches takes advantage of self-assembling side chains (e.g. aryl-perfluoroaryl units or coumarin-based mesogens) attached to the chromophore that can cooperatively interact through introduced dipolar or quadrupolar interactions. [45–49] However, these chromophore modifications and absence of polymer host can result in a lower than desirable glass transition temperature (T_g), which should be improved to satisfy Telcordia standards for EO telecom switching devices. [50] A second approach takes advantage of a design feature that relies on bulky bis(tert-butyldiphenylsilyl) bis(TBDPS) functional groups on the donor end of the chromophore. A recent study showed that a simple modification of the donor of a benchmark CLD-class chromophore, [51] -switching from tert-butyl-dimethy-silyl (TBDMS) ether functional groups to TBDPS-resulted in a new monolithic material (JRD1) able to achieve an extraordinarily high EO activity of $r_{33} \sim 500$ pm/V. [2] This paper builds on that concept. New monolithic chromophores with the same bis(TBDPS)-containing donor units have been designed, synthesized, and analyzed. Enhanced EO activity as well as improved thermal stability is pursued. The effect of bridge

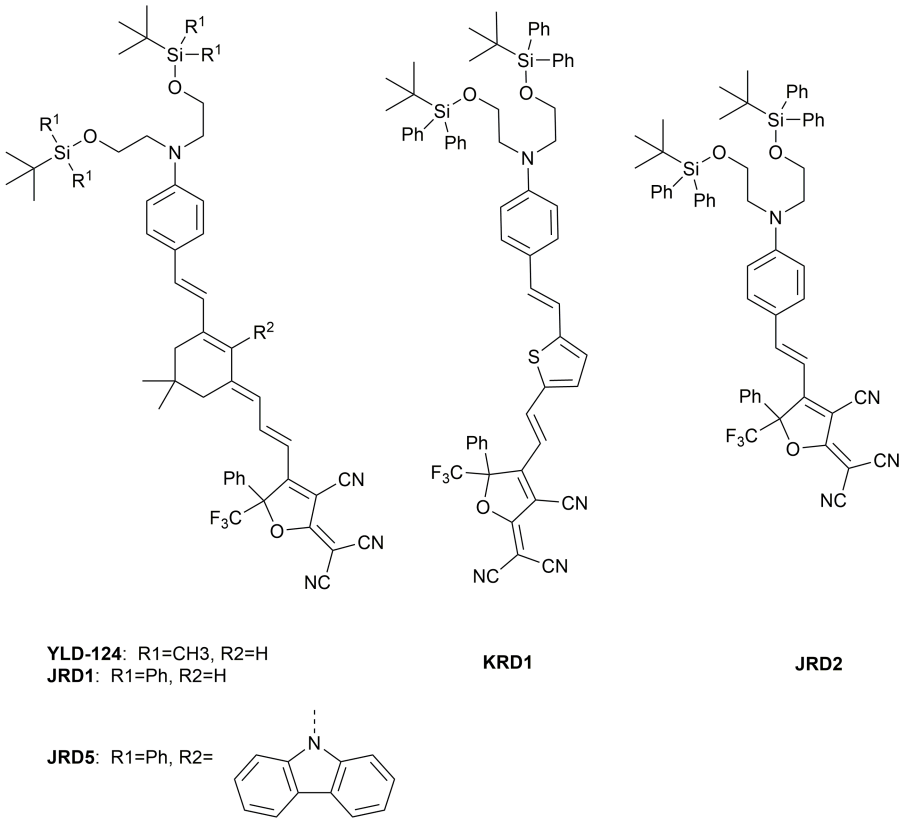

Figure 2.1: A series of EO chromophores studied in this paper.

substitution and different bridge types on EO performance, T_g, thermal stability, and film quality will be discussed.

The structures of the chromophores for this study (Figure 2.1) all have a dialkylarylamino electron donor and a tricyanofuran (TCF) electron acceptor connected by a π-conjugated bridge. Our earlier work [2] demonstrated the feasibility of using YLD-124 as a neat chromophore; whereas previously, it was thought that YLD-124 needed to be doped into a polymer host to form stable amorphous films that could be poled efficiently. The poling efficiency (r_{33}/E_p) of neat YLD-124 ($1.4 \pm 0.1\ nm^2/V^2$) is about 40% higher than YLD-124 dispersed at 25 wt% in host polymer poly(methyl methacrylate) (PMMA) ($\sim 1\ nm^2/V^2$). We initially found it surprising that YLD-124 was a good film-forming material as a neat chromophore because it readily forms crystals when purified, as evidenced by DSC analysis

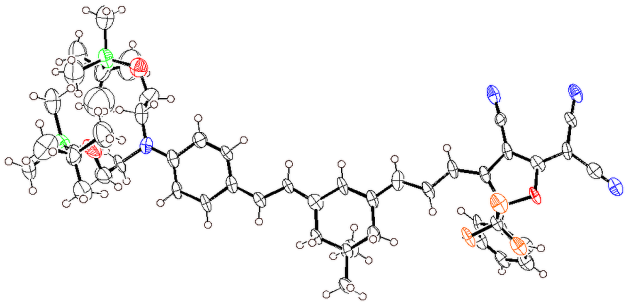

Figure 2.2: Individual molecule from YLD-124 crystal structure. All double bonds along the bridge are transoid (Figure 2.36 shows two molecules in the unit cell which are antiparallel and are enantiomers). Grey=carbon, brown=hydrogen, orange=fluorine, blue=nitrogen, red=oxygen, green=silicon.

Table 2.1: Dipole moment (μ_z) and hyperpolarizability (β) calculated using LC-BLYP/6-31+G* in vacuo; given according to the perturbation convention. Frequency-dependent β is computed at 1310 nm.

Structure	μ_z	$\beta_{zzz}(0) \times 10^{-30} esu$	$\beta_{zzz}(-\omega;\omega,0) \times 10^{-30} esu$
YLD124	22.0	460	641
JRD1	21.4	483	680
JRD5	20.3	476	664
JRD2	17.6	87.9	108
KRD2	20.0	341	463

(Figure 2.25) and the recently obtained x-ray-quality crystals (x-ray crystal structure shown in Figure 2.2 and more information in Figure 2.36 and Tables 2.1).

In spite of YLD-124's tendency to crystallize-also measured by DSC (melting point = 176.4 °C)-spin casting YLD-124 from the solvent 1,1,2-trichloroethane results in an optically clear and shiny film that poles efficiently. Both poled and unpoled films have remained glassy with no visible signs of crystallization or phase separation for over a year.

In spite of the success with neat films of YLD-124, we sought a way to ensure that the EO material would not crystallize during long-term use. The molecule was modified to prevent close packing: four methyl groups on the donor were replaced with four phenyl groups,

forming the TBDPS groups of molecule JRD1. The volume of a molecule of JRD1 (834.588 cm^3/mol) calculated by density functional theory was 28% larger than that of YLD-124 (653.946 cm^3/mol). JRD1 was indeed amorphous and showed a significant increase in poling efficiency, attaining an efficiency of 3.1 ± 0.1 $(nm/V)^2$ as a neat chromophore. YLD-124 should have a higher efficiency based on its higher number density if order is about the same, given that β and dipole moment are nearly equivalent for YLD-124 and JRD1 according to theoretical calculations (Table 2.1). But the poling efficiency of YLD-124 is lower, which suggests that the bulky substituents on the donor of JRD1 enables better mobility and can effectively reduce electrostatic interactions between chromophores, and provide needed space for the reorientation of the dipole vector during poling, and boost acentric order as a result.

Previously, functionalization of the bridge of NLO chromophores with bulky substituents has been shown to diminish unwanted intermolecular electrostatic interactions and increase the degree of poling of higher density chromophores. [52, 53] Therefore, we decided to add another site isolation group to the bridge area of the JRD1 molecule. According to current paradigms, [54] additional chromophore substituents with high flexibility and many degrees of rotational freedom, such as alkyl chains, could lower the T_g below a desirable temperature (i.e. lower the stability temperature of the poled chromophore film). [48] Therefore, we decided to introduce a large, rigid, fused ring moiety, that of a carbazole, a commonly-used functional group in high T_g organic polymers, for its ease of synthesis and likelihood to have little electronic influence on the chromophore's π-bridge system. Density functional theory calculations of the carbazole-containing chromophore JRD5 predicted that the carbazole substituent decreased the chromophore's hyperpolarizability by only 2% (Table 2.1). [54,55] Furthermore, calculated HOMO and LUMO orbital images are very similar for JRD1 and JRD5 with only a very small extension onto the carbazole framework, HOMO LUMO energy levels for the two are less than 0.08 eV apart, and the calculated HOMO-LUMO gap difference is less than 0.04 eV (Figure 2.40). A carbazole substituted bridge unit **1** was synthesized through successful SN2' nucleophilic attack of carbazole anion on 4-bromoisophorone (Figure 2.3). ^{13}C NMR spectroscopy showed that the C-3 chemical shift, which is very sensitive to the electron-donating or withdrawing effect of the substituent at the C-2 position, [55] was 159.50 ppm for **1**, which is very similar to that of the unsubstituted isophorone, 160.4 ppm,

Table 2.2: Summary of the physical, spectroscopic, and nonlinear optical properties of 5 EO chromophores.

EO Material	ρ_N [a] $/molx \times 10^{20} cm^{-3}$	T_g- T_d [b] /°C	$\lambda_{max}^{CHCl_3}$ nm	$\overline{r_{33}/E_p}$ $/(nm/V)^2$	Best r_{33}/pm/V[d] no barrier, BCB[c]
YLD124[b]	6.83	81-208	786	1.4±0.1	118±29, 242±37
JRD1[b]	5.33	82-226	784	3.1±0.1	314±55, 556±90
JRD5	4.65	101-233	778	2.9±0.1	188±32, 214±46
JRD2	6.12	60-272	630	0.3±0.1	22±5, NA
KRD2	5.52	75-240	762	1.4±0.1	150±20, NA

a) Number density calculations assume a material density of 1 $g\ cm^{-3}$. b) T_d: the decomposition temperature. c) See ref [2]. d) The errors are standard errors for the entire data sets. Additional information for the poling results are shown in Table 2.9 and Figure 2.45.

indicating that the carbazole is less electron donating than an alkoxy or alkyl substituent. The carbazole is rotated by 70° according to the crystal structure of **1**, and 89° according to the calculated structure of JRD5, and therefore does not interfere with the extended π character of the bridge. The rest of the chromophore synthesis followed the same procedure as for JRD1, creating JRD5. Two other chromophores with different bridge types were also developed as controls: one is called JRD2, having the same acceptor and donor as JRD1, but lacking an extensive conjugated π bridge. Another, KRD1, shares the same acceptor and donor as JRD1, but with a thiophene bridge, referred to as "FTC-type". Chromophore syntheses and characterization are detailed in section 2.5. This study provides a broad understanding of the impacts on material properties caused by different bridge sizes, types, and functionalization and donor steric bulk for monolithic EO materials.

Layered, parallel plate devices for electric field poling and r_{33} measurement were fabricated with the following device architecture: indium tin oxide (ITO)/EO material/gold. ITO (45 nm thick, resistivity $\geq$ 100 ohms/sq.) was purchased coated on glass from Thin Film Devices. Solutions of monolithic chromophores in 1,1,2-trichloroethane solvent were filtered through a 0.2 μm PTFE filter and spun cast on ITO/Glass substrates. The films

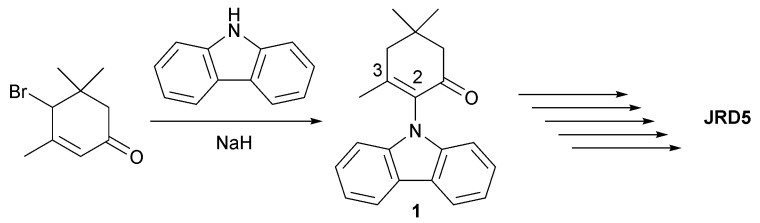

Figure 2.3: Synthesis of carbazole substituted bridge for JRD5.

were then dried on a hot plate at 65 °C for half an hour, and then further cured in a vacuum oven at 65 °C overnight, resulting in 1-1.7 μm thick films. A 60 nm thick gold layer was sputter coated as the top electrode to complete the poling structure.

An in-situ electric field poling configuration incorporated with a Teng-Man ellipsometry apparatus was employed for monitoring the real-time parameters (e.g. current, voltage, temperature) during chromophore alignment and measurement of r_{33} at 1310 nm. [13, 56] The samples were poled under DC electric fields ranging from 40-105 $V\mu m^{-1}$while heating from room temperature to the poling temperature (T_p, closely related to T_g) at a rate of 10 °C min^{-1}. The temperature was held at T_p where poling occurred for about 5 min and then cooled well below T_p before the poling field was removed.

Important parameters for comparison between JRD1 and JRD5 are listed in Table 2.2. Poling efficiency is regarded as the standard to appraise the EO performance of different chromophores, since r_{33} scales linearly with the applied poling field. Of note is that, unlike polymer guest-host systems, the conductance of devices fabricated from monolithic materials during poling is significant, causing a notable drop in voltage across the EO layer. So, the average electric field during poling was used in the calculation for a more accurate estimation of intrinsic poling efficiency. [2] JRD5 has a poling efficiency of 2.9 ± 0.2 $(nm/V)^2$, which is nearly identical with the result of JRD1 3.1 ± 0.1 $(nm/V)^2$, within the experimental error, and twice as large as the poling efficiency of YLD-124 as a neat film. Because these three molecules have similar β values inferred from the shared CLD-type molecular motifs [57] and β_{zzz} calculations (Table 2.1), the increases for JRD1 and JRD5 can be attributed to the improvement in $\langle \cos^3 \theta \rangle$. YLD-124 is seemingly not able to obtain a thermodynamic

equilibrium value during poling and is kinetically trapped, while the TBDPS groups of JRD1 and JRD5 facilitate greater molecular mobility. [58] $\rho_N\langle\cos^3\theta\rangle$ for JRD1 and JRD5 is remarkably about twice that of YLD-124. It is also worth noting that DLD136, a CLD-type chromophore with bis(TBDPS) groups attached on the bridge has a poling efficiency (1.7 $(nm/V)^2$) far less than JRD1 despite having a similar ρ_N (4.95×10^{20} $molecules/cm^3$) and β. [48] This underscores the importance of proper placement of the TBDPS group.

With the additional carbazole modification of the bridge, the T_g of JRD5 increases to 101 °C. This result is comparable to guest/host systems of YLD124 and PMMA at around 25% loading. JRD5 is thus expected to have equivalent thermal stability to previously studied guest/PMMA materials because the relaxation of poled order is closely related to T_g. [59] This is an important advance considering the low-T_g barrier of high performance monolithic chromophores reported so far. In addition, thin films derived from JRD1 and JRD5 showed excellent film quality and could be kept at ambient temperature for a long term without any observable phase separation or cracking. JRD5 films, especially, had better film quality with less dispersion and fewer surface irregularities (i.e., pinholes) than JRD1 during fabrication. In contrast, an alternative CLD-type chromophore HD-BB-MOM (Figure 2.4) was designed with rigid site isolation groups similar to JRD5, but instead of TBDPS groups, a benzyl ether-containing unit was used. Because of the high flexibility of the benzyl ether groups, [60] HD-BB-MOM had good solubility and was amorphous as a neat material, and the rigid fluorene and naphthalene units increased the T_g to 101 °C, the same as JRD5. However, the film formation of HD-BB-MOM was not very good; tiny pinholes resulted in over half of the devices having electrical shorts, and for the devices that were successful, the poling efficiency, 1.1 ± 0.2 $(nm/V)^2$, was far below JRD1 and JRD5 in spite of a similar ρ_N (4.83×10^{20} $molecules/cm^3$) and comparable β. We conclude that the two bulky TBDPS groups of JRD1 and JRD5 properly placed at the donor end promote smooth film formation, amorphous character, efficient poling, and are an important design element in monolithic, high number density chromophores.

Bridge size and type influenced the optical properties (e.g. wavelength of maximum absorption, λ_{max}). Because β generally increases as λ_{max} increases [61,62] the bridge type also had a strong impact on EO performance. YLD-124, JRD1, and JRD5 have similar λ_{max}

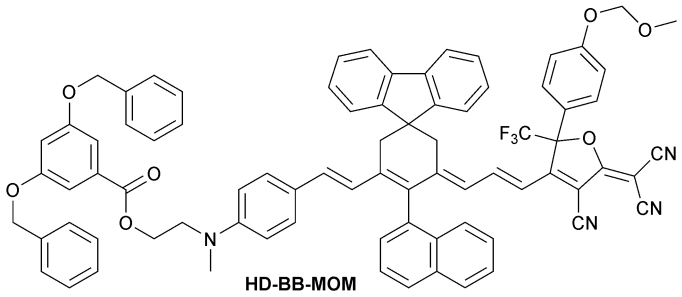

Figure 2.4: Molecular structure of the comparative chromophore HD-BB-MOM.

values within 10 nm of one another in chloroform solution. JRD2 exhibited a significantly blue-shifted absorption due to the presence of a much shorter diene bridge compared to the tetraene bridge of the CLD-type chromophores. Accordingly, the poling efficiency of JRD2 was only one tenth of the result of JRD1. From another aspect, it is interesting that a molecule as small as JRD2 formed films of reasonable quality and was successfully poled as a monolithic system. This confirms the effect of TBDPS groups on the physical properties of monolithic chromophores in this series. The same theory also applies to KRD1, a chromophore with thiophene replacing some of the bridge architecture of JRD1. While KRD1 is amorphous by DSC, the TBDMS analog is not (melting point = 180 °C). [63] The poling efficiency of KRD1 was 1.4 ± 0.1 $(nm/V)^2$, half of that of JRD1, consistent with the ratio of β measurements for CLD and FTC based chromophores, and in r_{33} measurements of CLD and FTC based chromophores in host-guest systems. [51, 63, 64] However, the differences in β were not reflected in poling efficiency comparison between KRD1 and YLD-124, which once again proves the efficacy of the bulky TBDPS groups in maximizing $\rho_N \langle \cos^3 \theta \rangle$. Collectively, this group of five chromophores shows that the β value, as a function of bridge size and type, together with acentric order enhanced by donor steric size ultimately determined the EO performance of a chromophore.

2.3 Conclusions

In conclusion, a new generation of monolithic organic EO chromophores based on the introduction of bis(TBDPS) units is reported for the study of structure-function relationships.

The EO performance and the auxiliary properties (e.g. viscoelastic properties, film quality) of the monolithic materials could be improved through site isolation by the modification of substituents. JRD5 has a poling efficiency approximately equal to that of JRD1 (∼3 $(nm/V)^2$) while having a higher glass transition temperature, comparable to that of the popular NLO guest/PMMA polymer system. JRD5 is a rare example of a single-component chromophore to have a poling efficiency of ∼3 $(nm/V)^2$ and a $T_g > 100$ °C, which is astonishing; others meeting these criteria have been binary chromophore mixtures. [52] This is a significant achievement not only because the poling efficiency is among the highest ones reported so far, but also the significant improvement in the aspect of thermal stability for high number-density chromophores. This improvement (demonstrated in this work) bodes well for future discoveries that will raise the T_g even further. This can be accomplished through implementation of Diels-Alder cross linking, for example, and the ability to tune and control the T_g, which we have shown here, will be important for coordinating the poling and crosslinking temperatures. [65–67] This work demonstrates the importance, subtlety, and feasibility of proper molecular design to improve EO material properties.

2.4 Experimental

General information: Chemicals used were purchased from Sigma Aldrich, Acros, Alfa Aesar, or TCI and used without further purification unless otherwise noted. 1,1,2 trichloroethane (TCE) was purified via vacuum distillation prior to use. ITO/glass slides were purchased from Thin Film Devices, Inc. Optical profilometry measurements were carried out on an NT-2000 model profilometer, provided by WYKO Corporation. In situ Teng-Man ellipsometry was carried out on a home built device. [21] UV-visible Absorption Spectroscopy was obtained on a Shimadzu 1601 or a Varian Cary 5000 spectrometer. Differential Scanning Calorimetry (DSC) data was acquired on a TA Instruments Q100 with heating and cooling under nitrogen at rates of 10 °C per min. Thermogravametric Analysis (TGA) data was acquired on a TA Instruments Q500 with heating under nitrogen at 20 °C per min. TGA and DSC analyses were carried out at the Advanced Materials Science and Engineering Center (AMSEC) at Western Washington University. High-Resolution Mass Spectrometry (HRMS) was performed using a Waters Micromass Quattro Premier XW instrument using

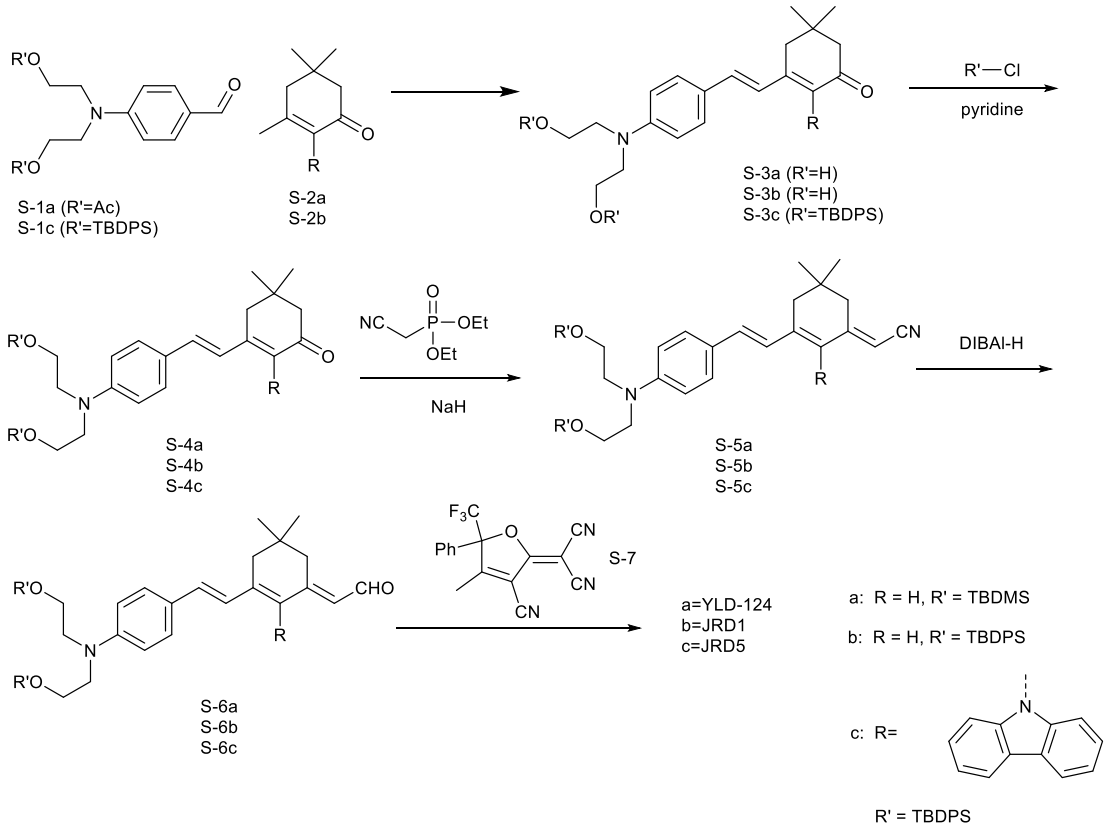

Figure 2.5: Synthetic route to CLD class chromophores

electrospray ionization to acquire a high resolution spectrum. ^{1}H NMR spectra were acquired using a Bruker AVance ugseries instrument running at 300 MHz or 500 MHz. All ^{1}3C NMR spectra were acquired on a Bruker AVance 500 MHz instrument.

2.5 Synthetic Details

The synthesis of organic ring-locked tetraene donor-π-acceptor molecules was accomplished via the trinary convergent synthesis of the donor, the bridge, and the acceptor. Once these three components are synthesized, they can be assembled in any order. [68] Several authors have previously published syntheses outlining various substitutions and methods to synthesize various analogues of this class of molecules. [51, 69–72] Here we present a detailed method for the synthesis of YLD-124 with recent modifications and additional details for

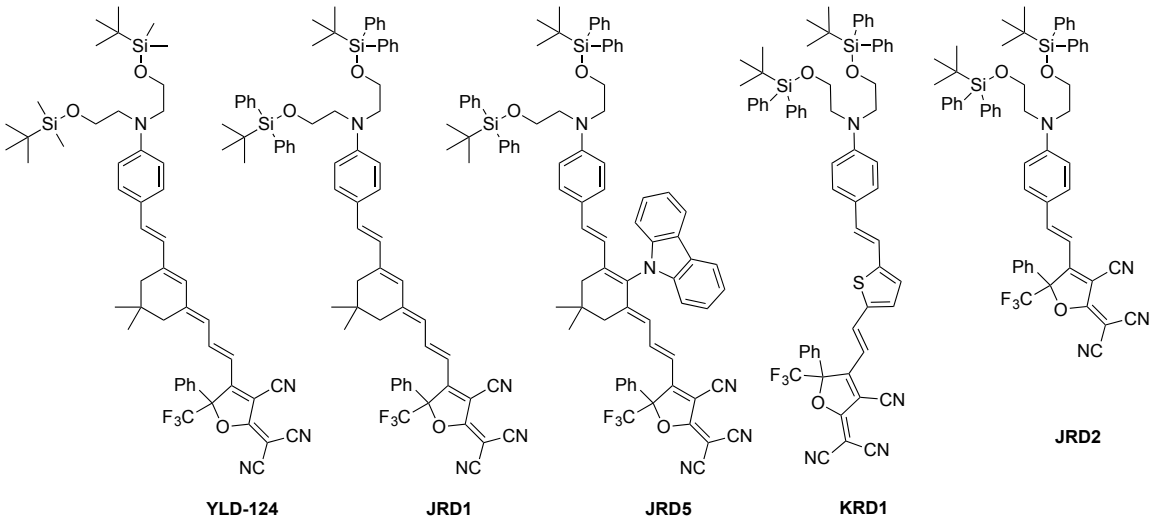

Figure 2.6: Structures of five molecules examined in this study.

the synthesis of analogues. In some cases, where the molecules were not new or reaction methods were the same, characterization of intermediates was limited to TLC.

2.5.1 YLD-124

3-[2-[4-[bis(2-hydroxyethyl)amino]phenyl]ethenyl]-5,5-dimethyl-2-cyclohex-en-1-one (S-3a): This two step reaction first couples the α, β unsaturated ring-locked bridge unit to the aldehyde donor resulting in extended conjugation and then removes the remaining acetate protecting groups. Two routes are employed. In the case of YLD-124 and JRD1, isophorone is the bridge unit being coupled to S-1a (prepared according to literature methods). [73] The methoxide route outlined below or some variation of the Claisen-Schmidt condensation is sufficent; [30,51,74] however, an alternative route was employed for JRD5 as outlined below. [75] The condensation reaction can be accomplished quite effectively (conversion up to 90% were observed by ^{1}H-NMR) using sodium metal and methanol. The introduction of sodium metal drives the reaction by eliminating residual water while generating dry methoxide *in-situ*. The reaction is carried out in a dual-neck round bottom flask fitted with a reflux condensor at constant atmospheric pressure under the protection of inert gas with an exterior ice bath. Clean sodium (20 g, 833 mmol) reacts with dry methanol

(250-300 mL) to produce sodium methoxide, hydrogen gas, and heat. The resulting mixture is cloudy and white in color. Isophorone is then added (9.5 mL, 63 mmol) and the solution is heated to reflux under protection of nitrogen. The solution is a dark red color. Dry S-1a is then added (17 g, 58 mmol) and the reaction is refluxed overnight. The resulting mixture must then undergo hydrolysis to completely remove the acetate protecting groups. Residual methanol is removed by rotary evaporation to prepare for simultaneous hydrolysis and liquid-liquid extraction. After rotary evaporation, the dark-red, crude reaction mixture from the previous step is diluted with a large excess of 0.1 N HCl, followed by titration with 1.0 M acetic acid until a sharp color change is observed. The color change presumably marked the point at which the acetate protecting groups were fully removed, a mixture of protected, half protected, and de-protected products was produced when the hydrolysis step was not undertaken (as observed by TLC and NMR). The resulting organic material is extracted from the biphasic mixture in a separatory funnel by minimal aliquots of dichloromethane (DCM) or chloroform, which is then removed under reduced pressure. Further purification can be accomplished by diluting the resulting solids with diethyl ether spiked with 2% to 5% ethyl acetate (EtOAc). The dilution with ether/EtOAc is accompanied by the precipitation of salts (presumably sodium acetate or other sodium based salts) that are conveniently separated using a fritted funnel. Residual salts remaining in the organic layer are then washed away using small aliquots of water or brine. The ether/EtOAc and product mixture is then dried of residual water using magnesium sulfate, and the solvent is removed by rotary evaporation followed by 12 hours in a vacuum oven at 60 °C. The resulting crude organic material can either be further purified by flash column chromatography, [76] precipitation, or crystallization from either EtOAc or acetone. 40% yield. MS (ESI) (M+H, $C_{20}H_{27}NO_3$): calcd, 330.20 $[M+H]^+$; found, 330.4 $[M+H]^+$.

3-[2-[4-[bis[2-[[(1,1-dimethylethyl)dimethylsilyl]oxy]ethyl]amino]phenyl]-ethenyl]-5,5-dimethyl-2-cyclohexen-1-one (S-4a): Silyl protection is carried out in flame dried glassware by adding tert-but[1]Himethylsilyl chloride (4.0 g, 27 mmol) to mixture of imidazole (2.4 g, 35 mmol) and dry dimethyl formamide (DMF, 9 mL). [29,77] S-3a (2.0 g, 6 mmol) is then added. The reaction is stirred overnight with gentle heating. The reaction is quenched with water, diluted with a mixture of hexanes and EtOAc, and then washed with brine to

remove residual DMF and imidazole. Flash chromatography is used to complete the purification and residual solvents are removed by rotary evaporation followed by 12 hours in a vacuum oven at 60 °C. [29, 76, 78] 99% conversion by TLC, overall yield: 90%.

2-[3-[(1E)-2-[4-[bis[2-[[(1,1-dimethylethyl)dimethylsilyl]oxy]ethyl]amino]phenyl]-ethenyl]-5',5'-dimethycyclohex-2-en-1-ylidene]-acetonitrile (S-5a): All glassware is flame dried prior to assembly. A multi-neck round-bottom flask is fitted with a reflux condenser and a stir rod. The flask is charged with 60% sodium hydride suspension (0.2 g, 6 mmol) and placed under the protection of inert gas at a constant one atmosphere of pressure and lowered into an ice bath. Dry, degassed THF is added via syringe (20 mL). Diethyl cyanomethylphosphonate (1.0 mL, 6 mmol) is added drop-wise via syringe producing bubbles of hydrogen gas. The solution is cloudy white. Once the diethyl cyanomethylphosphonate is completely added, the ice bath is removed and the reaction is brought to room temperature. The solution is then clear. Dry S-4a (1.2 g, 2 mmol) is dissolved in dry degassed tetrahydrofuran (THF), then added to the mixture via cannula transfer and the reaction is refluxed overnight. [48, 79, 80] The reaction is then cooled, quenched with water, and residual THF is removed by rotary evaporation. The resulting mixture is diluted with a mixture of hexanes and EtOAc. Residual salts are removed via liquid/liquid extraction. The resulting organic layer is dried using magnesium sulfate and flash chromatography is performed. Residual solvent is then removed via rotary evaporation and the product is placed in a vacuum oven at 60 °C overnight to dry. 99% conversion by TLC, 80% yield overall. MS (ESI) (M+H, $C_{34}H_{56}N_2O_2Si_2$): calcd, 581.39 $[M+H]^+$; found, 581.6 $[M+H]^+$.

2-[3-[2-[4-[bis[2-[[(1,1-dimethylethyl)dimethylsilyl]oxy]ethyl]amino]phenyl]ethenyl]-5,5-dimethyl-2-cyclohexen-1-ylidene]-acetaldehyde (S-6a): A single neck round bottom flask is flame dried and placed under the protection of an inert gas. The flask is charged with pure, dry S-5a (2.3 g, 4 mmol). Dry and degassed toluene is added (100 mL). The reaction vessel is lowered into a bath of dry ice and acetone and allowed to chill. Diisobutylaluminum hydride (DiBAl-H) is added to the mixture drop-wise (6.9 mL, 1 M) and the solution turns a dark red color. The reaction is allowed to react for two hours or monitored by thin layer chromatography (TLC). Hydrolysis is then accomplished by the addition of damp silica (10 g, about 10% water by mass), which is added to the reaction mixture and

the reaction is allowed to return to room temperature while being stirred overnight. The resulting mixture is then diluted with hexane/EtOAc, dried with magnesium sulfate, filtered through a coarse grain filter paper, and placed onto a large flash chromatography column. Residual solvent is removed via rotary evaporation and the product is dried in a vacuum oven at 60 °C overnight. [30,81] 58% yield. MS (ESI) (M+H, $C_{34}H_{57}NO_3Si_2$): calcd, 584.39 $[M+H]^+$; found, 584.7 $[M+H]^+$.

2-[4-(3-[3-[2-(4-[Bis-[2-(tert-butyl-dimethyl-silanyloxy)-ethyl]-amino]-phenyl)-vinyl]-5,5-dimethyl-cyclohex-2-enylidene]-propenyl)-3-cyano-5-phenyl-5-trifluoromethyl-5H-furan-2-ylidene]-malononitrile (YLD124): A round bottom flask is flame dried, fitted with a reflux condenser, placed under the protection of nitrogen, and charged with dry CF3-Ph-TCF acceptor (0.4 g, 1 mmol) and aldehyde (0.7 g, 1 mmol). Ethanol is dried with magnesium sulfate and added to the reaction vessel via a filtered syringe. The reaction vessel is lowered into an oil bath and refluxed for 20 minutes. The vessel is then cooled in an ice bath and residual ethanol is removed via rotary evaporation. The resulting mixture is purified using flash column chromatography and precipitation from a concentrated DCM solution in excess cold methanol. [30, 81] 20% yield. Desired product was confirmed by TLC, UV-Vis, ESI-MS and ^{1}H NMR and X-ray crystallography. [74]

2.5.2 CF3-Ph-TCF Acceptor

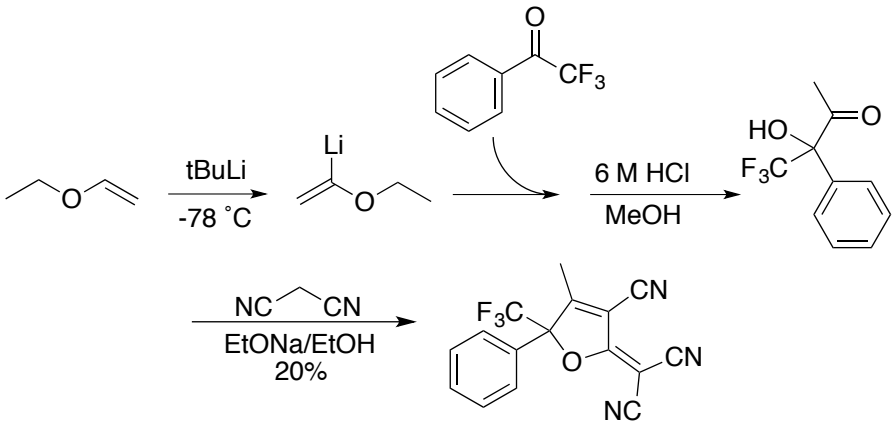

Figure 2.7: Synthesis of CF3-Ph-TCF Acceptor (S-7).

[3-cyano-4-methyl-5-phenyl-5-(trifluoromethyl)-2(5H)-furanylidene]-propanedinitrile (CF3-Ph-TCF Acceptor S-7): CF3-Ph-TCF acceptor was prepared by the application of tert-butyl lithium (200 mL 1.7 M (340 mmol) in THF) to ethyl vinyl ether (27.2 mL, 284 mmol) at -78 °C, followed by addition of 2,2,2-trifluoroacetophenone (26.6 mL, 188 mmol) to form the desired ketol, which is then purified by vacuum distillation. [82] 84% yield, GCMS (M^+, $C_{10}H_9F_3O_2$): calcd, 218.06; found, 218. The recovered ketol (25 g ketol, 115 mmol) was then condensed with malononitrile (14.9 g, 240 mmol) in a solution of sodium ethoxide in dry ethanol. [83] The resulting solution was condensed via rotary evaporation to remove most of the ethanol, followed by flash chromatography using DCM as the principle solvent. Two distinct fractions were observed, one pale green and one light brown. Both were positive for the desired product by GCMS (M^+, $C_{16}H_8F_3N_3O$): calcd, 315.06; found, 315. Further purification was carried out by precipitation of a white powder in cold hexanes. 24% yield.

2.5.3 JRD1

3-[2-[4-[bis(2-hydroxyethyl)amino]phenyl]ethenyl]-5,5-dimethyl-2-cyclohex-en-1-one (S-3b): Prepared from the synthesis of YLD-124 outlined above.

3-[2-[4-[bis[2-[[(1,1-dimethylethyl)diphenylsilyl]oxy]ethyl]amino]phenyl]-ethenyl]-5,5-dimethyl-2-cyclohexen-1-one (S-4b): tert-Butyl(chloro)diphenylsilane (42.5 mL, 163 mmol) was added dropwise to a solution of imidazole (23 g, 337 mmol) and dry DMF (235 mL). S-3b (22.5 g 68.1 mmol) was then added and the reaction was stirred overnight. The resulting mixture was diluted with EtOAc and ether, washed with cold water, dried with sulfates of magnesium and sodium, then purified via flash chromatography and used in the next reaction without further characterization. 90% yield.

2-[3-[(1E)-2-[4-[bis[2-[[(1,1-dimethylethyl)diphenylsilyl]oxy]ethyl]amino]phenyl]-ethenyl]-5',5'-dimethycyclohex-2-en-1-ylidene]-acetonitrile (S-5b): Diethyl cyanomethylphosphonate (23.6 mL, 146 mmol) was added dropwise to a solution of sodium hydride suspension (4.9 g, 60% m/m, 123 mmol) in THF. Ice was used to cool the reaction during the addition and then warmed to room temperature and re-submerged into an ice bath for the addition of S-4b. A concentrated solution of S-4b was added via cannula transfer (13.1 g, 16 mmol). The product was identified by TLC and moved to the next reaction without further purification. 90% yield.

2-[3-[2-[4-[bis[2-[[(1,1-dimethylethyl)dimethylsilyl]oxy]ethyl]amino]phenyl]ethenyl]-5,5-dimethyl-2-cyclohexen-1-ylidene]-acetaldehyde (S-6b): A single neck round bottom flask is flame dried and placed under the protection of nitrogen. The flask is charged with S-5b (10 g, 12.1 mmol) and toluene is added. The reaction is chilled with dry ice and acetone. DiBAl-H is added drop-wise. The reaction is allowed to react for two hours. Hydrolysis is then accomplished by addition of damp silica (14.0 g, about 10% water by mass) followed by stirring overnight. Product was identified via TLC (∼50% yield), purified via flash chromatography and moved to the final reaction without further characterization. 40% yield overall.

2-[4-(3-[3-[2-(4-[Bis-[2-(tert-butyl-diphenyl-silanyloxy)-ethyl]-amino]-phenyl)-vinyl]-5,5-dimethyl-cyclohex-2-enylidene]-propenyl)-3-cyano-5-phenyl-5-trifluoromethyl-5H-furan-2-ylidene]-malononitrile (JRD1): The synthesis of JRD1 is essentially identical to that of YLD124. The change in silyl ether protecting group, i.e., the substitution of two methyl groups with two phenyl groups, instills a notable decrease in polarity compared to that of YLD124 which is especially apparent when selecting solvents for thin-layer and

flash chromatography. CF3-Ph-TCF acceptor (3.1 g, 9.8 mmol) and S-6a (6.8 g, 8.1 mmol) are refluxed in ethanol for 20 minutes followed by rotary evaporation and flash chromatography. 34% yield. The desired product is further purified by precipitation overnight from a concentrated solution of DCM into cold excess hexanes. MS (ESI) (M^+, $C_{70}H_{71}F_3N_4O_3Si_2$): calcd, 1128.5011; found, 1128.4998. ^{1}H NMR δH(500 MHz; $CDCl_3$; Me_4Si) 7.61 (8 H, d, J=7.7 Hz, Ar-H), 7.50 (5 H, m, Ar-H), 7.42 (4 H, t, J=7.5 Hz, Ar-H), 7.34 (8 H, t, J=7.4 Hz, Ar-H), 7.18 (2 H, d, J=8.7 Hz, Ar-H), 6.88 (1 H, d, J=15.9 Hz, C-H), 6.72 (1 H, d, J=15.5 Hz, C-H), 6.38 (1 H, s, C-H), 6.31-6.33 (4 H, m, C-H, Ar-H), 3.75 (4 H, t, J=6.1 Hz, C-H2), 3.50 (4 H, t, J=6.1 Hz, C-H2), 2.40 (2 H, s, C-H2), 2.31 (1 H, d, J=16.5 Hz, C-H), 2.22 (1 H, d, J=16.2 Hz, C-H), 1.04 (18 H, s, C-H3), 1.02 (3 H, s, C-H3), 0.96 (3 H, s, C-H3). ^{13}C NMR δC(125 MHz; $CDCl_3$; Me_4Si) 175.93, 161.90, 159.19, 152.54, 149.47, 146.60, 136.65, 135.61, 133.28, 131.22, 130.38, 129.94, 129.83, 129.59, 129.56, 128.66, 127.79, 126.76, 125.55, 124.13, 122.22 (Q, $^1J_{CF}$=285 Hz), 115.40, 112.03, 111.86, 111.69, 111.17, 95.67 (Q, $^2J_{CF}$=30.3 Hz), 93.78, 60.86, 56.68, 52.94, 39.89, 39.64, 31.65, 28.62, 28.14, 26.85, 19.11.

2.5.4 JRD5

4-[Bis-[2-(tert-butyl-diphenyl-silanyloxy)-ethyl]-amino]-benzaldehyde (S-1c): Deprotected benzaldehyde (S-1a) was recovered from the synthesis of YLD124 (6.42 g, 31 mmol) and added to a solution of tert-butyldimethylsilyl chloride (17.5 mL, 67 mmol) and excess pyridine, then stirred overnight. The reaction was diluted with a mixture of hexanes/ EtOAc and washed with copious amounts of brine, passed through a silica plug, and precipitated in cold methanol. Product was identified by TLC and moved to the next reaction without further purification. Overall yield 90%.

3-[2-(4-[Bis-[2-(tert-butyl-diphenyl-silanyloxy)-ethyl]-amino]-phenyl)-vinyl]-2-carbazol-9-yl-5,5-dimethyl-cyclohex-2-enone (S-3c): Trimethylsilyldiethylammonium route: An alternative route to condense the bridge unit of JRD5 with the donor was explored. [75] This was in part due to the unpredictability of the sodium methoxide route employed previ-

ously, and also to avoid working with sodium metal and harsh reaction conditions that may produce side reactions with the modified bridge. The reaction was carried out by mixing lithium perchlorate (0.72 g, 6 mmol) and N,N-diethyltrimethylsilylamine (1.9 mL, 10 mmol) and the desired aldehyde (4.9 g, 7 mmol) for ten minutes under nitrogen, followed by addition of the bridge unit. Minimal THF was used as a solvent. The reaction mixture was purified via flash column chromatography and the desired material was identified by TLC. 90% yield.

[3-[2-(4-[Bis-[2-(tert-butyl-diphenyl-silanyloxy)-ethyl]-amino]-phenyl)-vinyl]-2-carbazol-9-yl-5,5-dimethyl-cyclohex-2-enylidene]-acetonitrile (S-5c): This reaction was carried out in a manner identical to that pertaining to YLD124 and JRD1 described above. Diethyl cyanomethylphosphonate (6.24 ml, 39mmol) was added to a solution of THF and 60% NaH suspension (1.5 g, 38 mmol). A solution of S-3c (5.0 g, 5 mmol) in THF was then added via cannula transfer and the reaction was refluxed overnight. The reaction was quenched with water and residual THF was removed via rotary evaporation. The resulting mixture was diluted with ethylacetate/hexanes, and residual salts were extracted with cold water. The product was dried with magnesium sulfate and then purified by flash chromatography. Residual solvent was stripped via rotary evaporation followed by 24 hours under vacuum at 60 °C. 90% yield. MS (ESI) (M^+, $C_{66}H_{71}N_3O_2Si_2$): calcd, 1016.50 $[M+Na]^+$; found, 1016.9$[M+Na]^+$.

[3-[2-(4-[Bis-[2-(tert-butyl-diphenyl-silanyloxy)-ethyl]-amino]-phenyl)-vinyl]-2-carbazol-9-yl-5,5-dimethyl-cyclohex-2-enylidene]-acetaldehyde: (S-6c) A round bottom flask is charged with S-5c (4.9 g, 5 mmol) and fitted with a reflux condenser. Dry degassed toluene is added (100 mL) and the reaction is cooled to -78 °C. DiBAlH in toluene is then added (8.5 mL 1.0 M). The reaction is stirred for 2 hours and monitored by TLC. Damp silica is then added (7 g, 10% water) and the reaction is stirred and allowed to come to room temperature overnight. Product was identified by TLC. 57% yield.

2-[4-(3-[3-[2-(4-[Bis-[2-(tert-butyl-diphenyl-silanyloxy)-ethyl]-amino]-phenyl)-vinyl]-2-carbazol-9-yl-5,5-dimethyl-cyclohex-2-enylidene]-propenyl)-3-cyano-5-phenyl-5-trifluoromethyl-5H-furan-2-ylidene]-malononitrile (JRD5): JRD5 was synthesized as outlined above for YLD124 and JRD1 with additional preparation of the bridge

unit and modification of the Claisen-Schmidt condensation step outlined above in the section labeled trimethylsilyldiethylammonium route. [75] CF3-Ph-TCF acceptor (1.1 g, 3.5 mmol) and S-6c (2.8 g, 2.8 mmol) are refluxed in ethanol for 20 minutes followed by rotary evaporation and column chromatography. 36% yield. MS (ESI) (M^+, $C_{82}H_{78}F_3N_5O_3Si_2$): calcd, 1293.5590; found, 1293.5604. ^{1}H NMR δH(500 MHz; $CDCl_3$; Me_4Si) 8.24 (2 H, dd, J=7.8 Hz, 3 Hz), 7.54 (8 H, dd, J=8.1 Hz, 1.4 Hz), 7.38-7.48 (7 H, m), 7.32-7.36 (5 H, m), 7.22-7.30 (10 H, m), 7.05 (2 H, dd, J=8.1 Hz, 4.7 Hz), 6.87 (1 H, d, J=15.9 Hz), 6.53 (2 H, d, J=9.1 Hz), 5.92 (1 H, d, J=14.9 Hz), 5.87 (1 H, d, J=15.9 Hz), 5.77 (2 H, d, J=9.1 Hz), 5.62 (1 H, d, J=12.2), 3.59 (4 H, t, J=6.7 Hz), 3.29 (4 H, t, J=6.6 Hz), 2.75 (2 H, s), 2.66 (1 H, d, J=15.9 Hz), 2.56 (1 H, d, J=15.9 Hz), 1.26 (3 H, s), 1.21 (3 H, s), 0.99 (18 H, s). 13C NMR δC(125 MHz; $CDCl_3$; Me_4Si) 175.55, 162.54, 153.50, 149.44, 148.92, 146.43, (141.18, 141.14), 138.69, 135.53, 133.13, 131.22, 129.79, 129.73, 129.59, 129.55, 127.72, 126.59, (126.42, 126.33), 124.27, 123.63, (122.95, 122.89), 121.90 (Q, $^1J_{CF}$=285 Hz), 120.52, (120.18, 120.10), 119.68, 116.87, 111.56, 111.32, 111.17, 110.66, 109.92, 95.83 (Q, $^2J_{CF}$=32.0 Hz), 95.58, 60.36, 57.95, 52.71, 40.38, 40.14, 31.02, 28.82, 28.29, 26.78, 19.01.

2.5.5 Carbazole-isophorone

2-(carbazol-9-yl)-3,5,5-trimethylcyclohex-2-en-1-one (S-2b): 4-bromoisophorone was prepared according to previously published methods. [30, 84, 85] SN2' nucleophilic substitution is then carried out to complete the carbazole substituted bridge unit. Carbazole was first purified via recrystallization in ethanol and dried under vacuum. A clean dry round bottom flask is charged with sodium hydride suspension (60%) (6.3 g / 0.26 mol) and THF under the protection of nitrogen at 1 atm constant pressure. The flask is lowered into an ice bath and a solution of slight excess carbazole (29.2 g / 0.17 mol) in THF is added dropwise. Bubbles of hydrogen gas were observed. 4-bromoisophorone (1.0 Meq) was then added and a distinct color change was observed. The reaction was allowed to stir at room temperature overnight. The reaction was quenched with water, diluted with EtOAc, washed with brine in a separatory funnel, dried with magnesium sulfate, and filtered through a fritted funnel. The residual solvent was then removed and via rotary evaporation and the remaining material

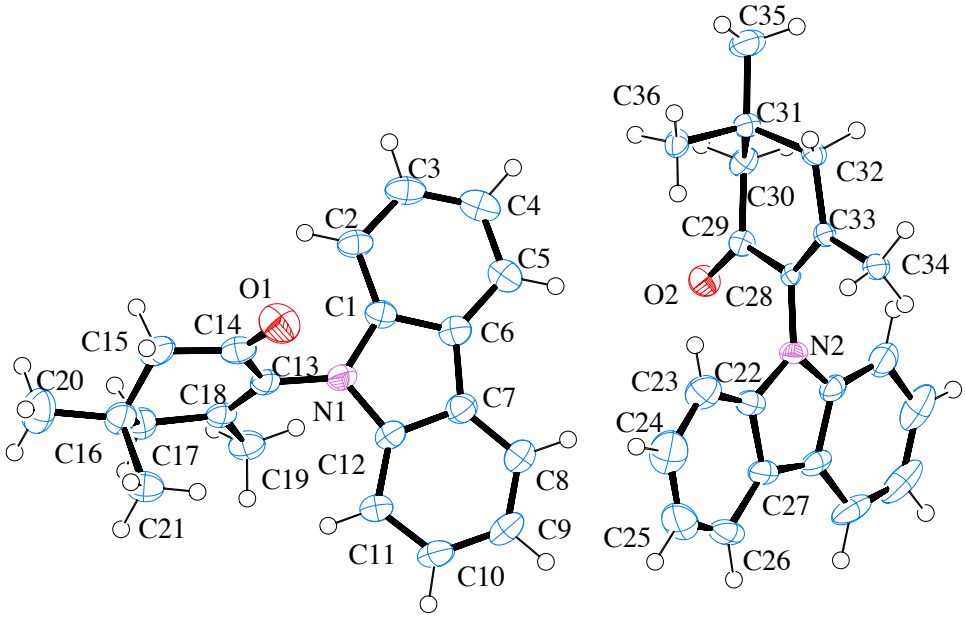

Figure 2.8: FCrystal Structure of JRD5 Bridge Unit.

was purified by flash chromatography and recrystallized in EtOAc. The major product of the reaction was that of isophorone with carbazole substituted at the 2 position, confirmed by x-ray crystallography (Figure 2.8). A minor product was also observed by GCMS (Figure 2.9). The minor product was confirmed to be that resulting from substitution at the 6 position. The minor product was also confirmed via X-ray crystallography, with ambiguous chirality. While the minor product was not reported in previous research, a similar minor peak of identical mass to the primary peak was observed in the gas chromatogram of bridge unit materials used for IKD-1-50. [24] ^{1}H-NMR (300 MHz, $CDCl_3$): δ 8.108 (d, J = 7.8, 2 H), 7.386 (t, J = 7.6, 2 H), 7.239 (t, J = 7.2, 2 H), 7.000 (d, J=8.0, 2H), 2.652 (s, 2 H), 2.591 (s, 2 H), 1.724 (s, 3 H), 1.291 (s, 6 H). ^{13}C-NMR (125 MHz, $CDCl_3$): δ 193.937, 159.503, 140.870, 130.454, 126.123, 126.055, 123.519, 120.779, 120.631, 119.975, 119.781, 109.769, 109.675, 51.845, 46.732, 33.360, 28.651, 20.893.

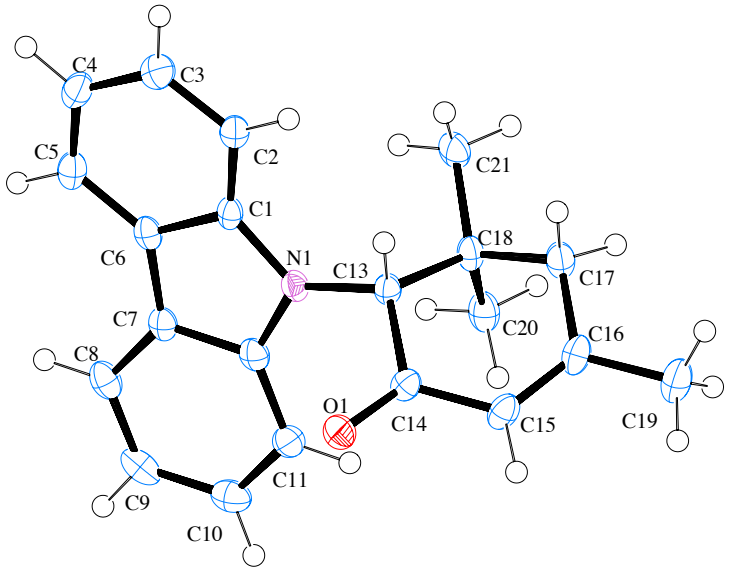

Figure 2.9: Crystal Structure of JRD5 Bridge Unit (Minor Product).

2.5.6 KRD1

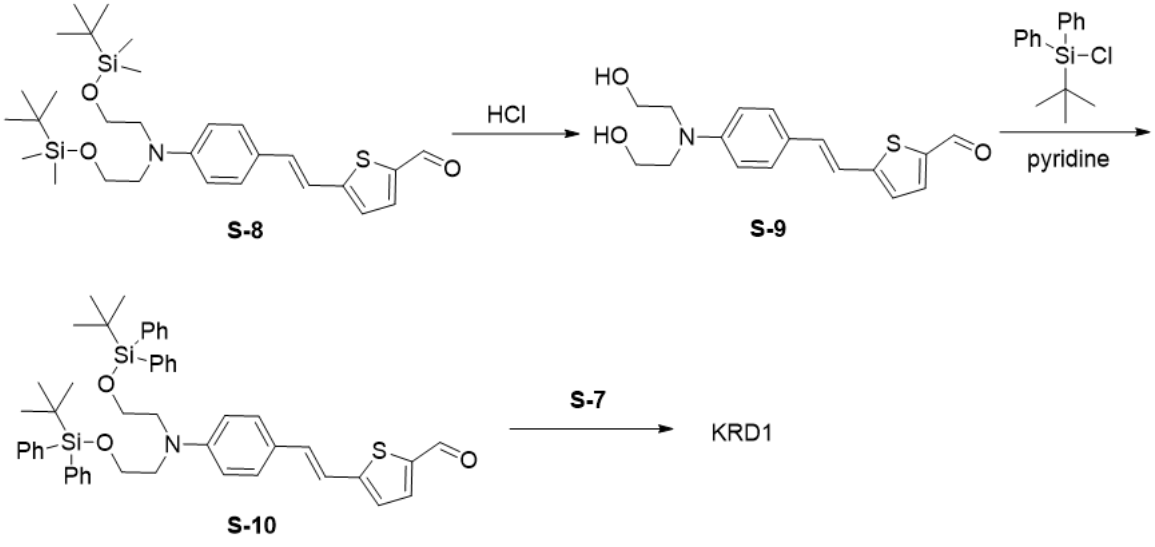

Figure 2.10: Synthesis of KRD1.

2-[4-(2-[5-[2-(4-[Bis-[2-(tert-butyl-diphenyl-silanyloxy)-ethyl]-amino]-phenyl)-vinyl]-thiophen-2-yl]-vinyl)-3-cyano-5-phenyl-5-trifluoromethyl-5H-furan-2-ylidene]-malononitrile: KRD1 was synthesized from precursor materials (aldehyde S-8) previously prepared for YLD156. [63] Hydrolysis of the tert-butyl dimethyl silyl protecting groups was followed by re-protection with that of diphenyl. Condensation of S10 (1.4 g, 1.7 mmol) with the CF3-Ph-TCF acceptor (0.6 g, 1.9 mmol) was then carried out by reflux in ethanol for 20 minutes. Desired product was purified by flash chromatography. Yield 38%. MS (ESI) (M^+, $C_{65}H_{61}F_3N_4O_3SSi_2$): calcd, 1090.3950; found, 1090.3934. ^{1}H NMR δH(300 MHz; $CDCl_3$; Me_4Si) 7.77 (1 H, d, J=15.1 Hz, C-H), 7.62 (8 H, d, J=6.5 Hz, Ar-H), 7.55-7.52 (5 H, m, Ar-H), 7.43 (4 H, t, J=7.3 Hz, Ar-H), 7.35 (8 H, t, J=6.9 Hz, Ar-H), 7.30 (1 H, d, J=4.2 Hz, C-H), 7.17 (2 H, d, J=8.9 Hz, Ar-H), 7.07 (1 H, d, J=15.7 Hz, C-H), 7.01 (1 H, d, J=4.1 Hz, C-H), 6.93 (1 H, d, J=15.7 Hz, C-H), 6.60 (1 H, d, J=15.3 Hz, C-H), 6.30 (2 H, d, J=8.9 Hz, Ar-H), 3.75 (4 H, t, J=5.9 Hz, C-H2), 3.50 (4 H, t, J=5.9 Hz, C-H2), 1.04 (18 H, s, C-H3). 13C NMR δC(125 MHz; $CDCl_3$; Me_4Si) 175.31, 162.05, 157.27, 149.40, 143.74 141.75, 137.98, 136.38, 135.57, 133.24, 131.57, 129.80, 129.61, 129.26, 127.75, 127.53, 126.83, 123.17, 115.5, 111.79, 111.67, 111.04, 110.61, 96.85, 96.70, 60.76, 58.34, 52.90, 26.81, 19.07 (CF_3 carbon too weak to observe).

2.5.7 JRD2

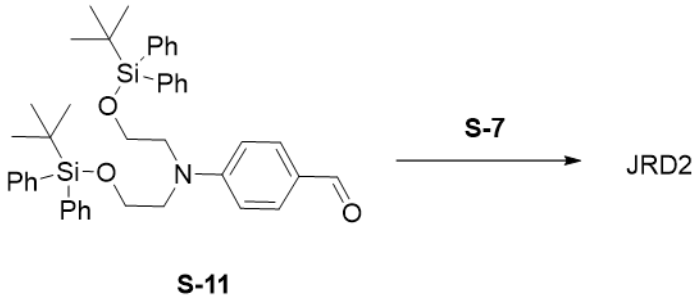

Figure 2.11: Synthesis of JRD2.

2-[4-[2-(4-[Bis-[2-(tert-butyl-diphenyl-silanyloxy)-ethyl]-amino]-phenyl)-vinyl]-3-cyano-5-phenyl-5-trifluoromethyl-5H-furan-2-ylidene]-malononitrile: JRD2 was re-

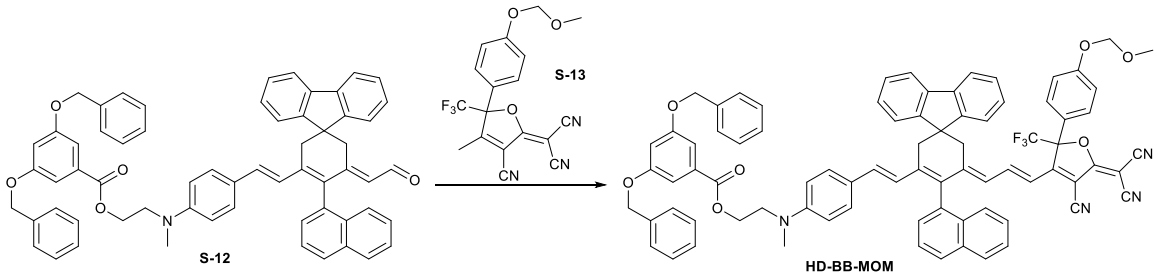

Figure 2.12: Synthesis of HD-BB-MOM.

covered as a byproduct of the synthesis of JRD1. Test reactions confirmed that the product could be synthesized through condensation of CF3-Ph-TCF acceptor and the corresponding donor. MS (ESI) (M^+, $C_{59}H_{57}F_3N_4O_3Si_2$): calcd, 983.3994 $[M+H]^+$; found, 983.3977 $[M+H]^+$. ^{1}H NMR δH(300 MHz; $CDCl_3$; Me_4Si) 7.69 (1 H, d, J=15.3 Hz, C-H), 7.52-7.58 (12 H, m, Ar-H), 7.38-7.43 (5 H, m, Ar-H), 7.30-7.34 (8 H, m, Ar-H), 7.21 (2 H, d, J=9.0 Hz, Ar-H), 6.69 (1 H, d, J=15.3 Hz, C-H), 6.39 (2 H, d, J=9.0 Hz, Ar-H), 3.77 (4 H, t, J=5.4 Hz, C-H2), 3.55 (4 H, t, J=5.7 Hz, C-H2), 1.02 (18 H, s, C-H3). 13C NMR δC(125 MHz; $CDCl_3$; Me_4Si) 175.99, 163.01, 153.65, 151.08, 135.49, 134.78, 132.84, 131.32, 130.14, 129.92, 129.61, 127.8, 127.68, 126.84, 122.55, 112.72, 111.5, 111.06, 108.71, 96.05 (Q, 2JCF=30.4 Hz), 94.13, 60.69, 56.71, 53.07, 26.77, 19.02, (CF_3 carbon too weak to observe).

2-([4-[(E)-2-[(5E)-5-[(2E)-3-[4-cyano-5-(dicyanomethylidene)-2-[4-(methoxymethoxy)phenyl]-2-(trifluoromethyl)-2,5-dihydrofuran-3-yl]prop-2-en-1-ylidene]-4-(naphthalen-1-yl)spiro[cyclohexane-1,9'-fluoren]-3-en-3-yl]ethenyl]phenyl](methyl)amino)ethyl 3,5-bis(benzyloxy)benzoate (HD-BB-MOM): Aldehyde S-12 (4.1 g, 4.6 mmol, orange solid) and acceptor S-13 (2.60 g, 6.93 mmol, light green powder) were charged to a flask, purged with nitrogen, and 12.0 mL ethanol was added. After heating to 70°C for 10 min, solubility was not very good, so 8 mL chloroform was added and heating under nitrogen was resumed for 2 hr resulting in a dark green solution. Solvent was stripped off by rotovap, and the product was purified by silica gel chromatography using gradient elution from 100% DCM to 15:1 DCM: EtOAc. Yield = 5.16 g (90%). HRMS (ESI) (M^+ $C_{80}H_{61}F_3N_4O_7$): calcd, 1246.4492; found, 1246.4463. δH(300 MHz; $CDCl_3$; Me_4Si) 8.03 (2

H, m), 7.86 (2 H, m), 7.43-7.72 (11 H, m), 7.28-7.39 (10 H, m), 7.16 (2 H, d, J=2.4 Hz), 7.12 (2 H, dd, J=8.8 Hz, J=2.4 Hz), 6.90 (1 H, d, J=9.0 Hz), 6.85 (2 H, d, J=8.8 Hz), 6.79 (1 H, d, J=9.2 H), 6.77 (1 H, t, J=2.4 Hz), 6.65 (1 H, br d, J=15.9 Hz), 6.52 (2 H, d, J=9.0 Hz), 6.37 (1 H, dd, J=15.5 Hz, J=3.5 Hz), 5.99 (1 H, dd, J=14.7 Hz, J=7.9 Hz), 5.92 (1 H, dd, J=12.3 Hz, J=5.9 Hz), 5.14 (1 H, s), 5.07 (1 H, s), 4.97 (4 H, s), 4.37 (2 H, t, J=5.7 Hz), 3.65 (2 H, t, J=5.5 Hz), (3.49, 3.48) (3 H, s), 3.35 (1 H, dd, J=18.0 Hz, J=5.3 Hz), 3.22 (1 H, dd, J=31.7 Hz, J=17.3 Hz), 2.99 (1 H, dd, J=18.2 Hz, J=9.0 Hz), 2.95 (3 H, s), 2.77 (1 H, dd, J=24.0 Hz, J=15.8 Hz).

2.6 NMR Spectra

2.6.1 JRD1

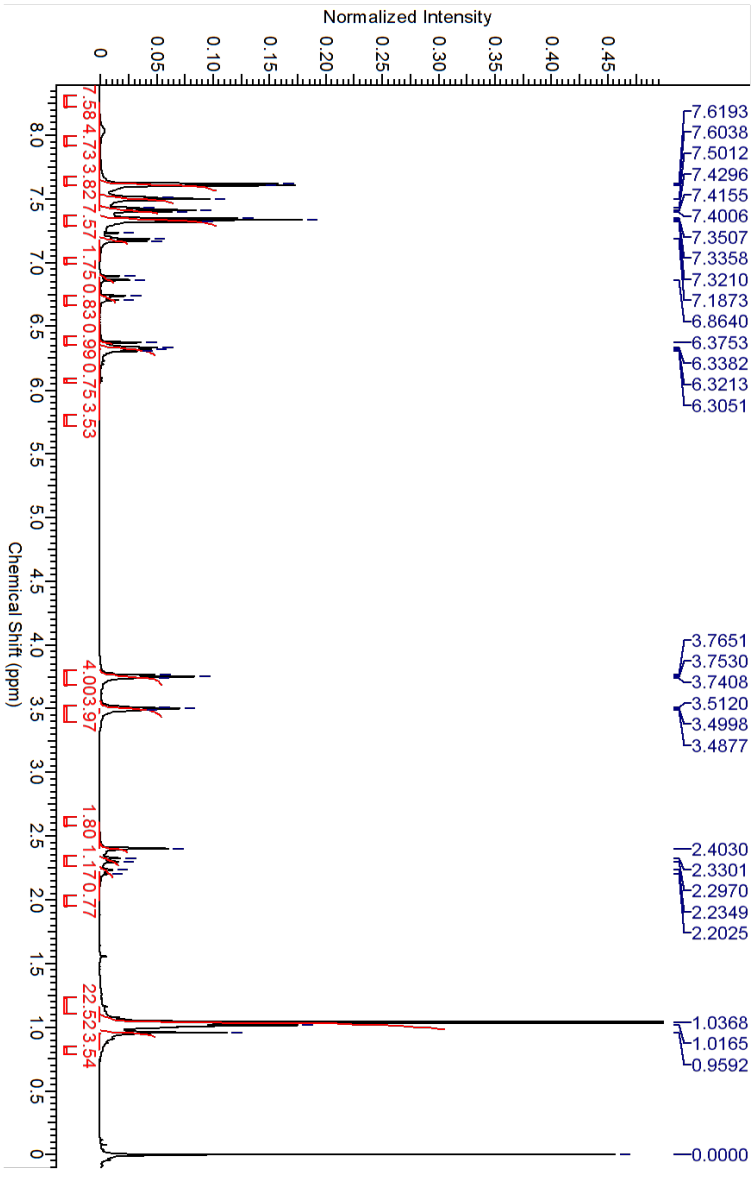

Figure 2.13: Proton NMR Spectra of JRD1.

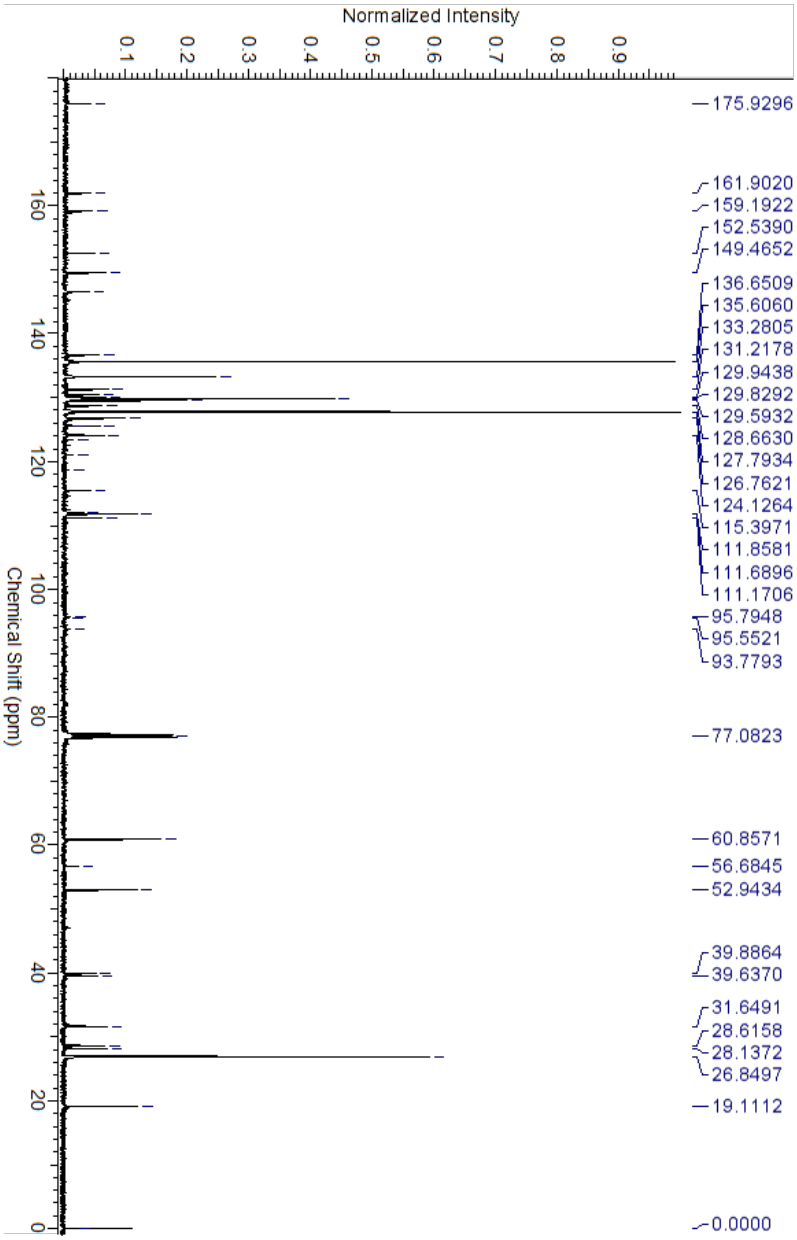

Figure 2.14: Carbon NMR Spectra of JRD1.

2.6.2 JRD5

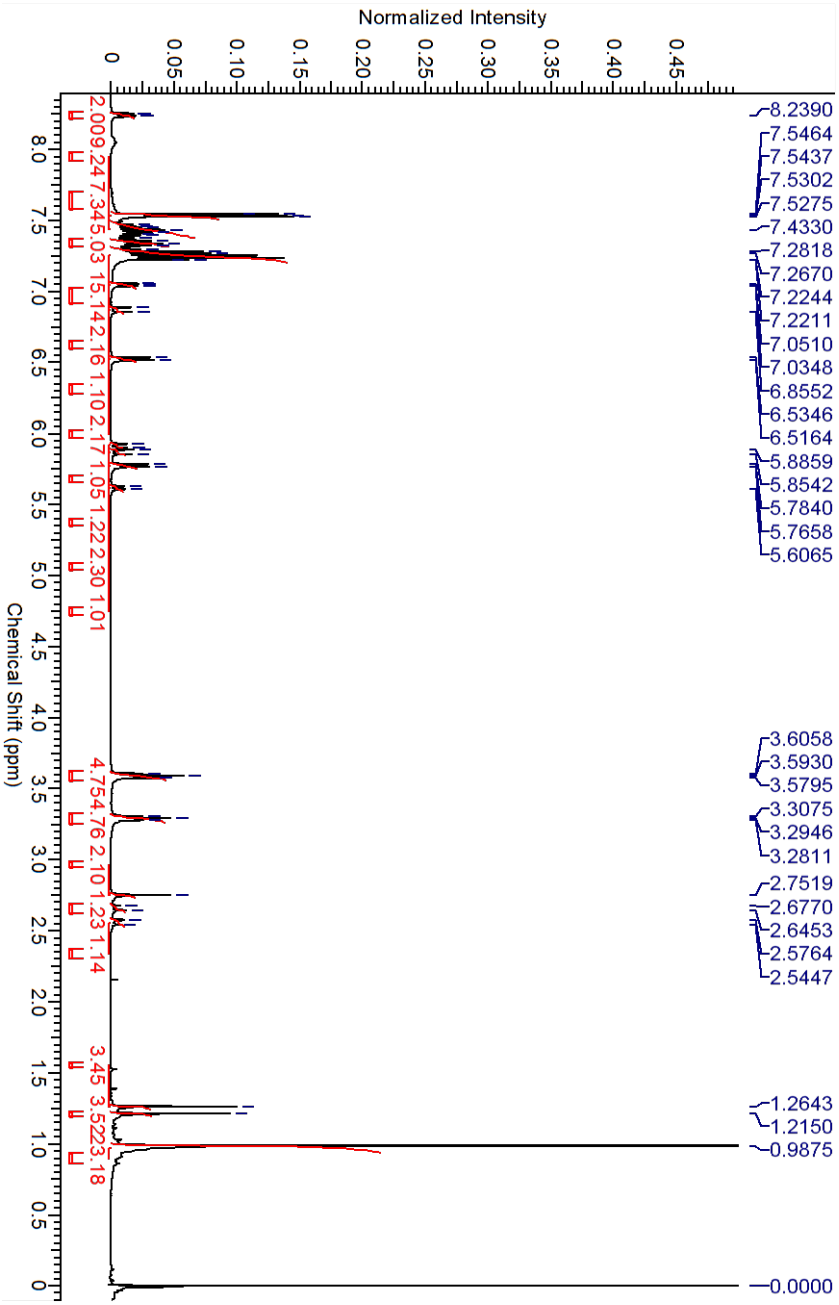

Figure 2.15: Proton NMR Spectra of JRD5.

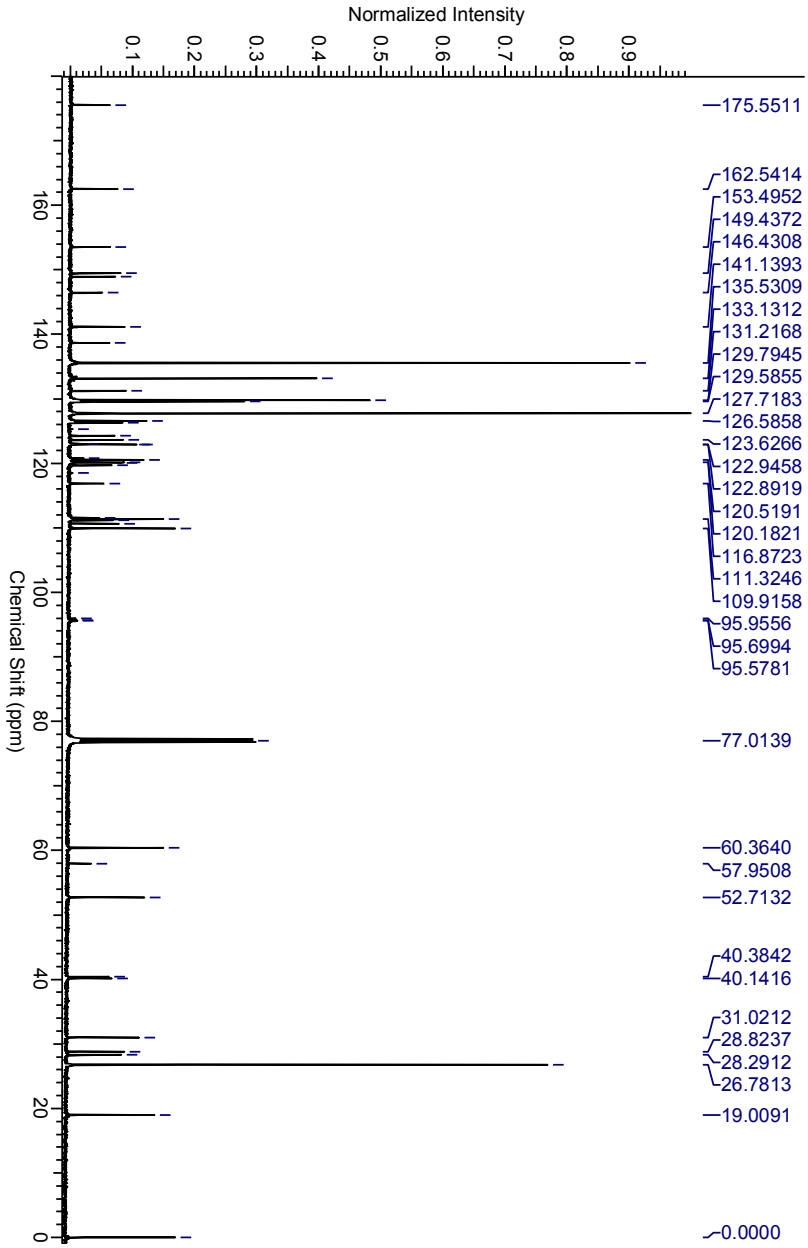

Figure 2.16: Carbon NMR Spectra of JRD5.

2.6.3 KRD1

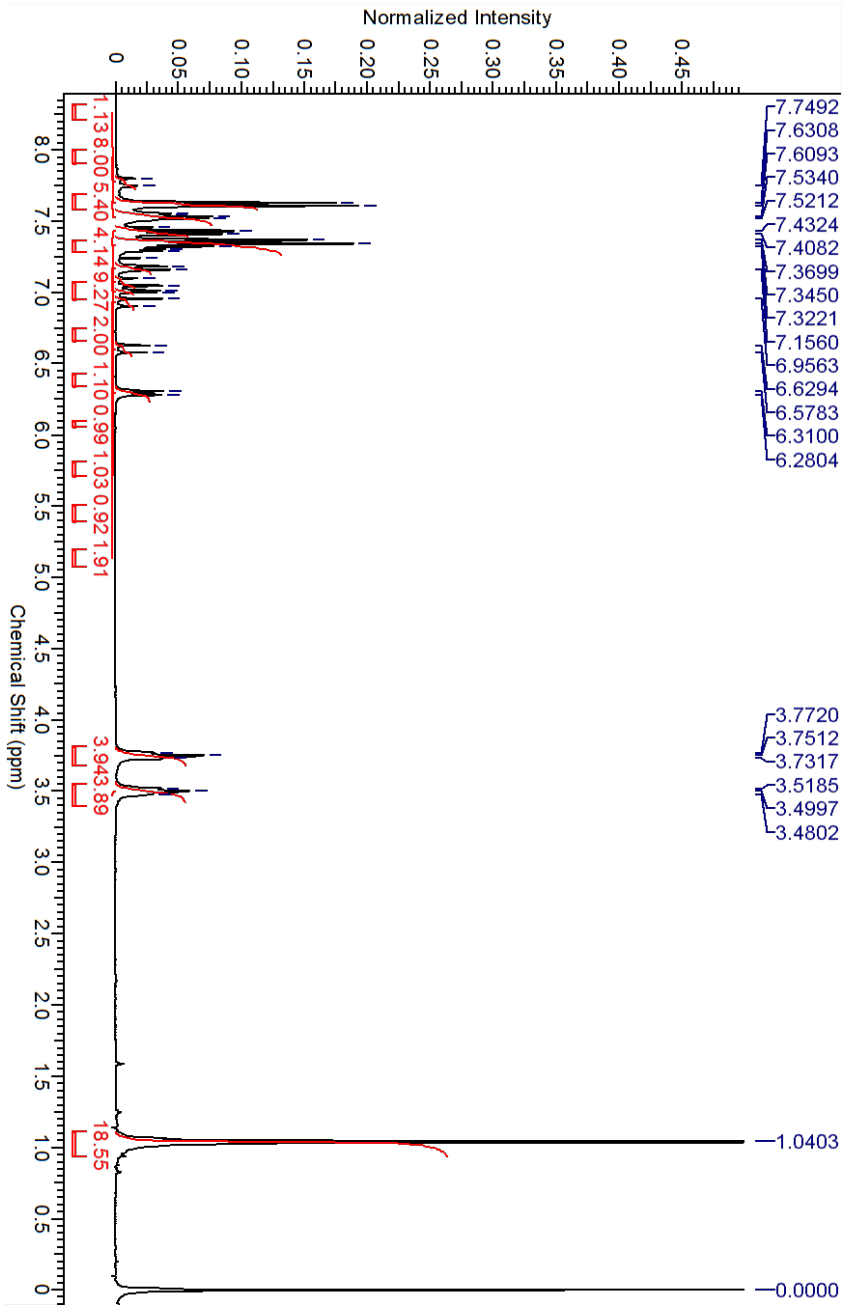

Figure 2.17: Proton NMR Spectra of KRD1.

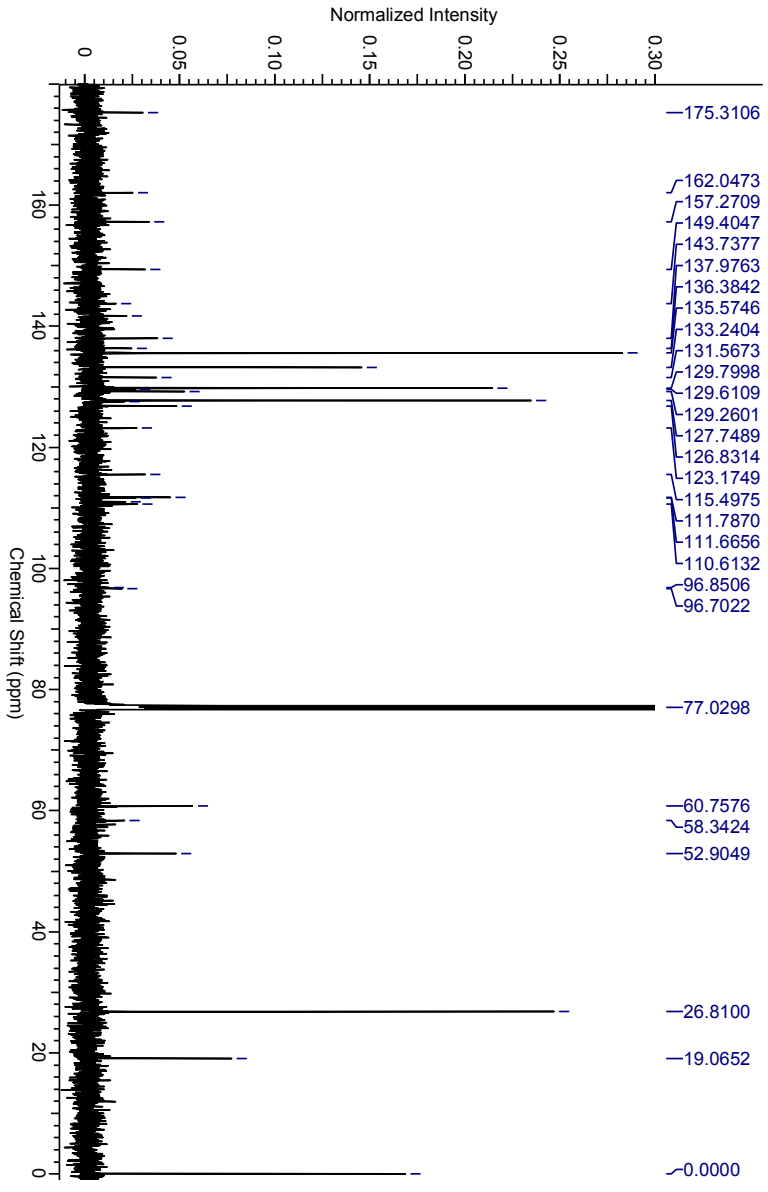

Figure 2.18: Carbon NMR Spectra of KRD1.

2.6.4 JRD2

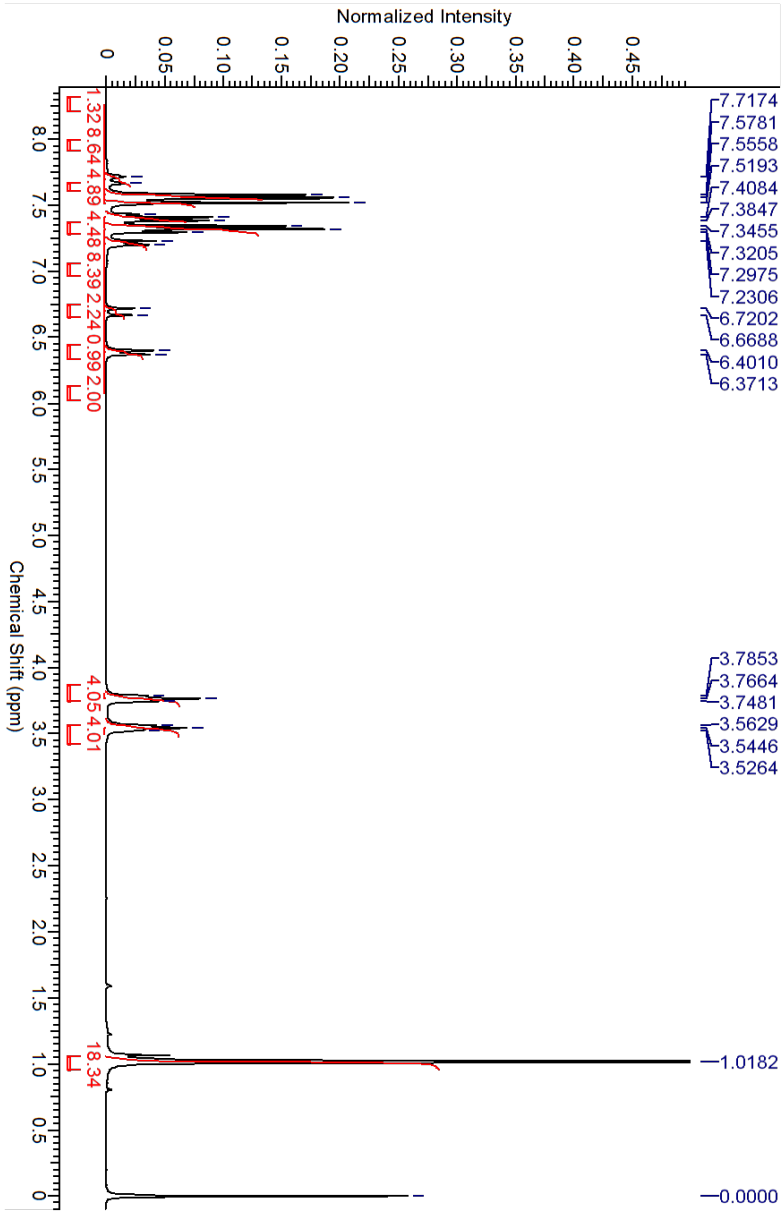

Figure 2.19: Proton NMR Spectra of JRD2.

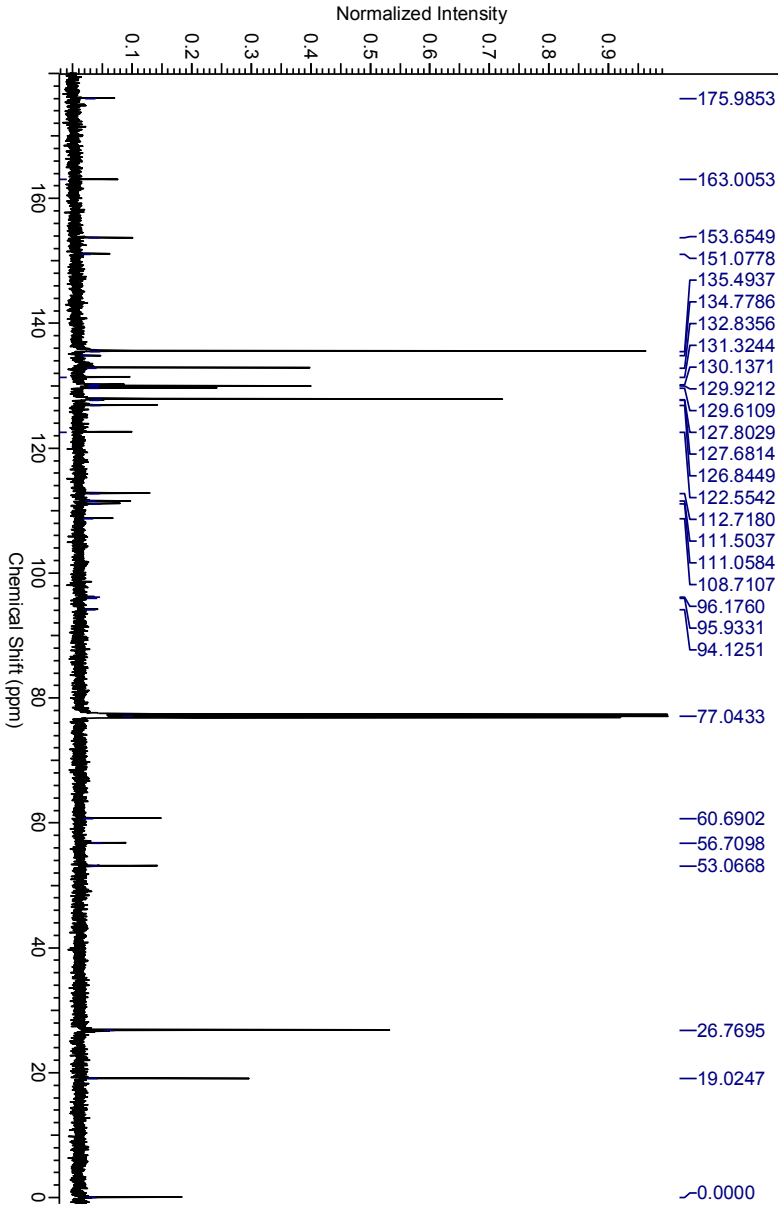

Figure 2.20: Carbon NMR Spectra of JRD2.

2.6.5 HD-BB-MOM

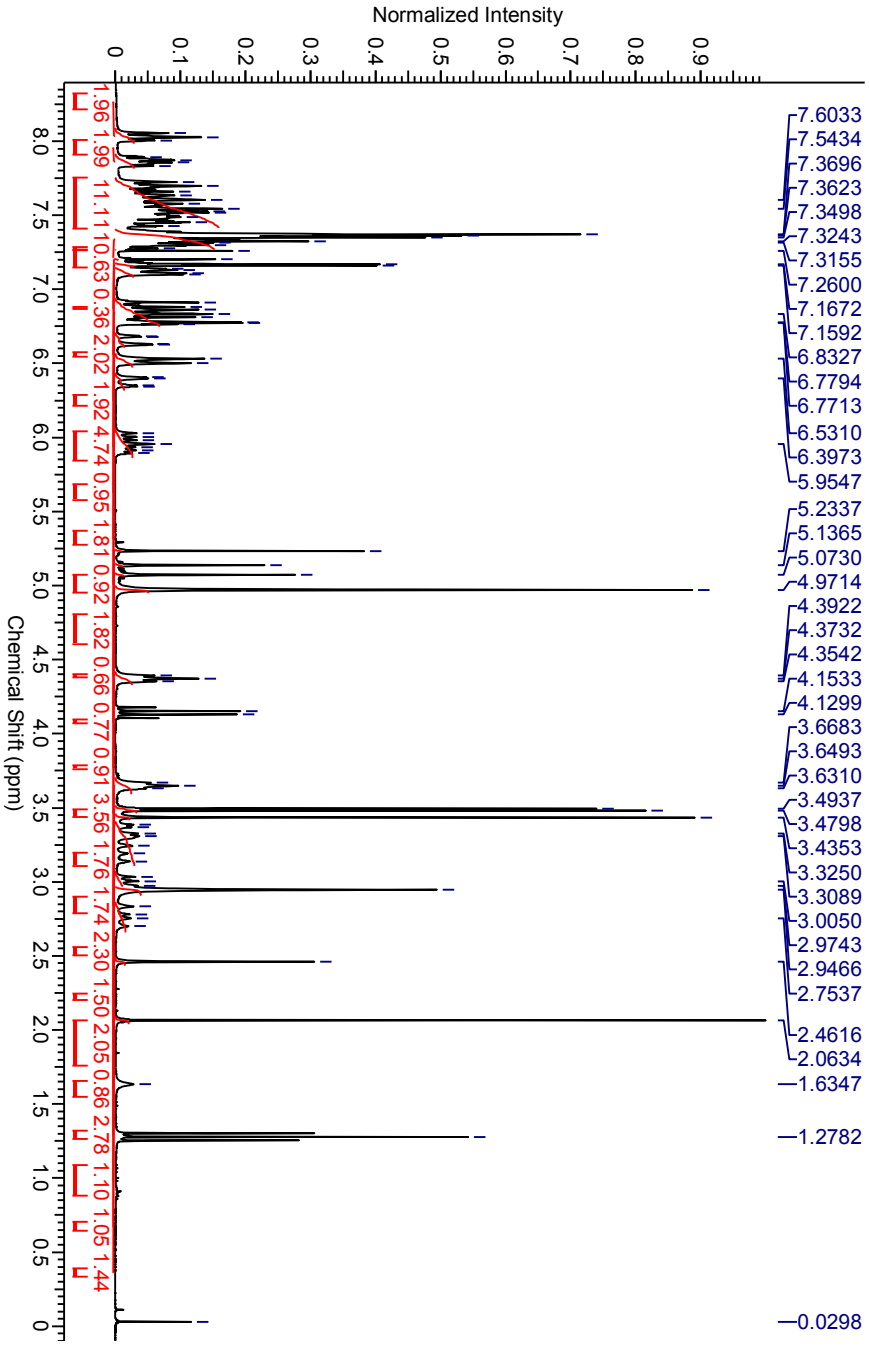

Figure 2.21: Proton NMR Spectra of HD-BB-MOM.

2.7 UV-visible Absorbance Spectra

UV-visible absorbance spectra were measured from both the chloroform solution and thin films for the series of chromophores studied herein. The solution phase absorbance spectra (Figure 2.22) for YLD-124 and JRD1 in chloroform are nearly identical; the main absorption bands are at 786 nm and 788 nm, respectively. Molecular substitution at the bridge led JRD5 to a slight hypsochromic shift from that of YLD-124 and JRD1. In general, λ_{max} for YLD-124, JRD1 and JRD5 in chloroform solution are very similar. However, bridge size and types showed great influence on the optical properties. The absorbance spectra of KRD1, the chromophore with a thiophene bridge, showed hypsochromic shift compared to that of JRD5. Without a bridge, the main absorption band for JRD2 further hypsochromic shifted to 630 nm. Figure 2.23 shows UV-vis spectra as a dependence of the molar absorptivity (ε) on the wavelength in chloroform. The normalized thin film absorbance spectra are shown in Figure 2.24. The tendency of the absorption behavior is similar in thin films as in the solution.

2.7.1 Solution Phase Spectra

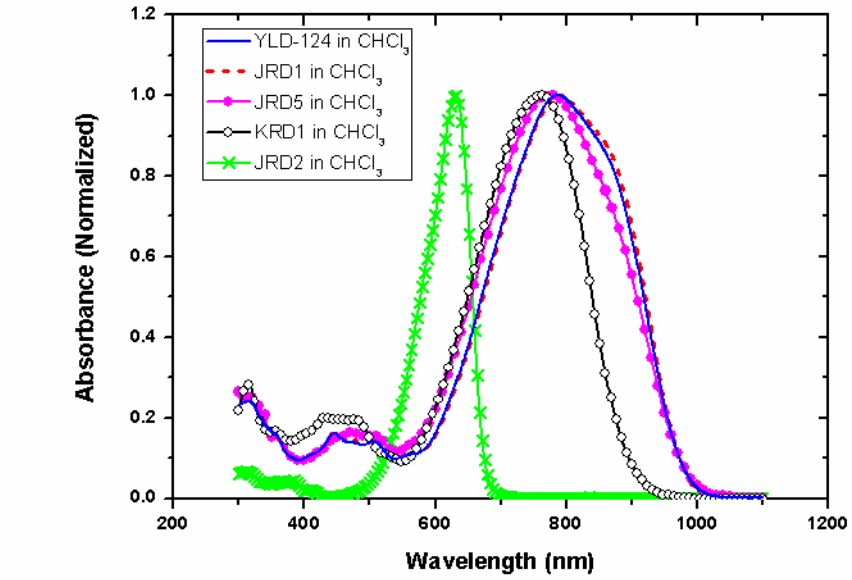

Figure 2.22: Normalized UV-vis spectra in chloroform for YLD-124 (blue solid line), λ_{max} = 786 nm; JRD1 (red dash line), λ_{max} = 788 nm; JRD5 (magenta triangles), λ_{max} = 778 nm; KRD1 (black circles), λ_{max} = 762 nm; and JRD2 (green crosses), λ_{max} = 630 nm.

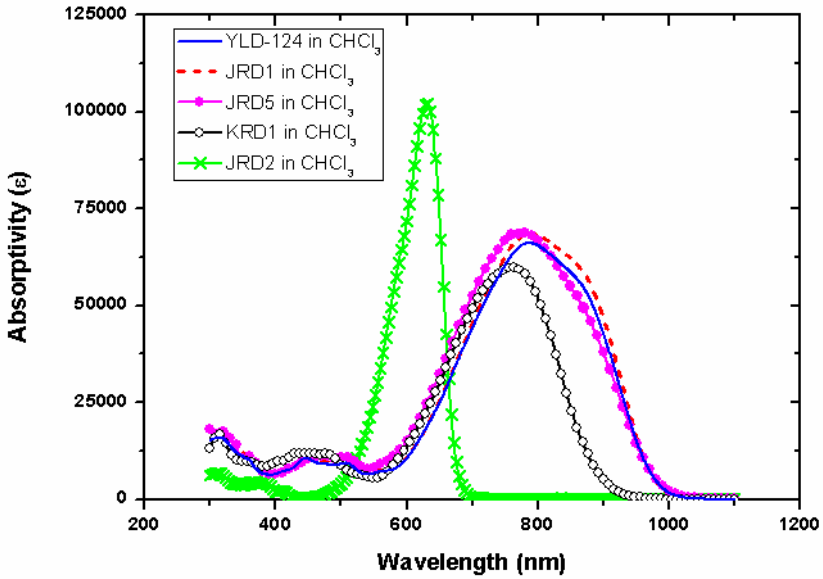

Figure 2.23: UV-vis spectra as a dependence of the molar absorptivity (ε) in chloroform for YLD-124 (blue solid line), $\varepsilon = 6.61 \times 104$; JRD1 (red dash line), $\varepsilon = 6.89 \times 104$; JRD5 (magenta triangles), $\varepsilon = 6.86 \times 104$; KRD1 (black circles), $\varepsilon = 5.98 \times 104$; and JRD2 (green crosses), $\varepsilon = 1.02 \times 105$.

2.7.2 Film Phase Spectra

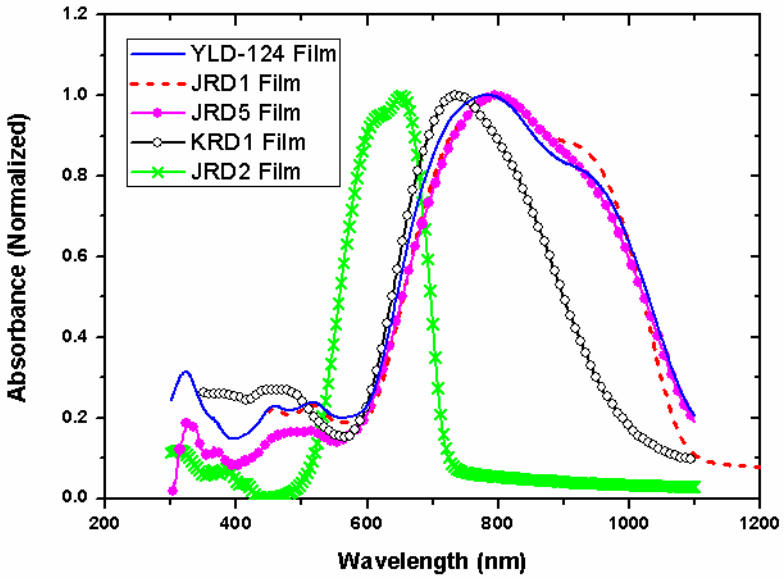

Figure 2.24: Normalized UV-vis thin film spectra for YLD-124 (blue solid line), λ_{max} = 783 nm; JRD1 (red dash line), λ_{max} = 800 nm; JRD5 (magenta triangles), λ_{max} = 795 nm; KRD1 (black circles), λ_{max} = 737 nm; and JRD2 (green crosses), λ_{max} = 652 nm.

2.8 Glass Transition Temperatures

Glass transition temperature (T_g) was measured by Differential Scanning Calorimetry (DSC). A three cycle heat/cool loop was run for each sample under nitrogen at a rate of 10 °C/minute from 0 °C to 150 °C 0 °C to 180 °C, and 0 °C to just under the temperature of decomposition using a TA Instruments Q100 calorimeter with a refrigerated cooling system (RCS). Data were analyzed using TA Instruments Universal Analysis software. Without a polymer host, the T_g values for YLD-124 and JRD1 reduced to 81 °C and 82 °C respectively, which agrees well with other neat chromophores reported so far. [22, 45, 48] This is a disadvantage for neat chromophores in applications since T_g is tightly related to the thermal stability. However, the T_g of JRD5 gained a remarkable increase to 101 °C, which is comparable to

the guest/PMMA material system. Such increase could be attributed to the large, rigid, fused ring moiety carbazole introduced to the bridge for reducing the possibility of lowering T_g due to the additional chromophore substituents with high flexibility and many degrees of rotational freedom. This exploration opens a new avenue to increase T_g for the neat materials with incredible EO performance and calls for further studies. Figure 2.25-3.13 shows the DSC plot of this series of chromophores. Figure 2.30 shows the DSC plot of the comparative choromophore HD-BB-MOM.

2.8.1 YLD-124

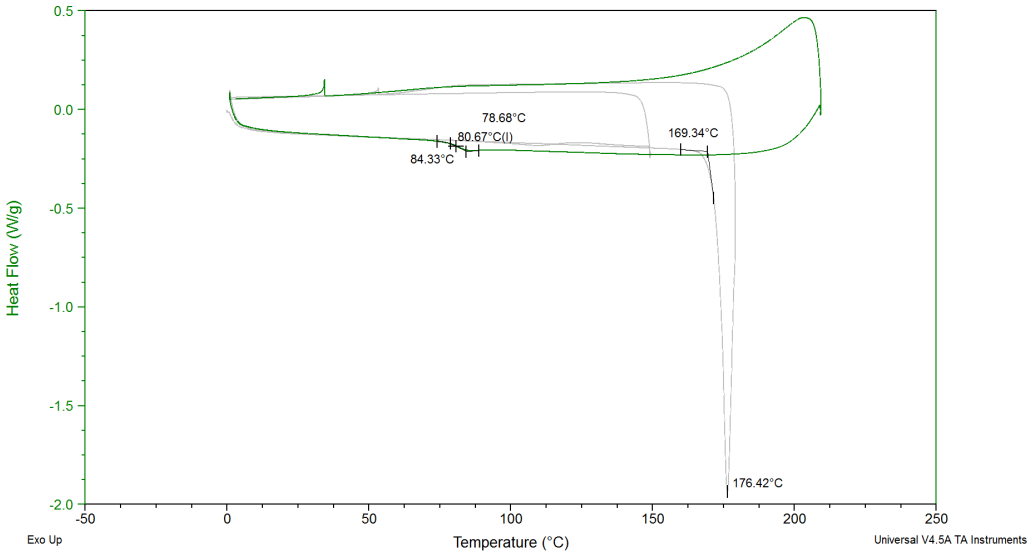

Figure 2.25: DSC plot of YLD-124. T_g = 80.67 °C.

2.8.2 JRD1

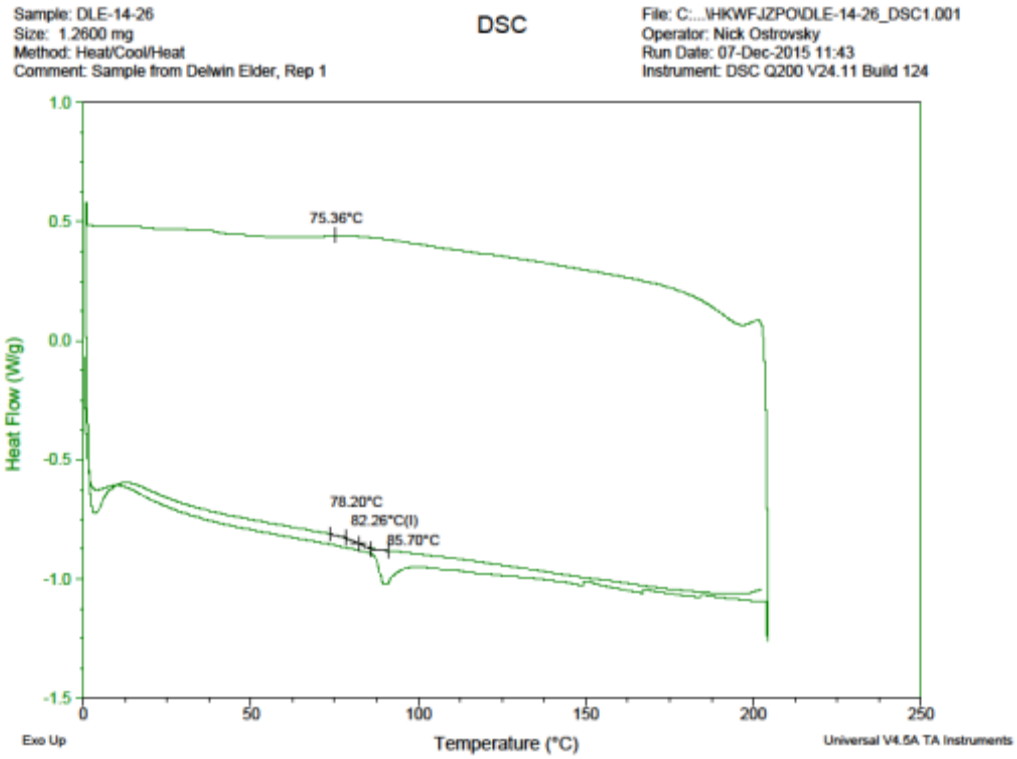

Figure 2.26: DSC plot of JRD1. T_g = 82.26 °C.

2.8.3 JRD5

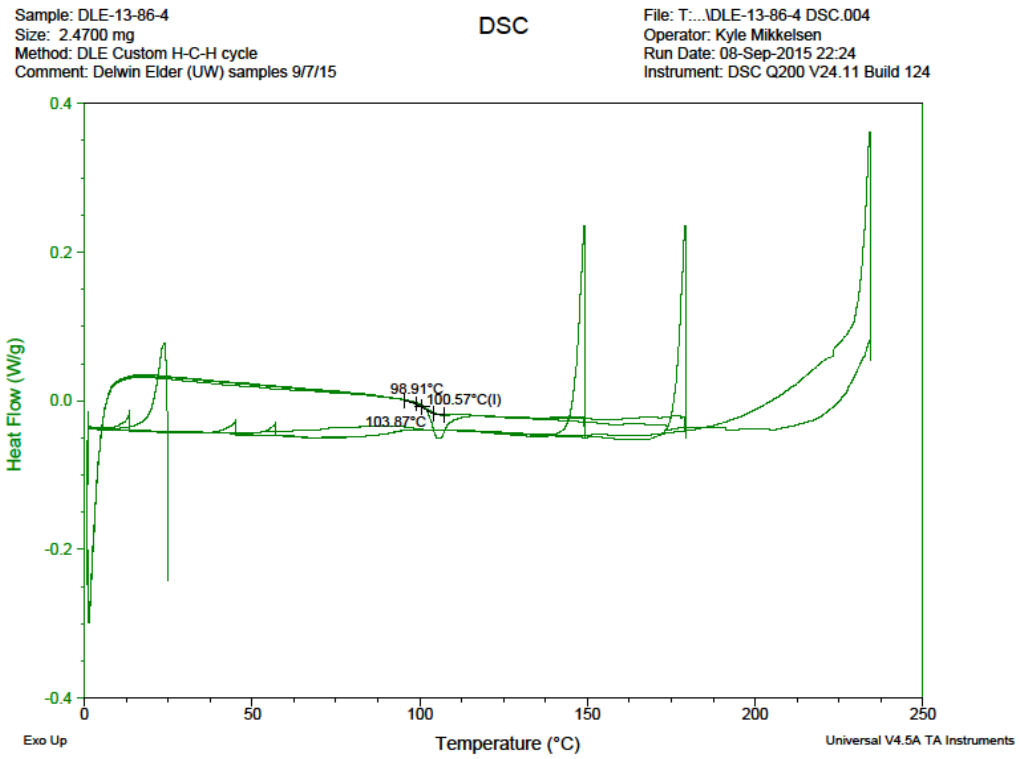

Figure 2.27: DSC plot of JRD5. $T_g = 100.57$ °C.

2.8.4 JRD2

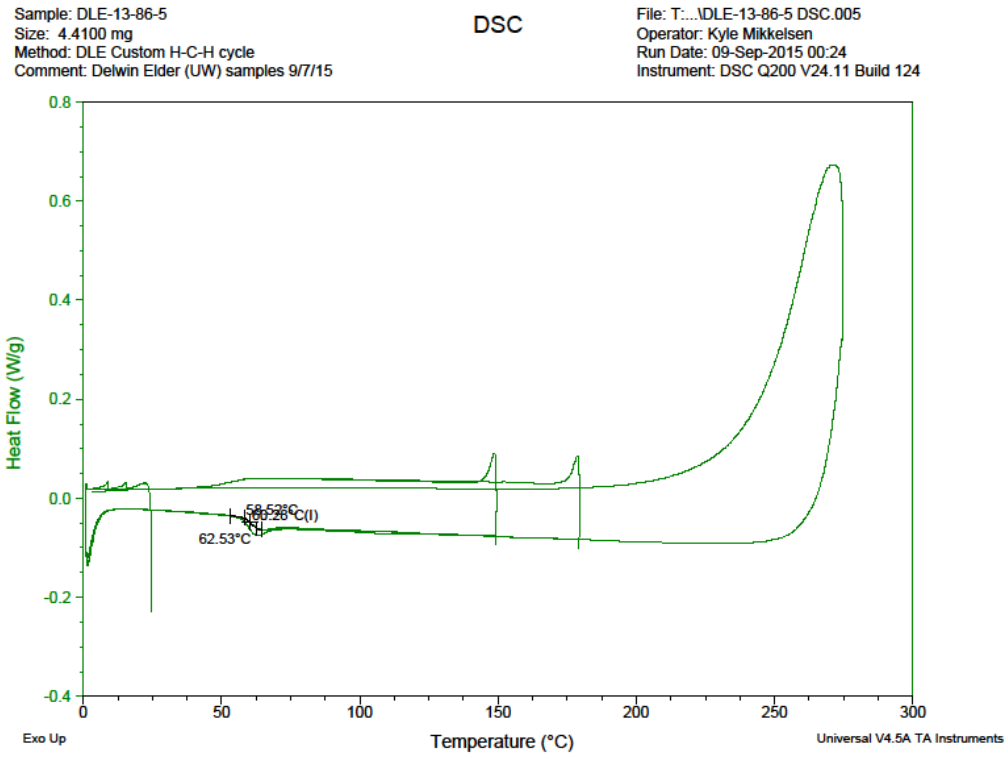

Figure 2.28: DSC plot of JRD2. $T_g = 60.28$ °C.

2.8.5 KRD1

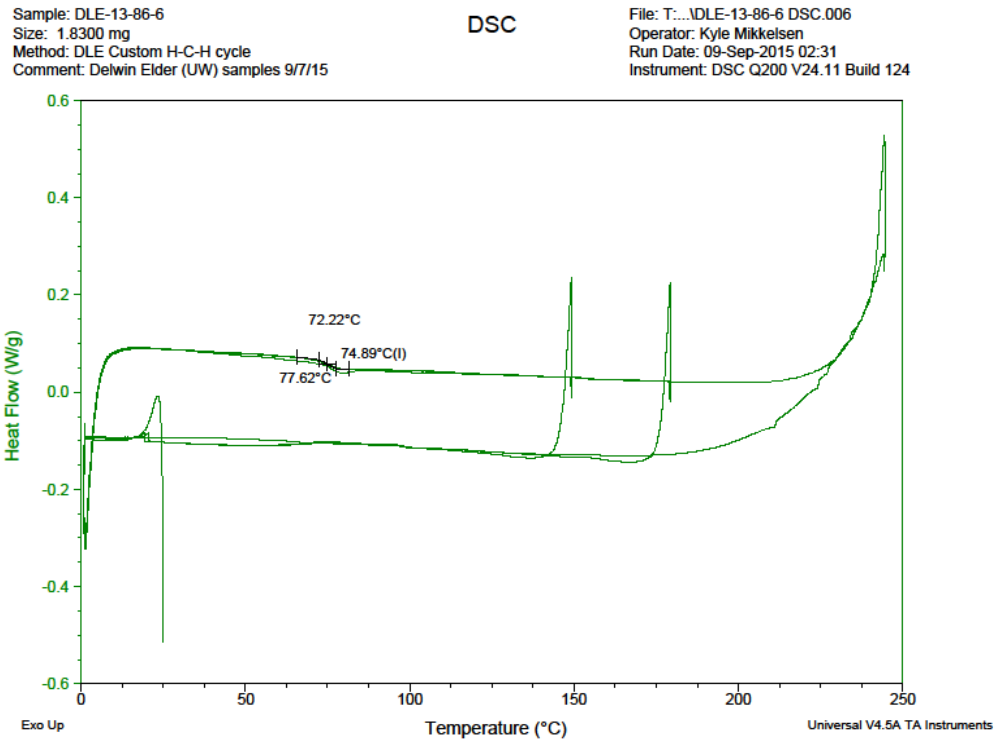

Figure 2.29: DSC plot of KRD1. T_g = 74.89 °C.

2.8.6 HD-BB-MOM

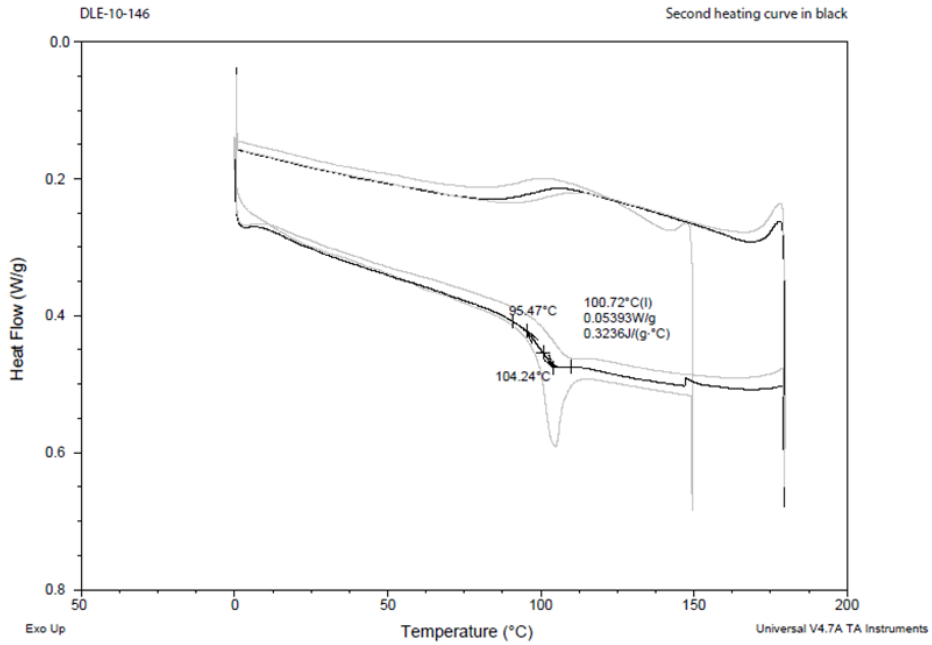

Figure 2.30: DSC plot of HD-BB-MOM. T_g = 100.72 °C.

2.9 The Decomposition Temperature

The decomposition temperatures (T_d) was measured by thermogravametric analysis (TGA). TGA samples were prepared by placing over 1 mg of sample onto a platinum TGA pan. The samples were scanned at a rate of 20 °C/minute from room temperature up to 400 °C. The T_d of YLD-124 is 208 °C. The other four chromophores have increased T_d compared to that of YLD-124. The T_d of JRD1, JRD5, JRD2 and KRD1 is 226.18 °C, 233.07 °C, 271.82 °C, and 239.87 °C, respectively.

2.9.1 YLD-124

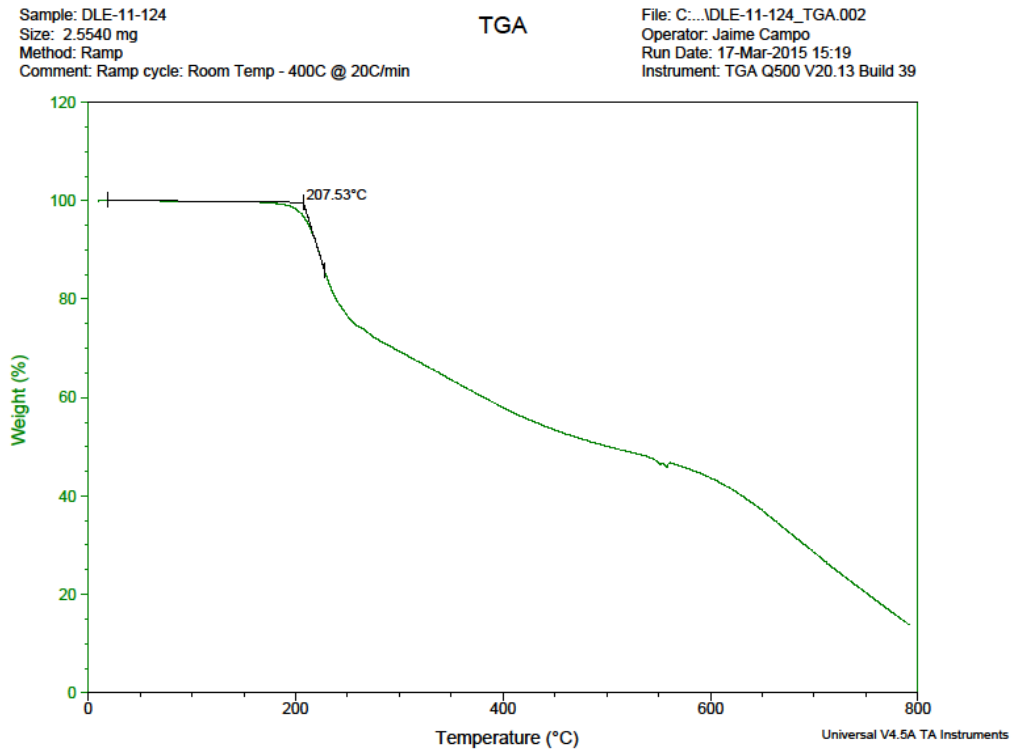

Figure 2.31: TGA plot of YLD-124. T_d=207.53 °C.

2.9.2 JRD1

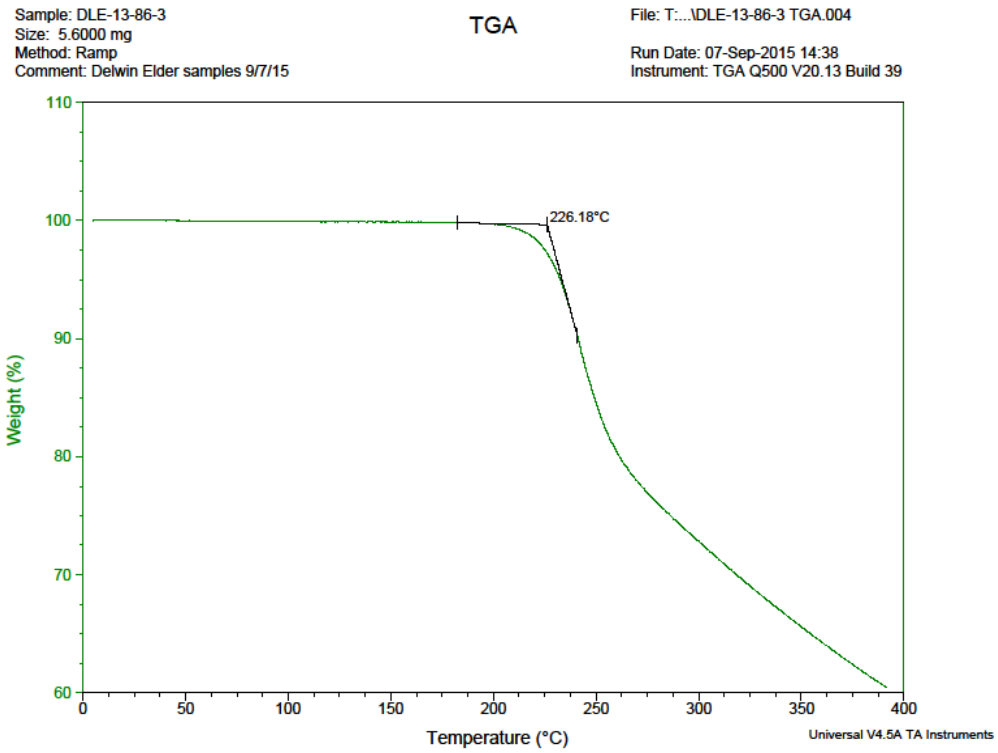

Figure 2.32: TGA plot of JRD1. T_d=226.18 °C.

2.9.3 JRD5

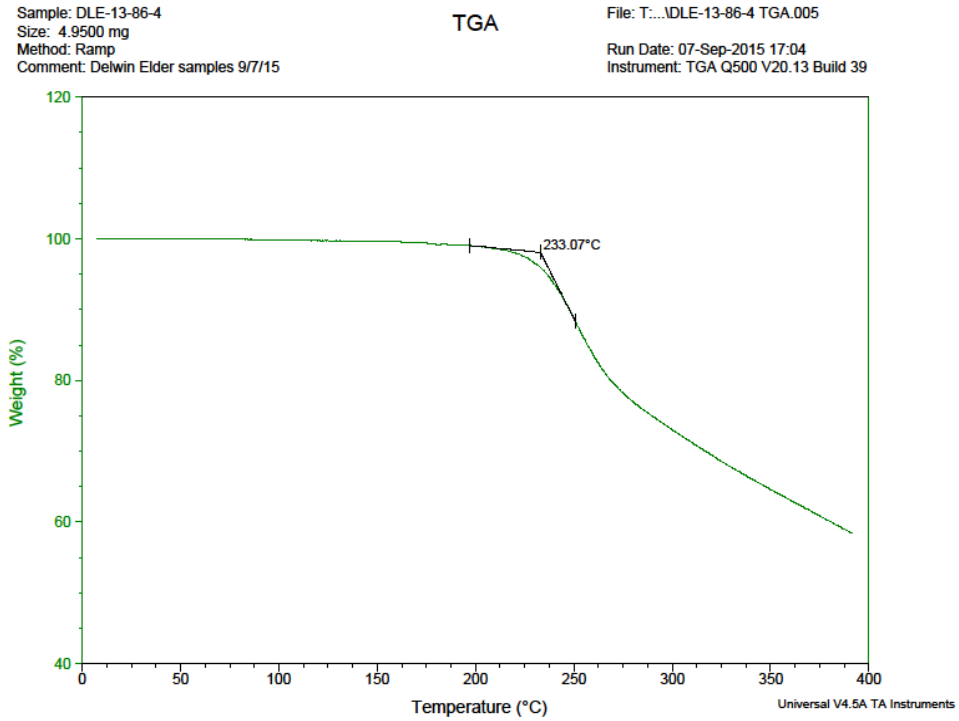

Figure 2.33: TGA plot of JRD5. T_d=233.07 °C.

2.9.4 JRD2

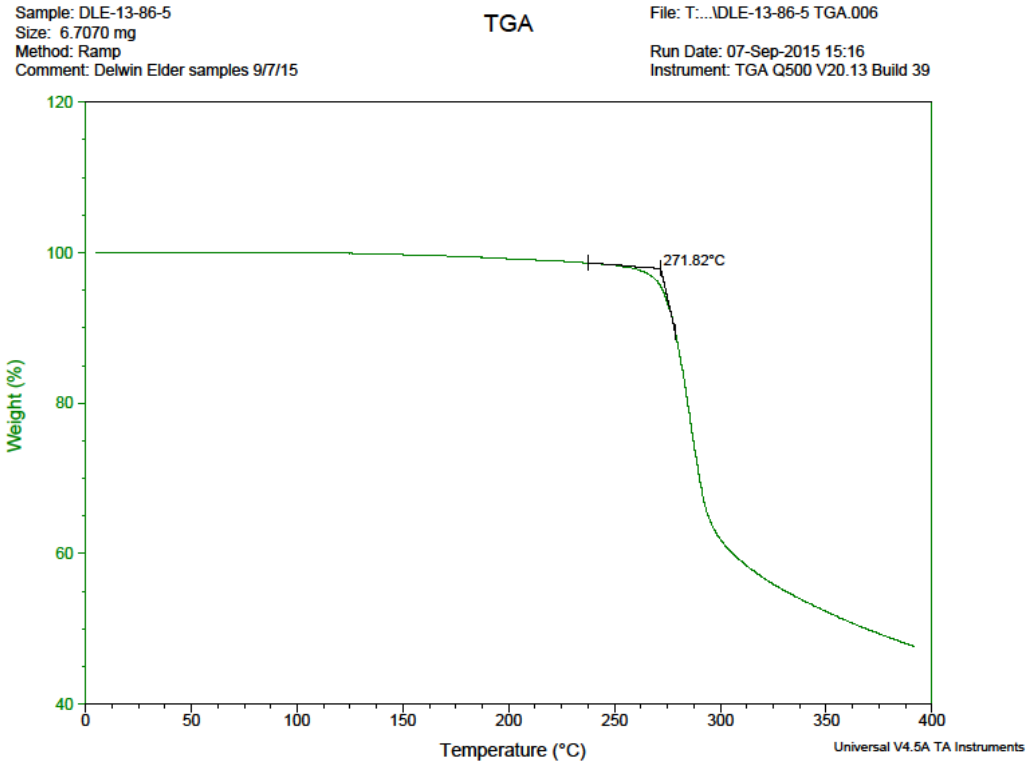

Figure 2.34: TGA plot of JRD2. T_d=271.82 °C.

2.9.5 KRD1

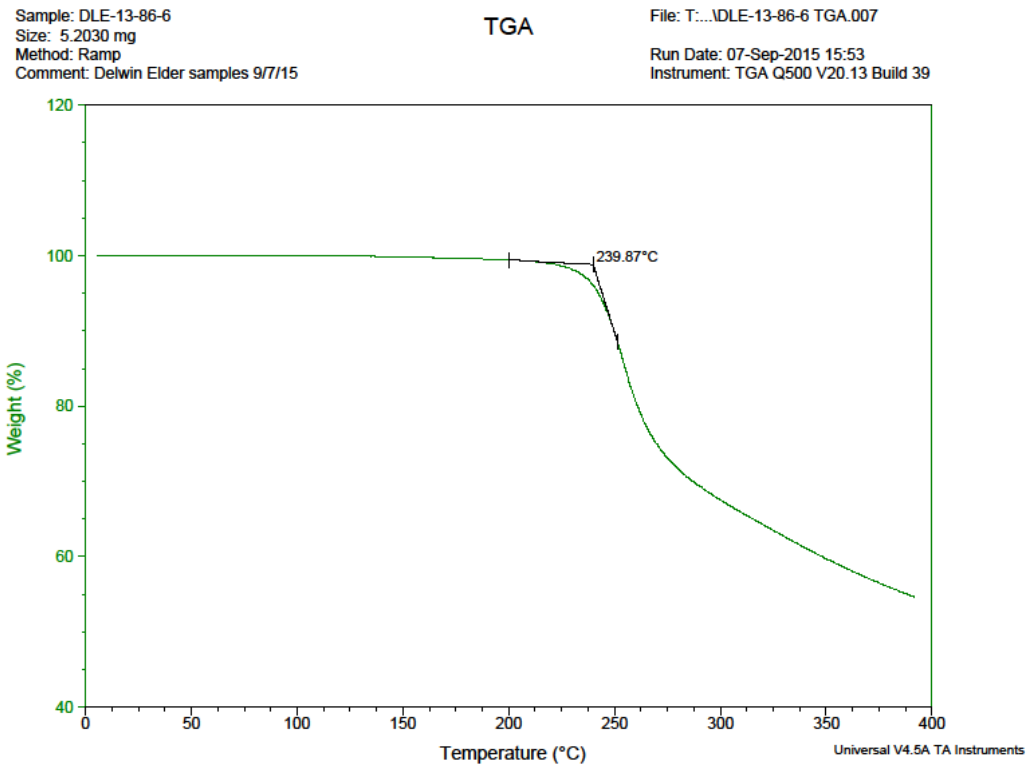

Figure 2.35: TGA plot of KRD1. T_d=239.87 °C.

2.10 Crystal Structure of YLD-124

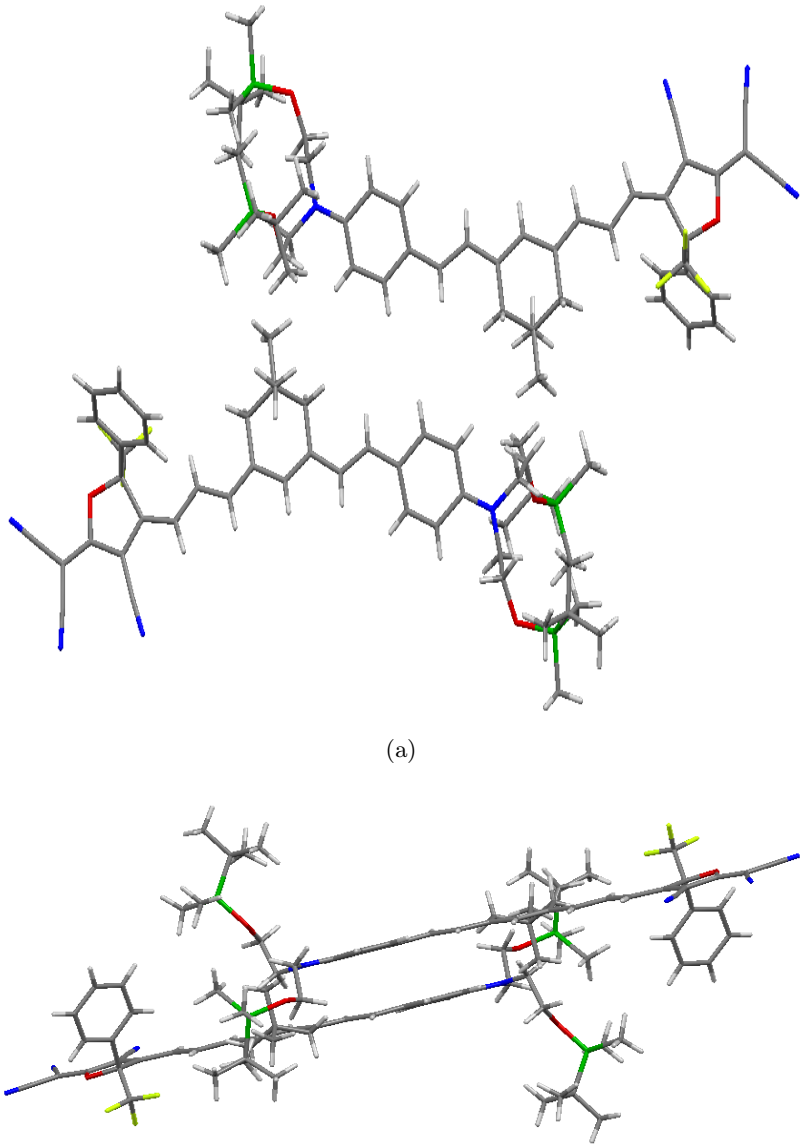

(a)

(b)

Figure 2.36: YLD-124 Crystal Structure, 2 molecules per unit cell, View (a) and (b).

2.10.1 Crystallization of YLD-124

Purified YLD-124 is dissolved in a minimal amount of DCM to form a concentrated ink. The ink is dropped into a scintillation vial which is then filled with cold methanol. The vial is fitted with a rubber septum and narrow gauge needle is placed in the septum such that the DCM can escape as it evaporates from the methanol solution. The vial is placed in a dark dry area. As the DCM evaporates, the molecules dimerize into a non-polar supermolecular structure that is insoluble in methanol and then further undergo polymerization. This process is competing with another process that degrades the chromophore. [30, 86, 87] A shiny, dark-copper colored, and delicate crystalline precipitate is formed over the course of several days. The degraded material is highly soluble in cold methanol and can be washed away without disturbing the crystalline material. The crystals are ribbon like and sub mm in size. The precipitate is filtered from the remaining methanol and washed with additional cold methanol.

2.10.2 Crystallographic Information

The crystal structure data of YLD-124 was collected at -173 °C on a Bruker APEX II single crystal X-ray diffractometer, Mo-radiation. A lustrous, violet ultra-thin plate, measuring $0.30 \times 0.15 \times 0.01$ mm^3 was mounted on a loop with oil. Crystal-to-detector distance was 40 mm and exposure time was 120 seconds per frame for all sets. The scan width was 1°. Data collection was 97.1% complete to 25° in θ. A total of 14385 reflections were collected covering the indices, h = -9 to 9, k = -16 to 16, l = -24 to 27. 8740 reflections were symmetry independent and the $R_{int} = 0.1251$ indicated that the data was of lesser than average quality (0.07). Indexing and unit cell refinement indicated a triclinic lattice. The space group was found to be $P\bar{1}$ (No.2).

The data was integrated and scaled using SAINT, SADABS within the APEX2 software package by Bruker.

Solution by direct methods (SHELXS, SIR97[11]) produced a complete heavy atom phasing model consistent with the proposed structure. The structure was completed by difference Fourier synthesis with SHELXL97. [88, 89] Scattering factors are from Waasmair and Kirfel.

[90] Hydrogen atoms were placed in geometrically idealised positions and constrained to ride on their parent atoms with C—H distances in the range 0.95-1.00 Angstrom. Isotropic thermal parameters U_{eq} were fixed such that they were 1.2 U_{eq} of their parent atom U_{eq} for CH's and 1.5 U_{eq} of their parent atom U_{eq} in case of methyl groups. All non-hydrogen atoms were refined anisotropically by full-matrix least-squares. The structure is of high quality and ready for publication. Table 2.3 summarizes the data collection details. Atomic coordinates and equivalent isotropic displacement parameters are listed in Table 2.4. Information about bond lengths and angles could be found in Table 2.5. Figure 2.36 shows YLD-124 crystal structure.

Table 2.4: Atomic coordinates ($\times 10^4$) and equivalent isotropic displacement parameters ($Å^2 \times 10^3$) for yld1240m. U(eq) is defined as one third of the trace of the orthogonalized U^{ij} tensor.

	x	**y**	**z**	U(eq)
C(1)	-5875(13)	13184(8)	6282(5)	35(3)
C(2)	-5120(12)	12569(7)	5793(5)	33(3)
C(3)	-4349(13)	11800(8)	5978(5)	36(3)
C(4)	-4527(13)	11972(7)	6670(5)	30(2)
C(5)	-2920(12)	12298(7)	7121(6)	35(3)
C(6)	-1324(13)	12109(8)	6929(6)	39(3)
C(7)	93(14)	12525(9)	7332(7)	49(3)
C(8)	-21(14)	13043(9)	7920(6)	43(3)
C(9)	-1617(16)	13258(9)	8102(6)	50(3)
C(10)	-3032(14)	12850(9)	7697(6)	43(3)
C(11)	-5607(15)	11143(8)	6805(5)	37(3)
C(12)	-6734(13)	14027(7)	6336(5)	36(3)
C(13)	-7308(14)	14516(8)	6924(6)	39(3)
C(14)	-7028(13)	14424(8)	5848(5)	32(2)

Continued on next page

Table 2.4 – *Continued from previous page*

	x	**y**	**z**	U(eq)
C(15)	-5137(12)	12712(8)	5196(6)	31(2)
C(16)	-3575(13)	11035(7)	5587(6)	37(3)
C(17)	-2765(13)	10230(7)	5713(6)	37(3)
C(18)	-2042(12)	9553(8)	5268(6)	42(3)
C(19)	-1218(13)	8737(8)	5343(5)	36(3)
C(20)	-1089(14)	8433(8)	5949(5)	42(3)
C(21)	530(13)	7845(7)	6028(5)	32(2)
C(22)	511(12)	6976(8)	5455(5)	32(2)
C(23)	274(12)	7254(8)	4858(5)	38(3)
C(24)	-553(13)	8095(7)	4836(6)	36(3)
C(25)	2117(13)	8523(9)	6136(6)	43(3)
C(26)	411(14)	7408(9)	6590(5)	41(3)
C(27)	808(12)	6667(7)	4312(5)	30(2)
C(28)	1689(12)	5821(7)	4281(5)	33(2)
C(29)	2303(12)	5230(7)	3747(5)	31(2)
C(30)	1947(13)	5301(8)	3148(5)	34(2)
C(31)	2523(15)	4710(9)	2657(6)	43(3)
C(32)	3609(14)	3902(8)	2730(6)	40(3)
C(33)	3945(13)	3795(8)	3324(5)	37(3)
C(34)	3302(13)	4434(7)	3828(6)	37(3)
C(35)	5256(15)	2508(8)	2299(6)	48(3)
C(36)	4130(20)	1591(10)	2309(6)	63(4)
C(37)	1980(18)	225(11)	542(7)	71(4)
C(38)	3650(20)	-803(10)	1451(7)	73(4)
C(39)	133(19)	-52(11)	1630(7)	64(4)
C(40)	-970(20)	802(14)	1563(9)	95(6)
C(41)	410(20)	-59(12)	2308(7)	81(5)

Continued on next page

Table 2.4 – *Continued from previous page*

	x	**y**	**z**	U(eq)
C(42)	-770(20)	-1014(14)	1231(8)	87(5)
C(43)	3771(15)	3373(9)	1627(6)	50(3)
C(44)	5000(20)	4105(12)	1441(7)	72(4)
C(45)	5390(30)	1984(15)	233(10)	118(7)
C(46)	5070(20)	3511(13)	-453(7)	84(5)
C(47)	8124(19)	3617(14)	464(8)	80(5)
C(48)	9050(30)	3164(16)	-90(10)	113(7)
C(49)	8820(50)	3320(30)	1008(15)	203(14)
C(50)	8470(40)	4710(20)	647(14)	167(10)
N(1)	-7714(13)	14878(8)	7378(6)	48(3)
N(2)	-7343(11)	14795(7)	5452(5)	43(2)
N(3)	-5146(10)	12761(7)	4708(5)	40(2)
N(4)	4157(12)	3302(7)	2236(5)	42(2)
O(1)	-5623(8)	12801(5)	6786(3)	37(2)
F(2)	-7007(7)	10912(5)	6407(3)	49(2)
F(1)	-6105(7)	11419(4)	7366(3)	44(2)
F(3)	-4765(7)	10335(4)	6781(3)	44(2)
O(2)	3129(14)	1262(7)	1735(5)	75(3)
O(3)	4736(13)	4026(7)	787(4)	68(3)
Si(1)	2217(5)	180(3)	1360(2)	58(1)
Si(2)	5882(6)	3310(3)	286(2)	66(1)

Table 2.3: Crystallographic data for YLD-124.

Empirical formula	$C_{50}H_{63}F_3N_4O_3Si_2$	
Formula weight	881.22	
Temperature	100(2) K	
Wavelength	0.71073 Å	
Crystal system	Triclinic	
Space group	P -1	
Unit cell dimensions	a = 7.905(7) Å	α = 105.216(17)°.
	b = 13.915(13) Å	β = 95.622(15)°.
	c = 22.51(2) Å	γ = 91.927(16)°.
Volume	2373(4) $Å^3$	
Z	2	
Density (calculated)	1.233 Mg/m^3	
Absorption coefficient	0.132 mm^{-1}	
F(000)	940	
Crystal size	0.30 x 0.15 x 0.01 mm^3	
Theta range for data collection	2.59 to 25.86°	
Index ranges	-9<=h<=9, -16<=k<=16, -24<=l<=27	
Reflections collected	14385	
Independent reflections	8740 [R(int) = 0.1251]	
Completeness to theta = 25.00°	97.10%	
Max. and min. transmission 0.9987 and 0.9615		
Refinement method	Full-matrix least-squares on F^2	
Data / restraints / parameters	8740 / 66 / 573	
Goodness-of-fit on F^2	1.102	
Final R indices [I>2sigma(I)]	R1 = 0.1447, wR2 = 0.3453	
R indices (all data)	R1 = 0.2679, wR2 = 0.4199	
Extinction coefficient	0.025(5)	
Largest diff. peak and hole	0.591 and -0.439 e.$Å^{-3}$	

Table 2.5: Bond lengths Å, and angles °, for yld124 0m.

C(1)-C(12)	1.360(14)
C(1)-O(1)	1.373(13)
C(1)-C(2)	1.404(15)
C(2)-C(3)	1.385(14)
C(2)-C(15)	1.407(16)
C(3)-C(16)	1.392(14)
C(3)-C(4)	1.535(15)
C(4)-O(1)	1.450(11)
C(4)-C(5)	1.521(15)
C(4)-C(11)	1.524(15)
C(5)-C(10)	1.334(16)
C(5)-C(6)	1.385(14)
C(6)-C(7)	1.376(16)
C(6)-H(6)	0.95
C(7)-C(8)	1.344(17)
C(7)-H(7)	0.95
C(8)-C(9)	1.383(17)
C(8)-H(8)	0.95
C(9)-C(10)	1.375(17)
C(9)-H(9)	0.95
C(10)-H(10)	0.95
C(11)-F(3)	1.317(11)
C(11)-F(1)	1.323(13)
C(11)-F(2)	1.327(12)
C(12)-C(14)	1.357(16)

Continued on next page

Table 2.5 – *Continued from previous page*

C(12)-C(13)	1.446(18)
C(13)-N(1)	1.097(14)
C(14)-N(2)	1.152(13)
C(15)-N(3)	1.119(13)
C(16)-C(17)	1.388(14)
C(16)-H(16)	0.95
C(17)-C(18)	1.368(15)
C(17)-H(17)	0.95
C(18)-C(19)	1.368(15)
C(18)-H(18)	0.95
C(19)-C(24)	1.411(15)
C(19)-C(20)	1.526(16)
C(20)-C(21)	1.563(14)
C(20)-H(20A)	0.99
C(20)-H(20B)	0.99
C(21)-C(25)	1.504(15)
C(21)-C(22)	1.518(15)
C(21)-C(26)	1.550(15)
C(22)-C(23)	1.490(15)
C(22)-H(22A)	0.99
C(22)-H(22B)	0.99
C(23)-C(24)	1.369(14)
C(23)-C(27)	1.398(15)
C(24)-H(24)	0.95
C(25)-H(25A)	0.98
C(25)-H(25B)	0.98
C(25)-H(25C)	0.98

Continued on next page

Table 2.5 – *Continued from previous page*

C(26)-H(26A)	0.98
C(26)-H(26B)	0.98
C(26)-H(26C)	0.98
C(27)-C(28)	1.377(13)
C(27)-H(27)	0.95
C(28)-C(29)	1.407(15)
C(28)-H(28)	0.95
C(29)-C(30)	1.381(15)
C(29)-C(34)	1.422(14)
C(30)-C(31)	1.323(15)
C(30)-H(30)	0.95
C(31)-C(32)	1.471(15)
C(31)-H(31)	0.95
C(32)-N(4)	1.323(14)
C(32)-C(33)	1.386(16)
C(33)-C(34)	1.397(15)
C(33)-H(33)	0.95
C(34)-H(34)	0.95
C(35)-N(4)	1.455(13)
C(35)-C(36)	1.535(19)
C(35)-H(35A)	0.99
C(35)-H(35B)	0.99
C(36)-O(2)	1.403(15)
C(36)-H(36A)	0.99
C(36)-H(36B)	0.99
C(37)-Si(1)	1.851(16)
C(37)-H(37A)	0.98

Continued on next page

Table 2.5 – *Continued from previous page*

C(37)-H(37B)	0.98
C(37)-H(37C)	0.98
C(38)-Si(1)	1.844(14)
C(38)-H(38A)	0.98
C(38)-H(38B)	0.98
C(38)-H(38C)	0.98
C(39)-C(42)	1.51(2)
C(39)-C(41)	1.52(2)
C(39)-C(40)	1.53(2)
C(39)-Si(1)	1.857(15)
C(40)-H(40A)	0.98
C(40)-H(40B)	0.98
C(40)-H(40C)	0.98
C(41)-H(41A)	0.98
C(41)-H(41B)	0.98
C(41)-H(41C)	0.98
C(42)-H(42A)	0.98
C(42)-H(42B)	0.98
C(42)-H(42C)	0.98
C(43)-N(4)	1.405(16)
C(43)-C(44)	1.548(19)
C(43)-H(43A)	0.99
C(43)-H(43B)	0.99
C(44)-O(3)	1.443(17)
C(44)-H(44A)	0.99
C(44)-H(44B)	0.99
C(45)-Si(2)	1.84(2)

Continued on next page

Table 2.5 – *Continued from previous page*

C(45)-H(45A)	0.98
C(45)-H(45B)	0.98
C(45)-H(45C)	0.98
C(46)-Si(2)	1.817(18)
C(46)-H(46A)	0.98
C(46)-H(46B)	0.98
C(46)-H(46C)	0.98
C(47)-C(49)	1.46(3)
C(47)-C(50)	1.47(3)
C(47)-C(48)	1.51(2)
C(47)-Si(2)	1.791(16)
C(48)-H(48A)	0.98
C(48)-H(48B)	0.98
C(48)-H(48C)	0.98
C(49)-H(49A)	0.9801
C(49)-H(49B)	0.9801
C(49)-H(49C)	0.9801
C(50)-H(50A)	0.98
C(50)-H(50B)	0.98
C(50)-H(50C)	0.98
O(2)-Si(1)	1.625(10)
O(3)-Si(2)	1.659(11)
C(12)-C(1)-O(1)	119.0(10)
C(12)-C(1)-C(2)	132.9(11)
O(1)-C(1)-C(2)	108.2(9)
C(3)-C(2)-C(1)	110.6(10)

Continued on next page

Table 2.5 – *Continued from previous page*

C(3)-C(2)-C(15)	124.5(9)
C(1)-C(2)-C(15)	124.9(9)
C(2)-C(3)-C(16)	124.3(11)
C(2)-C(3)-C(4)	107.0(8)
C(16)-C(3)-C(4)	128.7(9)
O(1)-C(4)-C(5)	106.7(8)
O(1)-C(4)-C(11)	102.5(8)
C(5)-C(4)-C(11)	113.3(8)
O(1)-C(4)-C(3)	102.0(7)
C(5)-C(4)-C(3)	117.4(9)
C(11)-C(4)-C(3)	112.8(9)
C(10)-C(5)-C(6)	118.9(11)
C(10)-C(5)-C(4)	119.8(9)
C(6)-C(5)-C(4)	121.1(11)
C(7)-C(6)-C(5)	118.9(11)
C(7)-C(6)-H(6)	120.6
C(5)-C(6)-H(6)	120.6
C(8)-C(7)-C(6)	122.0(11)
C(8)-C(7)-H(7)	119
C(6)-C(7)-H(7)	119
C(7)-C(8)-C(9)	118.6(11)
C(7)-C(8)-H(8)	120.7
C(9)-C(8)-H(8)	120.7
C(10)-C(9)-C(8)	118.9(12)
C(10)-C(9)-H(9)	120.6
C(8)-C(9)-H(9)	120.6
C(5)-C(10)-C(9)	122.3(11)

Continued on next page

Table 2.5 – *Continued from previous page*

C(5)-C(10)-H(10)	118.8
C(9)-C(10)-H(10)	118.8
F(3)-C(11)-F(1)	106.4(9)
F(3)-C(11)-F(2)	109.3(9)
F(1)-C(11)-F(2)	106.9(9)
F(3)-C(11)-C(4)	112.1(9)
F(1)-C(11)-C(4)	111.5(9)
F(2)-C(11)-C(4)	110.4(9)
C(14)-C(12)-C(1)	120.9(10)
C(14)-C(12)-C(13)	119.8(9)
C(1)-C(12)-C(13)	119.4(10)
N(1)-C(13)-C(12)	178.3(13)
N(2)-C(14)-C(12)	176.1(11)
N(3)-C(15)-C(2)	175.5(11)
C(17)-C(16)-C(3)	129.9(11)
C(17)-C(16)-H(16)	115
C(3)-C(16)-H(16)	115
C(18)-C(17)-C(16)	121.8(11)
C(18)-C(17)-H(17)	119.1
C(16)-C(17)-H(17)	119.1
C(19)-C(18)-C(17)	126.5(12)
C(19)-C(18)-H(18)	116.7
C(17)-C(18)-H(18)	116.7
C(18)-C(19)-C(24)	120.1(11)
C(18)-C(19)-C(20)	122.6(10)
C(24)-C(19)-C(20)	117.1(9)
C(19)-C(20)-C(21)	111.7(9)

Continued on next page

Table 2.5 – *Continued from previous page*

C(19)-C(20)-H(20A)	109.3
C(21)-C(20)-H(20A)	109.3
C(19)-C(20)-H(20B)	109.3
C(21)-C(20)-H(20B)	109.3
H(20A)-C(20)-H(20B)	107.9
C(25)-C(21)-C(22)	112.3(9)
C(25)-C(21)-C(26)	109.7(9)
C(22)-C(21)-C(26)	107.7(8)
C(25)-C(21)-C(20)	110.5(9)
C(22)-C(21)-C(20)	108.0(9)
C(26)-C(21)-C(20)	108.5(9)
C(23)-C(22)-C(21)	114.6(9)
C(23)-C(22)-H(22A)	108.6
C(21)-C(22)-H(22A)	108.6
C(23)-C(22)-H(22B)	108.6
C(21)-C(22)-H(22B)	108.6
H(22A)-C(22)-H(22B)	107.6
C(24)-C(23)-C(27)	118.6(11)
C(24)-C(23)-C(22)	119.0(10)
C(27)-C(23)-C(22)	122.4(10)
C(23)-C(24)-C(19)	124.9(11)
C(23)-C(24)-H(24)	117.6
C(19)-C(24)-H(24)	117.6
C(21)-C(25)-H(25A)	109.5
C(21)-C(25)-H(25B)	109.5
H(25A)-C(25)-H(25B)	109.5
C(21)-C(25)-H(25C)	109.5

Continued on next page

Table 2.5 – *Continued from previous page*

H(25A)-C(25)-H(25C)	109.5
H(25B)-C(25)-H(25C)	109.5
C(21)-C(26)-H(26A)	109.5
C(21)-C(26)-H(26B)	109.5
H(26A)-C(26)-H(26B)	109.5
C(21)-C(26)-H(26C)	109.5
H(26A)-C(26)-H(26C)	109.5
H(26B)-C(26)-H(26C)	109.5
C(28)-C(27)-C(23)	123.7(10)
C(28)-C(27)-H(27)	118.1
C(23)-C(27)-H(27)	118.1
C(27)-C(28)-C(29)	125.6(11)
C(27)-C(28)-H(28)	117.2
C(29)-C(28)-H(28)	117.2
C(30)-C(29)-C(28)	126.8(9)
C(30)-C(29)-C(34)	116.7(10)
C(28)-C(29)-C(34)	116.4(10)
C(31)-C(30)-C(29)	124.6(10)
C(31)-C(30)-H(30)	117.7
C(29)-C(30)-H(30)	117.7
C(30)-C(31)-C(32)	119.9(11)
C(30)-C(31)-H(31)	120
C(32)-C(31)-H(31)	120
N(4)-C(32)-C(33)	123.6(10)
N(4)-C(32)-C(31)	119.7(11)
C(33)-C(32)-C(31)	116.7(10)
C(32)-C(33)-C(34)	121.4(10)

Continued on next page

Table 2.5 – *Continued from previous page*

C(32)-C(33)-H(33)	119.3
C(34)-C(33)-H(33)	119.3
C(33)-C(34)-C(29)	120.6(11)
C(33)-C(34)-H(34)	119.7
C(29)-C(34)-H(34)	119.7
N(4)-C(35)-C(36)	108.5(10)
N(4)-C(35)-H(35A)	110
C(36)-C(35)-H(35A)	110
N(4)-C(35)-H(35B)	110
C(36)-C(35)-H(35B)	110
H(35A)-C(35)-H(35B)	108.4
O(2)-C(36)-C(35)	108.2(11)
O(2)-C(36)-H(36A)	110.1
C(35)-C(36)-H(36A)	110.1
O(2)-C(36)-H(36B)	110.1
C(35)-C(36)-H(36B)	110.1
H(36A)-C(36)-H(36B)	108.4
Si(1)-C(37)-H(37A)	109.5
Si(1)-C(37)-H(37B)	109.5
H(37A)-C(37)-H(37B)	109.5
Si(1)-C(37)-H(37C)	109.5
H(37A)-C(37)-H(37C)	109.5
H(37B)-C(37)-H(37C)	109.5
Si(1)-C(38)-H(38A)	109.5
Si(1)-C(38)-H(38B)	109.5
H(38A)-C(38)-H(38B)	109.5
Si(1)-C(38)-H(38C)	109.5

Continued on next page

Table 2.5 – *Continued from previous page*

H(38A)-C(38)-H(38C)	109.5
H(38B)-C(38)-H(38C)	109.5
C(42)-C(39)-C(41)	111.5(14)
C(42)-C(39)-C(40)	107.6(15)
C(41)-C(39)-C(40)	109.7(12)
C(42)-C(39)-Si(1)	111.3(10)
C(41)-C(39)-Si(1)	109.2(11)
C(40)-C(39)-Si(1)	107.3(11)
C(39)-C(40)-H(40A)	109.5
C(39)-C(40)-H(40B)	109.5
H(40A)-C(40)-H(40B)	109.5
C(39)-C(40)-H(40C)	109.5
H(40A)-C(40)-H(40C)	109.5
H(40B)-C(40)-H(40C)	109.5
C(39)-C(41)-H(41A)	109.5
C(39)-C(41)-H(41B)	109.5
H(41A)-C(41)-H(41B)	109.5
C(39)-C(41)-H(41C)	109.5
H(41A)-C(41)-H(41C)	109.5
H(41B)-C(41)-H(41C)	109.5
C(39)-C(42)-H(42A)	109.5
C(39)-C(42)-H(42B)	109.5
H(42A)-C(42)-H(42B)	109.5
C(39)-C(42)-H(42C)	109.5
H(42A)-C(42)-H(42C)	109.5
H(42B)-C(42)-H(42C)	109.5
N(4)-C(43)-C(44)	113.8(10)

Continued on next page

Table 2.5 – *Continued from previous page*

N(4)-C(43)-H(43A)	108.8
C(44)-C(43)-H(43A)	108.8
N(4)-C(43)-H(43B)	108.8
C(44)-C(43)-H(43B)	108.8
H(43A)-C(43)-H(43B)	107.7
O(3)-C(44)-C(43)	111.6(11)
O(3)-C(44)-H(44A)	109.3
C(43)-C(44)-H(44A)	109.3
O(3)-C(44)-H(44B)	109.3
C(43)-C(44)-H(44B)	109.3
H(44A)-C(44)-H(44B)	108
Si(2)-C(45)-H(45A)	109.5
Si(2)-C(45)-H(45B)	109.5
H(45A)-C(45)-H(45B)	109.5
Si(2)-C(45)-H(45C)	109.5
H(45A)-C(45)-H(45C)	109.5
H(45B)-C(45)-H(45C)	109.5
Si(2)-C(46)-H(46A)	109.5
Si(2)-C(46)-H(46B)	109.5
H(46A)-C(46)-H(46B)	109.5
Si(2)-C(46)-H(46C)	109.5
H(46A)-C(46)-H(46C)	109.5
H(46B)-C(46)-H(46C)	109.5
C(49)-C(47)-C(50)	103(2)
C(49)-C(47)-C(48)	111(2)
C(50)-C(47)-C(48)	109.1(19)
C(49)-C(47)-Si(2)	112.0(19)

Continued on next page

Table 2.5 – *Continued from previous page*

C(50)-C(47)-Si(2)	110.3(15)
C(48)-C(47)-Si(2)	110.6(12)
C(47)-C(48)-H(48A)	109.5
C(47)-C(48)-H(48B)	109.5
H(48A)-C(48)-H(48B)	109.5
C(47)-C(48)-H(48C)	109.5
H(48A)-C(48)-H(48C)	109.5
H(48B)-C(48)-H(48C)	109.5
C(47)-C(49)-H(49A)	109.3
C(47)-C(49)-H(49B)	109.5
H(49A)-C(49)-H(49B)	109.5
C(47)-C(49)-H(49C)	109.7
H(49A)-C(49)-H(49C)	109.5
H(49B)-C(49)-H(49C)	109.5
C(47)-C(50)-H(50A)	109.5
C(47)-C(50)-H(50B)	109.5
H(50A)-C(50)-H(50B)	109.5
C(47)-C(50)-H(50C)	109.4
H(50A)-C(50)-H(50C)	109.5
H(50B)-C(50)-H(50C)	109.5
C(32)-N(4)-C(43)	124.4(10)
C(32)-N(4)-C(35)	120.6(11)
C(43)-N(4)-C(35)	115.0(9)
C(1)-O(1)-C(4)	111.6(8)
C(36)-O(2)-Si(1)	132.2(8)
C(44)-O(3)-Si(2)	121.9(9)
O(2)-Si(1)-C(38)	109.1(6)

Continued on next page

Table 2.5 – *Continued from previous page*

O(2)-Si(1)-C(37)	104.0(6)
C(38)-Si(1)-C(37)	109.6(7)
O(2)-Si(1)-C(39)	112.3(6)
C(38)-Si(1)-C(39)	109.8(7)
C(37)-Si(1)-C(39)	111.9(7)
O(3)-Si(2)-C(47)	113.1(6)
O(3)-Si(2)-C(46)	103.6(7)
C(47)-Si(2)-C(46)	112.1(9)
O(3)-Si(2)-C(45)	110.2(7)
C(47)-Si(2)-C(45)	110.7(10)
C(46)-Si(2)-C(45)	106.8(9)

Table 2.6: Dipole moments, polarizabilities, and hyperpolarizabilities calculated using LC-BLYP/6-31+G* *in vacuo*; given according to the perturbation convention. Frequency-dependent properties are computed at 1310-nm.

Structures	μ_z (D)	$\alpha_{zzz}(-\omega;\omega)$ $\times 10^{-24}$ esu	$\beta_{zzz}(0)$ $\times 10^{-30}$ esu	$\beta_{zzz}(-\omega;\omega,0)$ $\times 10^{-30}$ esu
JRD1	21.4	308	483	680
YLD124	22	171	460	641
AJY1	22.6	248	444	623
JRD2	17.6	151	87.9	108
KRD1	20	190	341	463
JRD5	20.3	304	476	664

2.11 Theory

2.11.1 Donor Study

All calculations were performed with the Gaussian-09 Rev D.01 electronic structure package (Frisch 2013). [91] The molecular geometries were optimized in vacuum at the B3LYP/6-31+G* level of theory using an "ultrafine" integration grid and tightened convergence settings (i.e., "Opt=Tight"), which choose the RMS force on all atoms to converge at a threshold of 1×10^{-5} au or less. All calculations were carried out according to default SCF convergence criteria, requiring density matrix convergence at least 10^{-8} au. Dipole moments and static and frequency-dependent (hyper)polarizabilities were computed with a long-range corrected (LC) functional, LC-BLYP (Iikura 2001). [92] Static hyperpolarizability, $\beta_{zzz}(0)$, and Pockels hyperpolarizability consistent with measurements of poling efficiency, $\beta_{zzz}(-\omega;\omega,0)$, at 1310-nm were computed via analytic differentiation by the coupled-perturbed Kohn-Sham (CPKS) method (Kamiya 2005). [93] Changes in computed electronic and optical properties as a result of changing dielectric environment were also studied using the polarizable continuum model (PCM). See Tables 2.6-2.8. Excitation energies were computed with B3LYP with 6-31+G* basis set using the linear response time-dependent DFT formalism in solvent

Table 2.7: Dipole moments, polarizabilities, hyperpolarizabilities, and wavelength of maximum absorption (λ_{max}) calculated using LC-BLYP/6-31+G* in acetonitrile; given according to the perturbation convention. Frequency-dependent properties are computed at 1310-nm.

Structures	μ_z (D)	$\alpha_{zzz}(-\omega;\omega)$ $\times 10^{-24}$ esu	$\beta_{zzz}(0)$ $\times 10^{-30}$ esu	$\beta_{zzz}(-\omega;\omega,0)$ $\times 10^{-30}$ esu	λ_{max} (nm) λ_{max} (nm)
JRD1	26.1	398	1245	1567	731.01
YLD124	27.1	210	1231	1536	729.74
AJY1	28.3	342	1334	1659	738.14

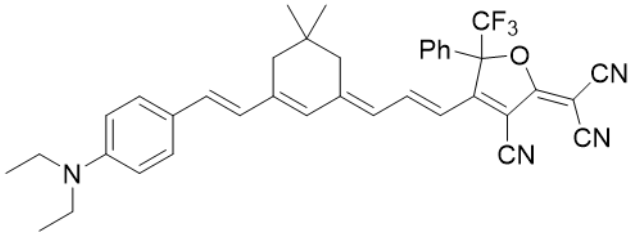

(structure of AJY1)

media (chloroform and acetonitrile) with PCM.

In the HOMO-LUMO structures, you can see that the TBDPS and TBDMS groups do not participate greatly in the electronic structures. The HOMO-LUMO structures are similar for the series, based both on MO visualization and energy levels. Figures 2.37-2.39 show the HOMO and LUMO structures according to B3LYP/6-31+G* and wB97xD/6-31+G*. The HOMO structures are qualitatively similar across the DFT methods; however, LUMO for wB97xD is much less localized on the donor phenyl ring than shown in B3LYP. Nevertheless, the LUMO structures are similar for AJY1, JRD1, and YLD124 within a given DFT method (wB97xD or B3LYP).

The frontier molecular orbitals of JRD1 and JRD5 are shown in Figure 2.40, according to wB97D/6-31+G*//B3LYP/6-31+G* in chloroform (PCM). The highest occupied molecular orbitals (HOMO) of the two species are generally similar and are delocalized over the length of the π-conjugated bridge, however the visualization shows that the carbazole in JRD5 offers a small electron-donating contribution. The lowest unoccupied molecular orbitals (LUMO) are similar for both structures and have only approximately 0.04 eV energy differ-

Table 2.8: Dipole moments, polarizabilities, hyperpolarizabilities, and wavelength of maximum absorption (λ_{max}) calculated using LC-BLYP/6-31+G* in acetonitrile; given according to the perturbation convention. Frequency-dependent properties are computed at 1310-nm. *Note that $\beta_{zzz}(-\omega;\omega,0) < \beta_{zzz}(0)$; this commonly occurs with highly polar solvents.

Structures	μ_z (D)	$\alpha_{zzz}(-\omega;\omega)$ $\times 10^{-24}$ esu	$\beta_{zzz}(0)$ $\times 10^{-30}$ esu	$\beta_{zzz}(-\omega;\omega,0)$ $\times 10^{-30}$ esu	λ_{max} (nm) λ_{max} (nm)
JRD1	27.7	398.7	1768	1695*	729.09
YLD124	29	209	1782	1695*	729.71
AJY1	30.3	343	1980	1840*	737.99

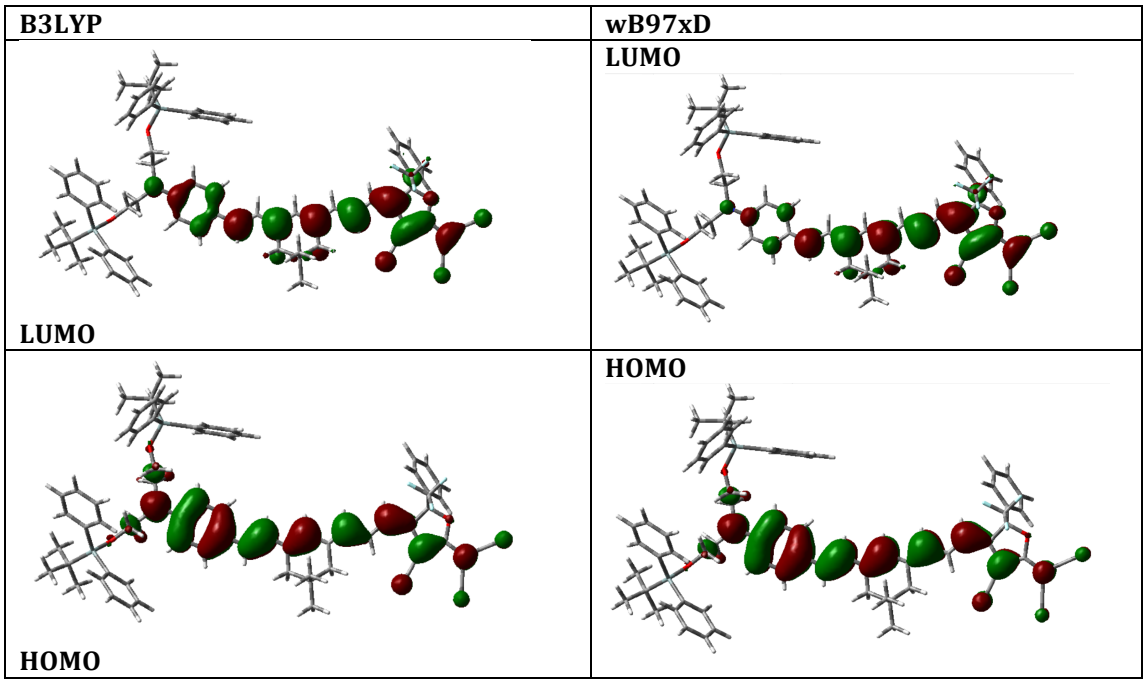

Figure 2.37: JRD1 Molecular Orbital structures DFT/6-31+G*//B3LYP/6-31+G* in Chloroform (PCM).

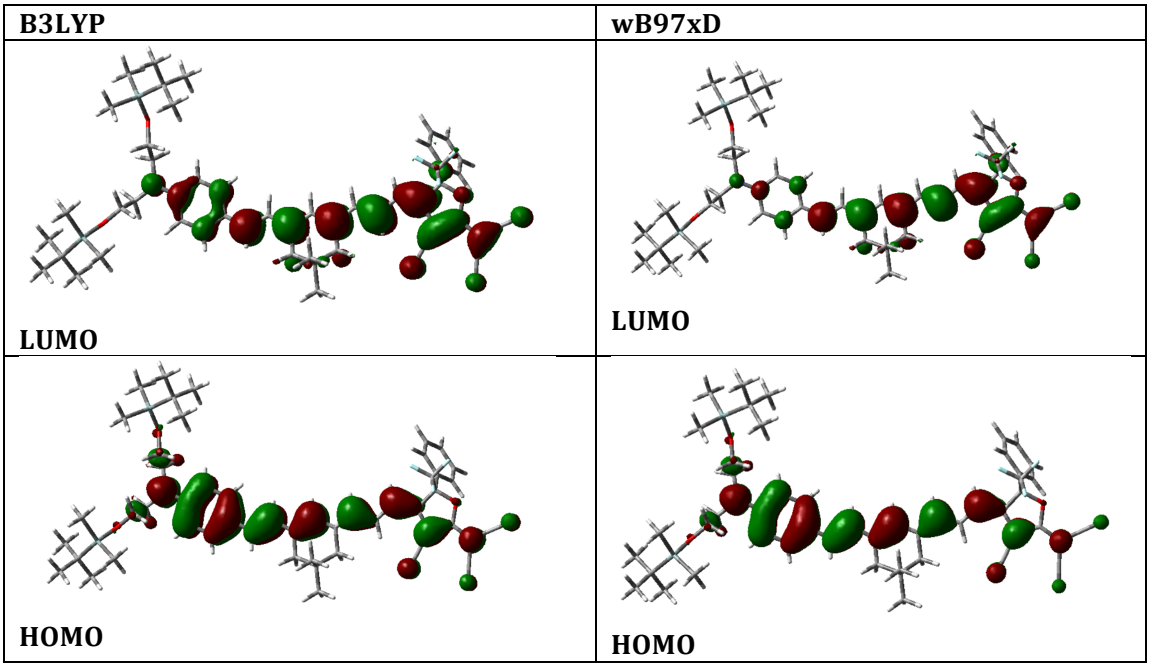

Figure 2.38: YLD124 Molecular Orbital structures DFT/6-31+G*//B3LYP/6-31+G* in Chloroform (PCM).

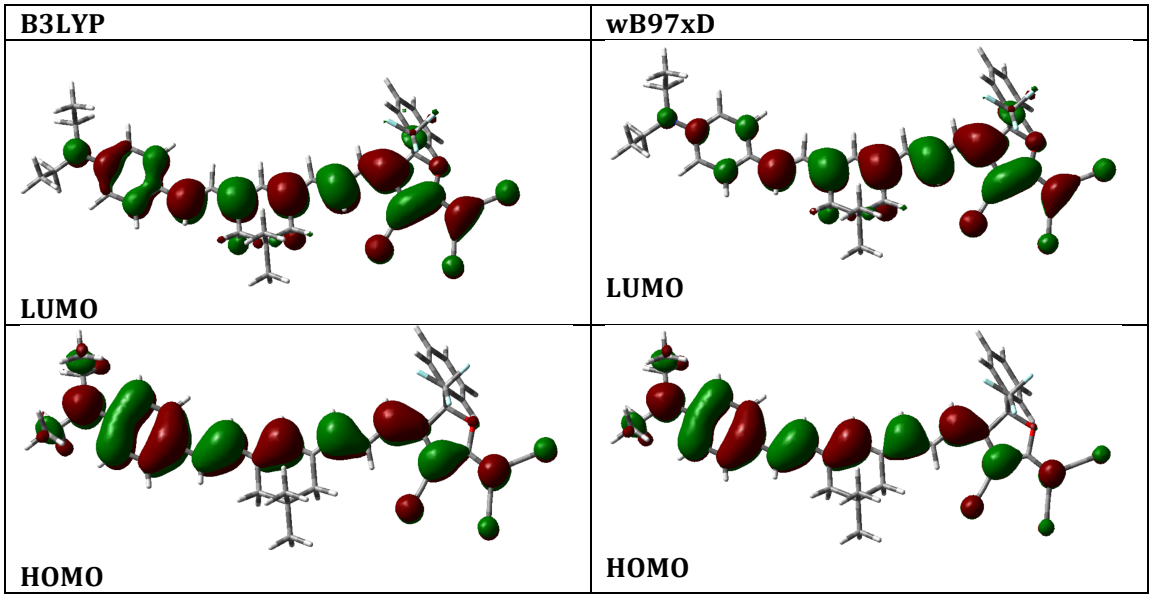

Figure 2.39: AJY1 Molecular Orbital structures DFT/6-31+G*//B3LYP/6-31+G* in Chloroform (PCM).

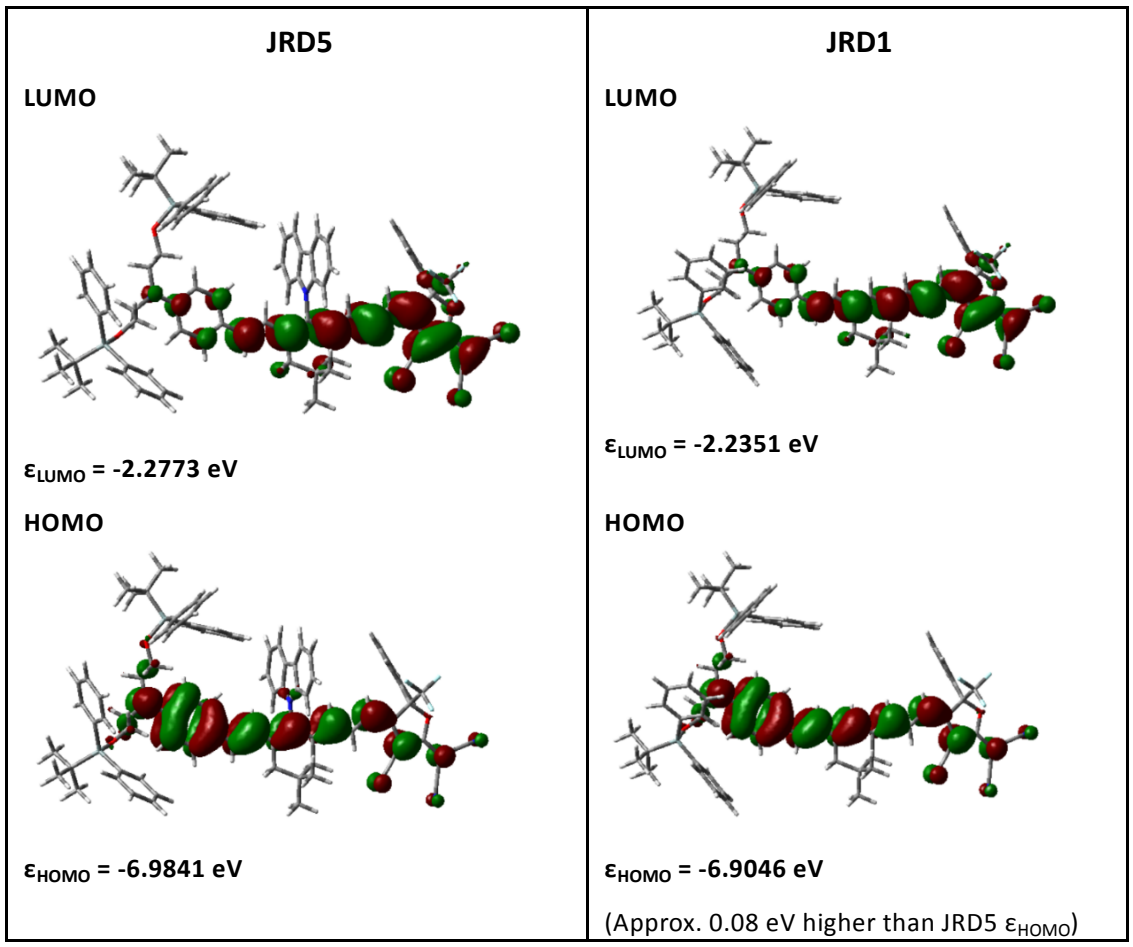

Figure 2.40: Side-by-side comparison of JRD5 and JRD1 molecular orbital structures according to wB97xD with 6-31+G* basis set and B3LYP/6-31+G* optimized geometry in Chloroform (PCM).

ence between JRD1 and JRD5. It follows that the intramolecular charge transfer transition energies ($\Delta E_{HOMO-LUMO}$) from HOMO-LUMO are similar between JRD1 and JRD5 with approximately 0.04 eV difference. It is important to note that the HOMO-LUMO energy difference, $\Delta E_{HOMO-LUMO}$, is not equal to the peak vertical excitation energy (i.e., λ_{max}) which involves a mixing of contributions from various excited states.

The frontier molecular orbitals of JRD1 and JRD5 according to B3LYP/6-31+G*/ /B3LYP/6-31+G* in chloroform (PCM) are shown in Figure 2.41. Similar to the long-range corrected method results (wB97xD; Figure 2.40), the HOMO visualization shows that the carbazole in JRD5 offers a small electron-donating contribution. The HOMO and LUMO energy values of JRD1 are shifted approx. 0.07 eV higher than those of JRD5. Consequently, the intramolecular charge transfer transition energies ($\Delta E_{HOMO-LUMO}$) from HOMO-LUMO are practically identical.

The frontier molecular orbitals of KRD1 according to different DFT methods: B3LYP and wB97xD, both with 6-31+G* basis set and B3LYP optimized geometry in chloroform (PCM) are shown in Figure 2.42. As expected with the inclusion of long-range (LR) Hartree Fock (HF) exchange in wB97xD, the predicted intramolecular charge transfer transition energy ($\Delta E_{HOMO-LUMO}$) from HOMO-LUMO is significantly larger (blue-shifted) in comparison to B3LYP which has no LR HF exchange correction. Within a given DFT method, the energy results for KRD1 are similar to JRD1 and JRD5. The frontier molecular orbitals of JRD2 according to different DFT methods: B3LYP and wB97xD, both with 6-31+G* basis set and B3LYP optimized geometry in chloroform (PCM) are shown in Figure 2.43. The smaller bridge structure results in an overall larger energy CT transition (blue shift) than predicted for JRD1, JRD5, or KRD1.

2.12 Device Fabrication

ITO/glass substrates were scrubbed with a cotton swab and multi-purpose detergent. Then slides were rinsed with deionized water, and fixed vertically on a polyethylene block where they were first immersed in acetone and sonicated for 5-10 minutes followed by immersion in isopropanol and another sonication for 5-10 minutes. Solutions of 9-12% w/w EO material in TCE were filtered through a 0.2 μm PTFE filter and spin cast on ITO/Glass substrates

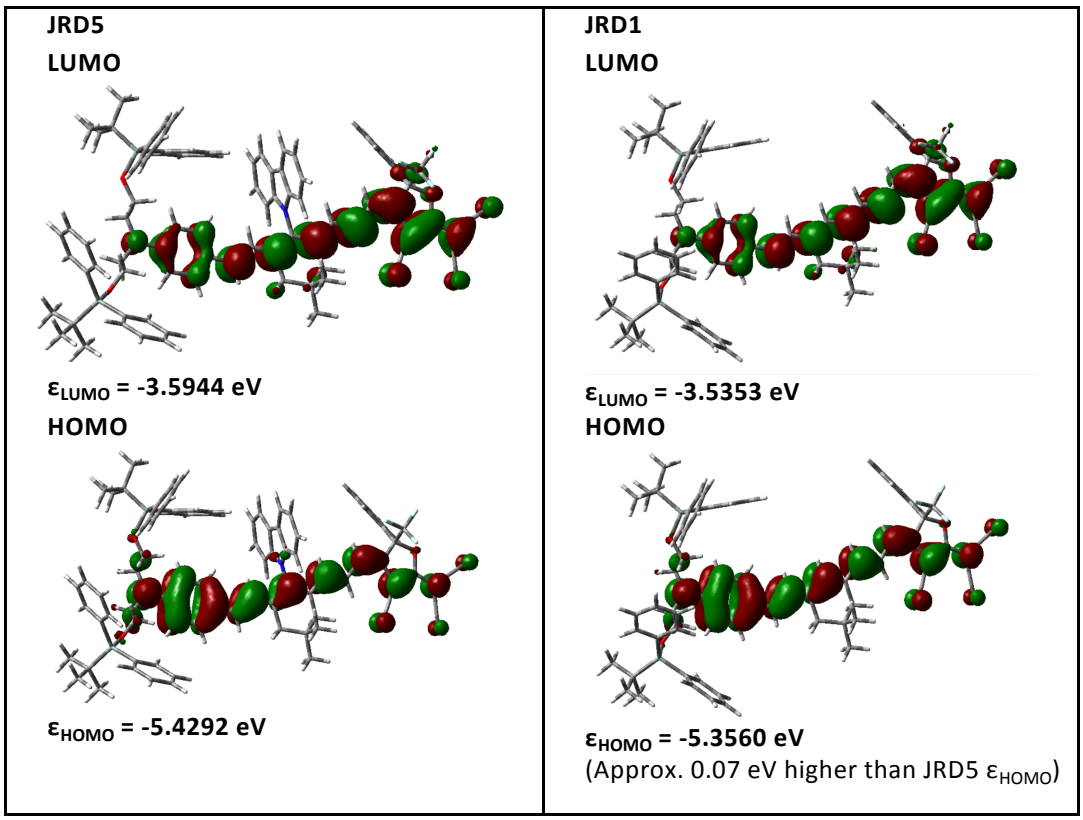

Figure 2.41: Side-by-side comparison of JRD5 and JRD1 molecular orbital structures according to B3LYP with 6-31+G* basis set and B3LYP/6-31+G* optimized geometry in Chloroform (PCM).

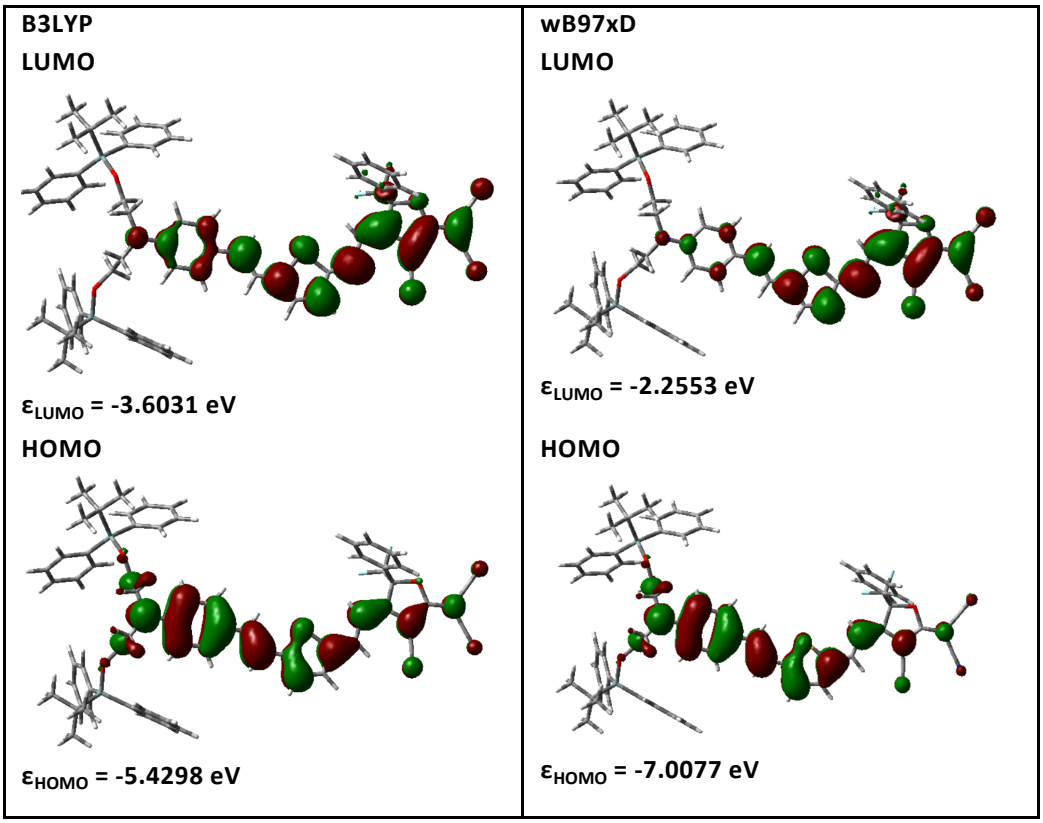

Figure 2.42: Side-by-side comparison of B3LYP and wB97xD results for molecule KRD1: Molecular Orbital structures.

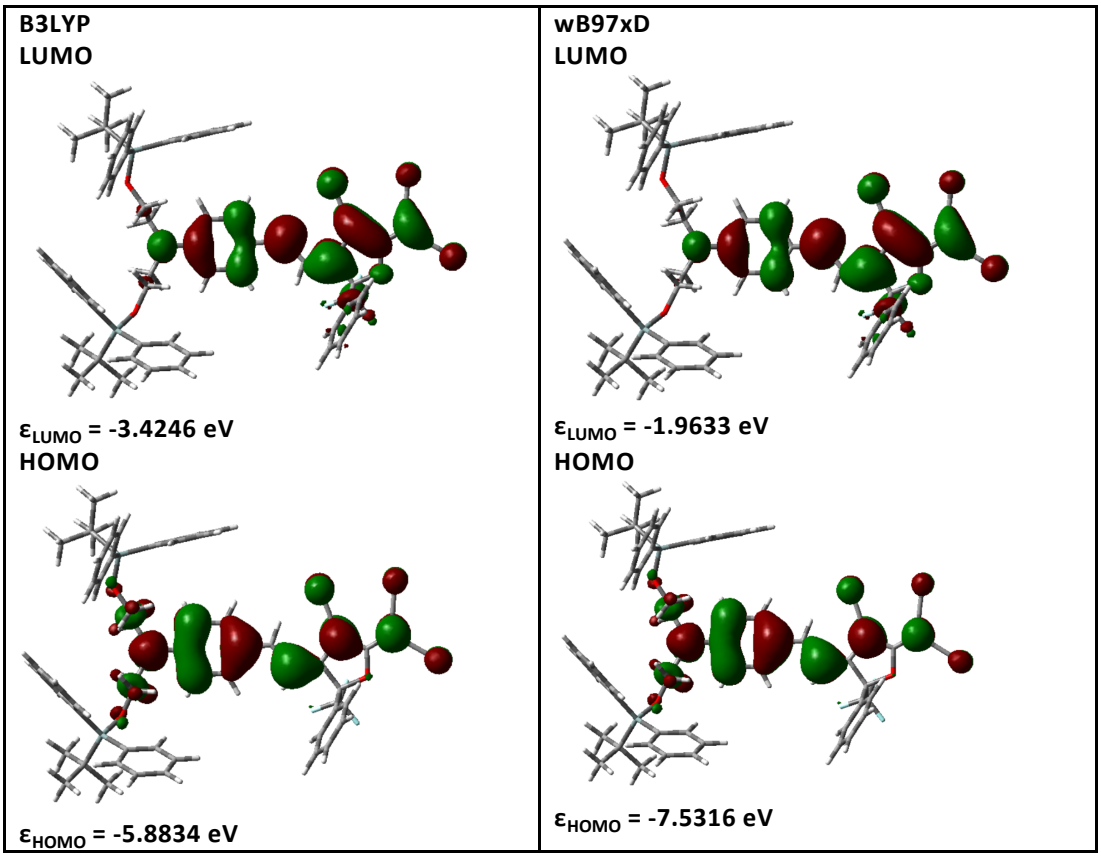

Figure 2.43: Side-by-side comparison of B3LYP and wB97xD results for molecule JRD2: Molecular Orbital structures

to form neat thin films. EO films were spin cast in three stages, 500 rpm for 5 seconds, 850 rpm for 30 seconds, followed immediately by 2000 rpm for 30 seconds. The films were then dried on a hot plate at 65 °C for half an hour, and then further cured in a vacuum oven at 65 °C overnight. The thickness of the EO film was then measured to be around 1-2 μm via optical profilometry. Gold electrodes (∼60 nm thick) were deposited on top of the films by sputter coating.

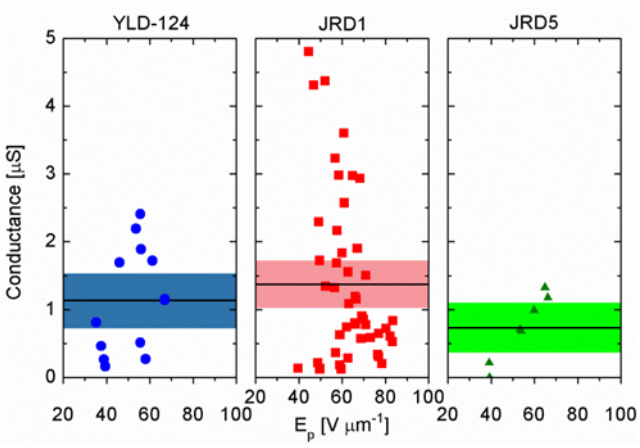

[!h]

Figure 2.44: The average conductance (G) during the poling process of JRD1-based devices (red square, G = 1.37 ± 0.35 μS), YLD-124-based devices (blue dot, G = 1.13 ± 0.40 μS), and JRD5-based devices (green triangle, G = 0.73 ± 0.36 μS). Red, green, and blue bands represent the 95% confidence intervals of the mean conductance.

2.13 Results and Discussion

2.13.1 Device conductance

High device conductance caused by chromophore conductivity at elevated temperature during poling limits the EO activity and needs to be controlled. There have been previous efforts to control this by introducing barrier layers, [2, 94] but certain barrier layers (e.g. solvent cast) are not easy to apply to device structures with vertical electrode walls, such as silicon slot waveguides used in SOH modulators. We found in our research that molecular modification might help to reduce poling-induced conductance in high ρ_N chromophores. The conductance of YLD-124, JRD1 and JRD5 devices were calculated from the measured current and voltage as a function of the average poling field during the poling process (Figure 2.44). JRD5 devices showed relative low conductance, while JRD1 and YLD-124 devices had similarly high conductance behavior. This figure indicates that the conductivity of monolithic materials can be affected by tuning of the bulk electronic mobility through bridge modification. This could be a noteworthy area for future study to solve the high conductivity problem of high number-density materials, in addition to the current barrier layer

solution.

2.14 Additional Information for Poling Results

Table 2.9: Average electric field during poling for the max r_{33}.

EO material	Barrier layer	Electric field Ep $/(V\mu m^{-1})$	Max r_{33} $/(pmV^{-1})$	r_{33}/E_p $/(nm/V)^2$
YLD-124	With BCB	75	242	3.2
	No barrier	57	118	2.1
JRD1	With BCB	85	556	6.5
	No barrier	77	343	4.5
JRD5	With BCB	75	214	2.9
	No barrier	65	188	2.9
JRD2	No barrier	54	22	0.4
KRD1	No barrier	110	155	1.4

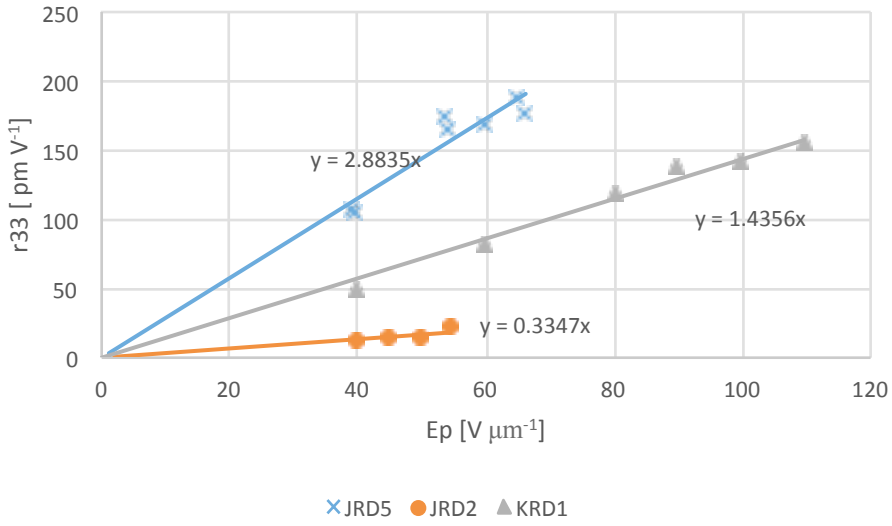

[!h]

Figure 2.45: Poling curves for JRD5, JRD2 and KRD1.

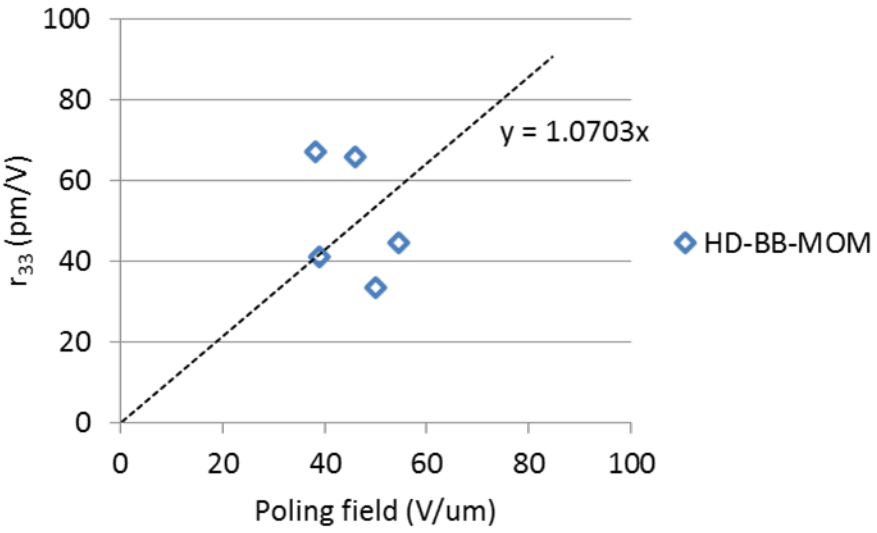

[!h]

Figure 2.46: poling field plot for H vs. poling field plot for HD-BB-MOM.

For more detailed information about statistical analysis, analysis of average electric field strength during poling, and the calculation of the device conductance, please see reference [2] and its supporting information.

2.15 Acknowledgements

This material is based upon work supported by the National Science Foundation under Grant Number (DMR-1303080, DMR-0120967). Any opinions, findings, and conclusions or recommendations expressed in this material are those of the author(s) and do not necessarily reflect the views of the National Science Foundation. The authors acknowledge partial financial support from the Air Force Office of Scientific Research (FA9550-10-1-0558, FA9550-15-1-0319). The authors also acknowledge the AMSEC Center at Western Washington University for TGA and DSC measurements. The authors would like to thank Roberto Garcia for his pioneering work in the crystallization of YLD-124. Jin W. also thanks the State-Sponsored Scholarship for Graduate Students from China Scholarship Council. Part of this work was conducted at the University of Washington Nanotechnology User Facility, a member of the NSF National Nanotechnology Infrastructure Network.

Chapter 3

BENZOCYCLOBUTENE BARRIER LAYER FOR SUPPRESSING CONDUCTANCE IN NONLINEAR OPTICAL DEVICES DURING ELECTRIC FIELD POLING [2]

3.1 Abstract

We measured the electro-optic (EO) coefficients (r_{33}) of thin-film devices made from several monolithic, high number density organic EO chromophores with and without additional charge barrier layers. We found that a cross-linkable benzocyclobutene layer was very effective in suppressing unwanted, leakage current, keeping the effective poling voltage nearly identical to the applied voltage. This barrier layer proved to be superior to a titanium dioxide (TiO_2) barrier layer. The suppression of the leakage current in combination with a new chromophore enabled the construction of EO devices that had r_{33} values - 400−500 $pm\ V^{-1}$ with poling fields 85 $V\ \mu m^{-1}$. VC 2014 AIP Publishing LLC. [http://dx.doi.org/10.1063/1.4884829]

3.2 Introduction

Organic nonlinear electro-optic (EO) materials have demonstrated substantial promise as components in a variety of photonics applications, including EO modulation and terahertz generation and detection. [34, 95–98] For 2nd order organic EO materials, three parameters ultimately define material performance: molecular hyperpolarizability (β) of the EO chromophore, number density (ρ_N) of active molecules that interact with the incident optical field, and acentric order ($\langle cos^3\theta \rangle$), which is generally generated by an electric field to induce chromophore order, a process known as "poling." [14, 19, 38] Optimization of these three parameters, as they relate to r_{33} according to the proportionality $r_{33} \propto \rho_N \beta \langle \cos^3 \theta \rangle$, is required to improve EO performance. [24]

Previous studies of guest-host EO materials have established that EO coefficients (r_{33}) approaching 200 $pm\ V^{-1}$ can be routinely achieved. [99, 100] High number density materials,

including monolithic films and binary-chromophore molecular glasses have demonstrated increased EO activity with r_{33} values approaching 400 $pm\ V^{-1}$. [49, 52, 101] One challenge in the fabrication of devices from these materials is the significant leakage current that occurs during poling. The increase in conductivity of the electro-optic material at the glass transition temperature during the poling process either reduces the magnitude of the electric field that can be sustained during poling or increases leakage current, which in turn limits the amount of acentric order that is induced. To achieve greater acentric order in these materials, the extent of leakage current or the conductance of the device must be reduced.

Reducing device conductance requires understanding the nature of the interface-limited current and judicious modification of the interface between the electrode and the EO material to prevent charge injection. [15,102] Ideally, the device architecture should include a "barrier" layer having significantly mismatched highest-occupied molecular orbital (HOMO)/lowest-unoccupied molecular orbital (LUMO) energies properly tuned relative to the electrode and the EO material. The introduction of an appropriate charge injection barrier layer enables larger poling fields across EO materials resulting in larger r_{33} values.

Previous barrier layer materials include metal-oxides, organic monolayers, conductive polymer blends (e.g., poly (ethylene dioxythiophene)/poly (styrenesulphonic acid) in poly (vinylalcohol)), and non-conductive polymers (e.g., poly(4-vinylphenol), the ferroelectric polymer poly(vinyli- dene fluoridetrifluoroethylene), and cyclic olefin copolymer TOPAS®). Among these, TiO_2 has emerged as one of the most successful barrier layer materials to address high conductance problems. [15, 94, 102–106] However, even with a TiO_2 layer, current leakage remains one to two orders of magnitude larger than the baseline current prior to poling. [94] This implies that the poling field is reduced during the poling process in spite of the TiO_2 layer, leading to less than optimal r_{33} values. The large conductivity associated with high number density organic EO materials ($> 3 \times 10^{20}\ molecules/cm^3$), [107] even with state-of-the-art TiO_2 as a charge-blocking layer, motivates further research into alternative barrier layer materials.

Herein, we demonstrate that the electric field applied to monolithic EO materials can be increased by incorporating a barrier layer of benzocyclobutene (BCB). Thermally crosslinked BCB was selected for this study because it has a large HOMO/LUMO gap that generates

a charge injection barrier. Upon crosslinking, BCB becomes quite mechanically stable and insoluble, will not wash away, crack, or swell significantly, an advantage over non-crosslinked organic barriers. Also, BCB has other excellent properties, including high optical transparency, easy solution processing, and long-term stability when exposed to air before and after cross-linking, which are advantages over TiO_2.

3.3 Experimental

To measure EO coefficients, indium tin oxide (ITO)/EO material/gold or ITO/barrier layer/EO material/gold devices were fabricated on glass substrates (figure 3.1). ITO (45 nm thick, resistivity $\leq 100\ \Omega/sq.$) was purchased coated on glass from Thin Film Devices. The TiO_2 barrier layer was spin cast and annealed following the standard sol-gel derived method previously reported resulting in $40-70$ nm films. [108] The BCB barrier layer was fabricated from commercially available BCB polymer (Cyclotene 3022-46, from Dow Corp.). The optimum thickness of the BCB layer ranged from 60 to 100 nm (see Appendix 1). When BCB was used as a barrier layer, a $\sim$20 nm poly(methyl methacrylate) (PMMA) film was spun cast as an adhesion layer; control studies showed that the PMMA layer had no additional charge barrier benefits beyond BCB alone (see Appendix 1). EO chromophore was spun cast from 1,1,2-trichloroethane solvent, resulting in 1-2 μm thick monolithic films. A 60 nm thick gold layer was sputter coated as the top electrode.

The effect of the BCB layer was examined for three monolithic chromophores: JRD1, YLD-124, and JSLD5 (figure 3.3). These structures were developed to illustrate the effect and importance of both increasing number density and tuning intermolecular interactions by variation in molecular size and structure on a shared EO motif. These molecules display similar optical properties (e.g., molar absorptivity, wavelength of maximum absorption, and presumably first-hyperpolarizabilities); however, as shown later, small structural differences give rise to large and unexpected differences in EO performance.

During electric field poling, the current and voltage across the device were measured along with an in situ r_{33} analysis at 1310 nm by the Teng-Man ellipsometric method. [13,21] Samples were poled under DC electric fields ranging from 40 to 105 $V\ \mu m^{-1}$ while being heated at a rate of 10 °C/min. Poling started near the material glass transition temperature

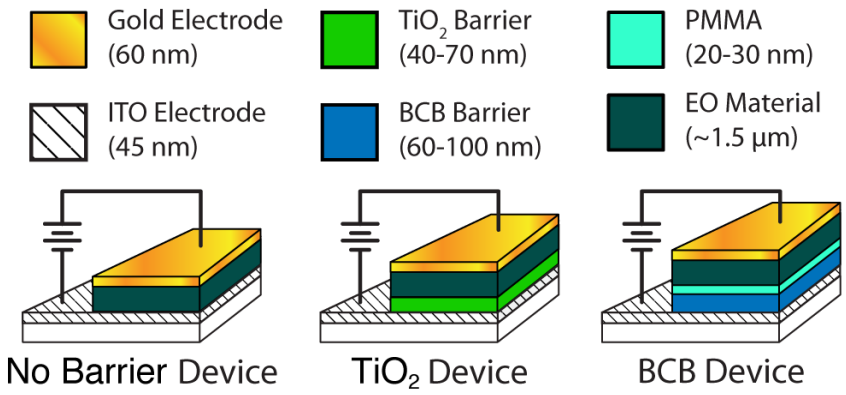

Figure 3.1: Addition of barrier layers to the standard poling prototype from left to right: A device with no barrier layer, a device with a titanium dioxide (TiO_2) barrier layer, and a device with a benzocyclobutene (BCB) barrier layer. Polymethyl methacrylate (PMMA) was used as an adhesion layer in the devices containing a BCB barrier layer to improve film quality. ITO and gold (Au) were the bottom and top electrodes, respectively.

(T_g, table 3.1) and continued at the T_g for 1−2 min. Then, the sample was cooled while maintaining the poling field until the sample was well below the T_g.

3.4 Results and Discussion

The addition of a BCB layer to the devices significantly reduced device conductance throughout the poling process. The conductance of two representative JRD1-based devices (with and without BCB layer) at identical applied poling fields of 95 $V\ \mu m^{-1}$ is shown in figure 3.2(a).

The conductance was estimated from the voltage and current of a simple two-probe measurement. Conductance of the JRD1-based device in the absence of a BCB layer was observed to sharply increase as the temperature approached the T_g (red curve), from 0.12 μS before poling to a maximum of 4.62 μS during poling. However, in the presence of the BCB layer (blue curve), conductance increased only slightly from 0.106 μS before poling to a maximum of 0.142 μS during poling. The conductance of a BCB-containing device at the EO poling temperature is consistently 0.1 μS. Therefore, the reduced device conductance, due to the BCB layer, is consistent with a reduction in current due to dramatically reduced

Table 3.1: Summary of the number density, T_g and poling results of JRD1, YLD-124, and JSLD5. ρ_N calculations assume a material density of 1 gcm^{-1}. The ratio, r_{33}/r_{33}^0, represents the maximum r_{33} measured with a barrier layer over that measured without a barrier layer.

	ρ_N	T_g		$r_{33}/\ pmV^{-1}$		$\overline{r_{33}/E_p}$
EO Material	$molx/cm^{-3}$	/°C	Barrier	(best)	r_{33}/r_{33}^0	$/(nm/V)^2$
JRD1	5.33×10^{20}	93	none	343±55	...	3.1±0.1
			BCB	556±90	1.6 ±0.04	3.4±0.1
			TiO_2	277±54	0.08 ±0.02	2.6±0.2
YLD-124	6.83×10^{20}	83	none	118±29	...	1.4±0.1
			BCB	242±37	2.0±0.6	1.9±0.2
JSLD5	3.07×10^{20}	73	none	89±11	...	0.98±0.07
			BCB	177±18	2.0±0.3	1.8±0.1

charge injection. [109] The conductivity calculation of JRD1 and BCB is shown in Appendix 1.

Because of the large band gap of the general class of non-conjugated polymers, [110, 111] BCB performs well as a charge barrier. The best results were obtained with ITO as the negative electrode and gold as the positive electrode (work functions -4.8 eV and -5.2 eV, respectively); this was true for both BCB and TiO_2 barriers. According to theoretical calculations on BCB model compounds, HOMO and LUMO levels for BCB were -5.7 eV and -0.9 eV, respectively (B3LYP DFT method, 631 G* basis set; see Appendix 1). Therefore, there is a 3.9 eV barrier to electron injection from the negative ITO electrode to the BCB LUMO, compared to a 0.9 eV barrier to charge injection directly to the JRD1 LUMO without a barrier layer (JRD1 HOMO = -5.0 eV, LUMO = -3.9 eV, determined by cyclic voltammetry). BCB also provides a larger barrier than the ~ 3 eV barrier to charge injection provided by TiO_2. [94]

The average conductance during the poling process, calculated from the measured current and voltage as a function of the average poling field during the poling process is shown in figure 3.2(b). The mean of all conductance measurements on JRD1-based devices (with no

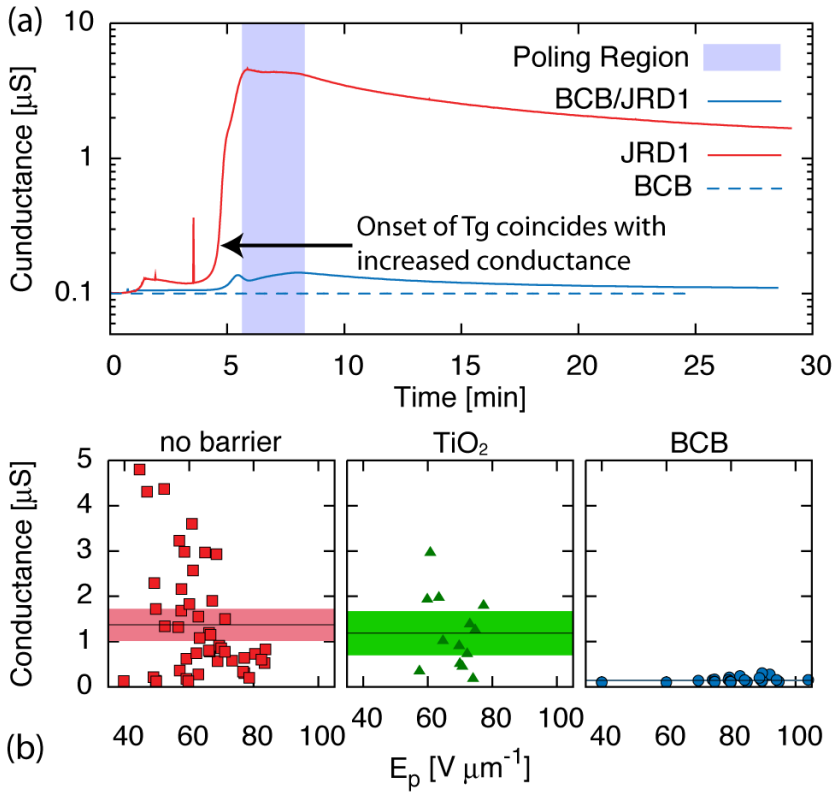

Figure 3.2: (a) Conductance (G) of a JRD1-based device as a function of time during poling at identical applied poling fields of 95 $V\ \mu m^{-1}$ with (blue) and without (red) a BCB barrier layer. The shaded region represents the duration of the poling process (the period of time that the sample is at T_g). (b) The average conductance during the poling process of JRD1-based devices with no barrier layer (red squares, $G = 1.37 \pm 0.18\ \mu S$), with a TiO_2 layer (green triangles, $G = 1.18 \pm 0.22\ \mu S$), and with a BCB layer (blue dots, $G = 0.142 \pm 0.008\ \mu S$). Red, green, and blue bands represent the 95% confidence intervals around the mean conductance.

barrier layer, with a TiO_2 layer, and with a BCB layer) were plotted at the 95% confidence level as shaded regions. The figure illustrates that the presence of the BCB layer (blue dots) decreased the conductance by one order of magnitude relative to the other two devices. The TiO_2 layer did not produce a statistically significant change in conductance relative to the device with no barrier layer.

Our results indicate that the actual poling field across the EO layer during the poling

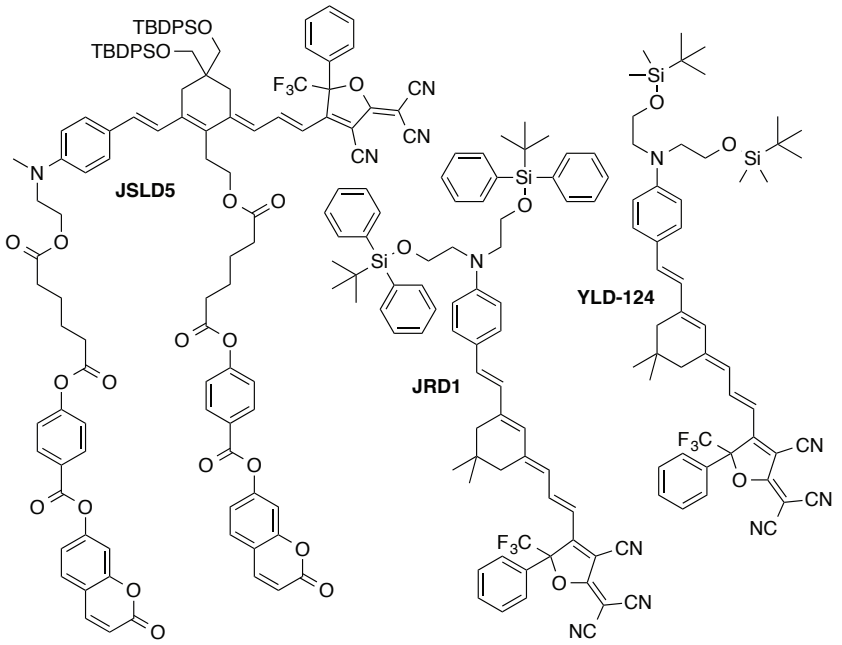

Figure 3.3: Three EO chromophores utilized in this study.

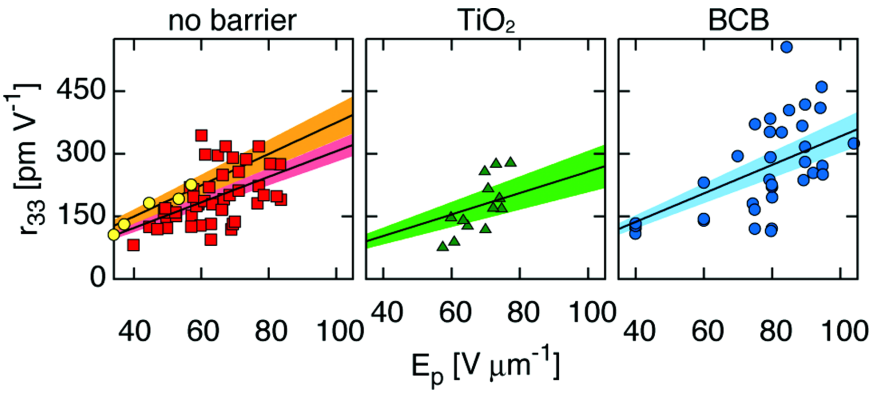

Figure 3.4: The r_{33} values of JRD1-based devices are plotted, as measured by attenuated total reflection (ATR) with no barrier layer (yellow dots) and by Teng-Man with no barrier layer (red squares), with a TiO_2 layer (green triangles), and with a BCB layer (blue dots), as a function of the average electric field during poling. Poling efficiencies are plotted as black lines (values listed in Table 3.1). Orange, red, blue, and green shaded wedges represent the error in the poling efficiency at the 95% confidence level.

process is substantially improved when a low conductivity layer is present. Conversely, in poling situations without a barrier layer, high leakage current results in a corresponding drop in poling field that limits r_{33}. To show this, the r_{33} values of JRD1-based devices with no barrier layer (red squares), with a TiO_2 layer (green triangles), and with a BCB layer (blue dots) were plotted as a function of the average poling field across the EO core during poling. The average electric fields during poling on JRD1-based devices with no barrier layer or with a TiO_2 layer were limited to $\leq 80\ V\mu m^{-1}$. Higher average electric fields during poling (between 80 and 105 $V\mu m^{-1}$) were only achieved across the EO layer on devices containing a BCB layer. The change in voltage from the applied voltage during poling was limited to below 1% by the BCB layer; this is contrasted with a 20% on aver- age change without the BCB layer (see figure A9 in Appendix 1). This result leads us to the conclusion that the presence of the BCB layer permits access to higher poling fields; and BCB is an essential tool in the screening of novel high number density materials that display high conductivity at the T_g.

Access to higher poling fields afforded by the BCB layer led to maximal EO coefficients; r_{33} values higher than 400 $pm\ V^{-1}$ were observed in multiple experiments on JRD1-based devices at poling fields $\geq 85\ V\ \mu m^{-1}$. In one device an r_{33} value of $556 \pm 90\ pm\ V^{-1}$ was obtained at a poling field of $85\ V\ \mu m^{-1}$. This impressive measurement corresponds to exceptionally low current during poling, suggesting that further optimization of the device architecture could lead to real devices with similarly large r_{33} values. From over 40 poling experiments of the BCB-containing devices, we found the mean poling efficiency, r_{33}/E_p, was $3.4 \pm 0.2\ (nm/V)^2$, which agrees with results found by attenuated total reflection (ATR) methods, within experimental error. [112, 113] Eliminating leakage current during poling resulted in a factor of 1.6 ± 0.4 increase in the maximum observed r_{33} for JRD1. Use of a BCB layer resulted in a similar increase in the maximum r_{33} observed for chromophores YLD-124 and JSLD5 (table 3.1). Here, YLD-124 was examined as a monolithic system, whereas previously it had only been used in a guest-host system. The poling efficiency of 25% w/w YLD-124 in PMMA was previously determined to be 1 $(nm/V)^2$ under ideal conditions and would therefore require substantially higher fields to obtain r_{33} values that could compete with monolithic YLD-124. [114]

While this paper focuses on simple device structures for measuring EO coefficients, charge barrier layers are also important in more complex waveguide EO devices, such as Mach-Zehnder, that depend on parallel plate or coplanar electrode configurations. BCB has in fact been used for decades in microfabrication facilities and has standard recipes for etching that are compatible with microscale or nanoscale patterning such as lining the walls of silicon rail waveguides. The low dielectric constant of BCB ($\varepsilon = 2.65$) makes it less than ideal as a cladding layer during operation of an EO device, though it is still desirable as a charge barrier during poling. [115, 116] What we have demonstrated in these experiments could be utilized by device engineers as a conceptual starting point for integrating BCB barrier layer into nanoslot silicon photonic devices; however, it is critical that a successful charge barrier layer like BCB be used in simple devices for accurately evaluating the EO performance of high performance, high number density chromophores.

3.5 Conclusion

In conclusion, BCB was employed as a barrier layer material for EO devices to reduce conductance during electric field poling. The BCB layer was more effective at reducing conductance in comparison to a sol-gel derived TiO_2 layer that has been one of the most widely employed materials for barrier layers. The maximum observed EO coefficients of three high number density EO materials (including the new chromophores JRD1 and JSLD5) were significantly improved by incorporating a $60-100$ nm thick BCB layer between the ITO electrode and the EO layer. The efficacy of BCB as a barrier layer to prevent current leak-through shows great potential for a wide-range of photonics applications.

This material is based upon work supported by the National Science Foundation (Grant Nos. DMR-1303080, DMR-1005819, and DMR-0120967). Any opinions, findings, and conclusions or recommendations expressed in this material are those of the author(s) and do not necessarily reflect the views of the National Science Foundation. The authors would like to thank Bruce E. Eichinger for the helpful discussion and calculations, and Viviana Gonzalez for pioneering work on neat YLD-124. The authors also acknowledge partial financial support from the Air Force Office of Scientific Research (FA9550-10-1-0558, FA9550-09-1- 0682). W. Jin also thanks the State-Sponsored Scholarship for Graduate Students from

China Scholarship Council. Part of this work was conducted at the University of Washington Nanotechnology User Facility, a member of the NSF National Nanotechnology Infrastructure Network.

3.6 General Information

Benzocyclobutene (BCB) was purchased from Dow Corporation as a solution in mesitylene (Cyclotene 3022-46). Mesitylene and 1,1,2 trichloroethane (TCE) was purchased from Sigma Aldrich. TCE was purified via vacuum distillation prior to use. Indium tin oxide (ITO)/glass slides were purchased from Thin Film Devices, Inc. Variable angle spectroscopic ellipsometry (VASE) was carried out on an ellipsometer purchased from J. A. Woollam Co., Inc. Optical profilometry measurements were carried out on an NT-2000 model profilometer, provided by WYKO Corporation. In situ Teng-Man ellipsometry was carried out on a home built device. [21]

The IUPAC names (followed by their common monikers in parenthesis) of the three high number-density, monolithic chromophore systems (Figure 3.3) examined in the study are 2-[4-(3-[3-[2-(4-[Bis-[2-(tert-butyl-dimethyl-silanyloxy)-ethyl]-amino]-phenyl)-vinyl]-5,5-dimethyl-cyclohex-2-enylidene]-propenyl)-3-cyano-5-phenyl-5-trifluoromethyl-5H-furan-2-ylidene]-malononitrile (**YLD-124**), 2-[4-(3-[3-[2-(4-[Bis-[2-(tert-butyl-diphenyl-silanyloxy)-ethyl]-amino]-phenyl)-vinyl]-5,5-dimethyl-cyclohex-2-enylidene]-propenyl)-3-cyano-5-phenyl-5-trifluoromethyl-5H-furan-2-ylidene]-malononitrile (**JRD1**), and 1-[2-[(6E)-4,4-bis([[(tert-butyldiphenylsilyl)oxy]methyl])-6-[(2E)-3-[4-cyano-5-(dicyanomethylidene)-2-phenyl-2-(trifluoromethyl)-2,5dihydrofuran-3-yl]prop-2-en-1-ylidene]-2-[(E)-2-[4-[methyl(2-[[6-oxo-6-(4-[[(2-oxo-2H-chromen-7-yl)oxy]carbonyl]phenoxy)hexanoyl]oxy]ethyl)amino]phenyl]ethenyl]cyclohex-1-en-1-yl]ethyl]4-[[(2-oxo-2H-chromen-7-yl)oxy]carbonyl]phenyl hexanedioate (**JSLD5**). (see figure 3.3)

Device Fabrication: ITO/glass substrates were scrubbed with a cotton swab and multi-purpose detergent. Then slides were rinsed with deionized water, and fixed vertically on a polyethylene block where they were first immersed in acetone and sonicated for 5-10 minutes followed by immersion in isopropanol and another sonication for 5-10 minutes.

BCB solution was diluted to 20% w/w in mesitylene and filtered through a 0.45 μm

PTFE filter via syringe and applied directly to a clean ITO/glass substrate and spin cast at 4000 rpm for 60 seconds. The resulting films were dried on a hot plate at 120 °C for 10-20 minutes to remove residual solvent prior to curing according to the procedure provided by Dow Corp. [117] The thickness of the BCB layer was then confirmed by VASE in the wavelength range of 300-1700 nm prior to adding the electro-optic (EO) layer. A 2% w/w solution of polymethyl methacrylate (PMMA) in TCE was spin cast onto devices over the BCB layer at 4000 rpm.

Titanium dioxide (TiO_2) barrier layers were fabricated according to previously published methods. [108]

Solutions of 9-12% w/w EO material in TCE were filtered through a 0.2 μm PTFE filter and spin cast on ITO/Glass substrates, with and without barrier layers. EO films were spin cast in three stages, 500 rpm for 5 seconds, 850 rpm for 30 seconds, followed immediately by 2000 rpm for 30 seconds. The films were then dried on a hot plate at 65 °C for half an hour, and then further cured in a vacuum oven at 65 °C overnight. The thickness of the EO film was then measured to be around 1-2 μm via optical profilometry. Finally, gold electrodes were deposited on top of the films by sputter coating, thus completing a prototype device.

3.7 Statistical analysis [4]

: The analysis of the EO coefficients, r, as a function of the poling field, E, provides a measure of the efficiency $m = r/E$. For the purposes of data analysis we assume that the model for the relation of r to E is proportional, $r = mE$, Furthermore, we assume there is no error in any of the E values. However there are concerns about how the data should be weighted: specifically, it is possible that the larger field values produce larger errors in the r-values. We therefore start with a robust model that will encompass the various possible ways the data might be analyzed. Our conclusion, at the end of the analysis is that the various methods give essentially the same answers within experimental error and therefore any of the methods can be relied upon. Therefore, a weighted least-squares analysis of the data is the starting point: the standard error of any quantity, q, is given as,σ_q and the

variance of the quantity is σ_q^2.The standard error of r, σ_r^2, defined as:

$$\sigma_r^2 = \frac{1}{N}\sum_{k=1}^{N}(w_k^2)(r-\hat{r})^2 \tag{3.1}$$

There are N data points enumerated by $k = 1, 2LN$. For each of the data points, $\{E_k, r_k\}$, the individual weights,w_k, must be given *apriori* and should depend on E. A general requirement of the weights is that $\sum_{k=1}^{N}(w_k^2) = N$. In general, the weights are taken to be related to the errors of the individual measurements, $\sigma_k \equiv \sigma_{r_k}$, where $w_k \propto \sigma_k^{-1}$, and this analysis is closely related to a chi squared analysis. Given the model, which depends upon a single parameter, m, the equation for the optimum efficiency or slope is $\frac{d\sigma_r^2}{dm}$, and yields the expression:

$$\begin{aligned} 0 &= \sum_{k=1}^{N}(w_k^2)(r_k-\hat{r}_k)\left(\frac{d\hat{r}_k}{dm}\right) \\ &= \sum_{k=1}^{N}(w_k^2)(r_k - mE_k)E_k \\ m &= \frac{\sum_{k=1}^{N}(w_k^2)(r_kE_k)}{\sum_{k=1}^{N}(w_k^2E_k^2)} \end{aligned} \tag{3.2}$$

The variance of the slope, m, may be found from the variance of the data given above:

$$\sigma_m^2 = \sum_{k=1}^{N}\left(\frac{dm}{dr_k}\right)^2\sigma_k^2 = \sum_{k=1}^{N}\left(\frac{(w_k^2E_k)}{\sum_{k=1}^{N}(w_k^2E_k^2)}\right)^2\sigma_k^2 = \frac{\sum_{k=1}^{N}\left((w_k^2E_k)\sigma_k\right)^2}{\left(\sum_{k=1}^{N}(w_k^2E_k^2)\right)^2} \tag{3.3}$$

Method 1: The simplest analysis is to assume that all of the weights are the same: $w_k = 1\forall k$. This implies that the error in the r values is independent of E, or that $\sigma_r = \sigma_k\forall k$. Then the slope, the variance in r and the variance of the slope m are:

$$m = \frac{\sum_{k=1}^{N}(r_kE_k)}{\sum_{k=1}^{N}(E_k^2)} \qquad \sigma_r^2 = \frac{1}{N}\sum_{k=1}^{N}(r_k - mE_k)^2 \qquad \sigma_m^2 = \frac{\sigma_r^2}{\sum_{k=1}^{N}(E_k)^2} \tag{3.4}$$

This form of the variance in the slope demonstrates that as one accumulates more data, the error in the slope will decrease, and will decrease approximately as $1/\sqrt{N}$.This form also demonstrates that data collected at larger field values will be better at reducing the error estimate.

Method 2: It is not known whether the error will increase with increasing E or be rather constant. So far we have assumed (in method 1) that the error in r is independent of E. However, if the error in r is proportional to the field then we should assume that $w_k^{-1} \propto \sigma_k \propto E_k$. Data points with larger E then are weighted less in the averaging. Using the constraint on the weights that they must sum to give us a complete description of the weights:

$$w_k = \frac{\alpha}{E_k} \qquad \alpha^2 = \frac{N}{\sum_{k=1}^{N}\left(\frac{1}{E_k^2}\right)} \tag{3.5}$$

In this case, the equation for the mean is (using the above general forms):

$$m = \frac{\sum_{k=1}^{N}\left(\frac{r_k}{E_k}\right)}{N} \tag{3.6}$$

Using the normalized weights, we can obtain an expression for the variance of r:

$$\sigma_r^2 = \frac{1}{N}\sum_{k=1}^{N}(w_k^2)(r-\hat{r})^2 = \frac{\alpha^2}{N}\sum_{k=1}^{N}\left(\frac{r_k}{E_k} - m\right)^2 = \frac{\sum_{k=1}^{N}\left(\frac{r_k}{E_k} - m\right)^2}{\sum_{k=1}^{N}\left(\frac{1}{E_k^2}\right)} \tag{3.7}$$

If we assume the variance in is the average of the individual variances then we find:

$$\sigma_k = \alpha\left(\frac{r_k}{E_k} - m\right) \tag{3.8}$$

The combination of these two expressions gives us an estimator to the variance of the slope.

$$\sigma_m^2 = \sum_{k=1}^{N}\left(\frac{dm}{dr_k}\right)^2\sigma_k^2 = \sum_{k=1}^{N}\left(\frac{\alpha}{NE_k}\left(\frac{r_k}{E_k} - m\right)\right)^2 = \frac{\sigma_r^2}{N} \tag{3.9}$$

Method 3: We continue with the weighting assumed in Method 2, which is that the weights are proportional to E_k^{-1}. Eqn 3.9 makes it clear that E_k^{-1} act as weights in the variance of the slope. If we assume that the σ_k^2 can be replaced by the average variance of r, σ_r^2, from Eqn 3.7 into Eqn 3.9, then we find the simplified equation for the variance that does not contain any additional weights for each of the deviations:

$$\sigma_m^2 = \frac{1}{N}\sum_{k=1}^{N}\left(\frac{r_k}{E_k} - m\right)^2 \tag{3.10}$$

This is the same expression for the slope (3.6) and the variance in the slope (3.10) that one would obtain if one assumed uniform weighting and that the fundamental model was $m = \hat{r}/E$. We can use the data set for r as a function of E for the case of JRD1-based devices that include the BCB layer. The analysis of the slope and the error in the slope is given for each of the three methods:

Table 3.2: Comparison of mean and standard error across three methods of analysis.

Method	1(eqn 3.4)	2(eqn 3.6, 3.9)	3(eqn 3.6, 3.10)
Mean: $m[nm/V]^2$	3.4162	3.3410	3.3410
Error:$\sigma[nm/V]^2$	0.1899	0.1622	0.1848

The numbers are shown beyond significance to illustrate the differences as a result of the various methods used to compute them. The comparison of the three methods shows that one obtains nearly the same means and the same errors. The weighted method (method 2) gives the lowest error but as all errors must be rounded to 0.2 it is clear any of the three methods will give the same error. Therefore we have confidence that the method of analysis is sufficient for the data at hand, and the results are robust.

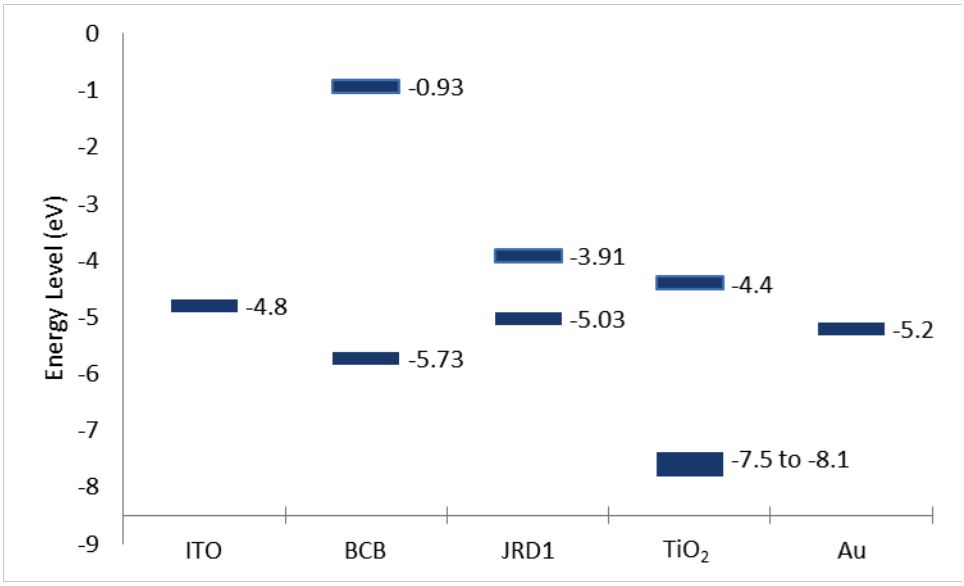

Figure 3.5: Energy level diagram of materials used in device fabrication.

3.7.1 HOMO-LUMO Level Analysis

HOMO (highest-occupied molecular orbital) and LUMO (lowest-unoccupied molecular orbital) energy levels for materials used in this study were determined by various methods. Energy levels for TiO_2 were taken from the literature, as were work functions for gold and ITO electrodes. [118–120] HOMO-LUMO energy levels of BCB were calculated by density functional theory. Geometry and energy levels of the BCB model compound in figure 3.6 were calculated using the B3LYP method with a 631G* basis set.

Band gap energy was estimated using cyclic voltammetry and carried out on 2.0 mM solutions of JRD1 in dry dichloromethane (DCM) previously purged with nitrogen (figure 3.7). Red-ox potentials were referenced to a solution of freshly sublimed ferrocene (2.0 mM in DCM). Tetrabutylammonium hexafluorophosphate (Bu_4NPF_6) was used as the supporting electrolyte at 0.1 M concentration. The bandgap energy of JRD1 in thin films was also estimated as the onset of absorption using normalized spectral data (figure 3.7). The wavelength of maximum absorption (λ_{max}) was measured in solutions of chloroform and from films cast with 1,1,2 trichloroethane.

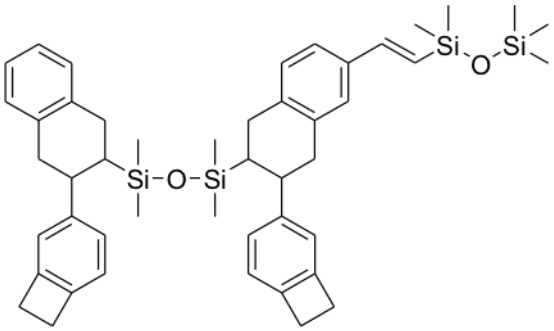

Figure 3.6: Structure of BCB model compound used for HOMO-LUMO calculations.

	$\lambda^{max}_{\mathrm{CHCl_3}}$	λ^{max}_{FILM}	$\varepsilon^{-1}_{\mathrm{CHCl_3}} \times 10^4$	$\Delta E(UV)$	E_{ox}	E_{red}	$\Delta E(CV)$
	$/nm$	$/nm$	$/Mcm^{-1}$	$/eV$	$/V$	$/V$	$/eV$
JRD1	780	800	6.89	1.14	0.395	−0.888	1.11

3.7.2 Conductivity Calculation for JRD1 and BCB

The conductivity of EO material and BCB can be calculated according to the current and voltage of ITO/EO material/gold and ITO/BCB/gold devices via wire model: $\sigma_i = (I_i/V_i)(d_i/A_i)$, where I_i is the current across the layer i (A), V_i is the voltage across the layer i (V), d_i is the thickness of the material (m), A is the area of the poling area ($\sim 9.36\times10^{-6}\ m^2$). As the result, the average conductivity at the glass transition temperature of EO material is $2.1\times10^{-7} \pm 5.7\times10^{-8}\ Sm^{-1}$. And the conductivity of BCB is estimated as $1.5\times10^{-8}\ Sm^{-1}$ based on the measurement of a 1.5 μm film.

3.8 Results & Discussion

Solubility of the BCB layer: Fully cured BCB films are highly robust and orthogonal to TCE and other common solvents used in device fabrication. To demonstrate this, neat TCE was dropped onto the BCB films and spin cast immediately at room temperature under ambient pressure. The thicknesses of the BCB layer before and after exposure to TCE are compared in Table SĐĘ. No significant change in the thickness of BCB layer was observed, it was therefore assumed that spin casting EO material on top of the BCB layer using TCE

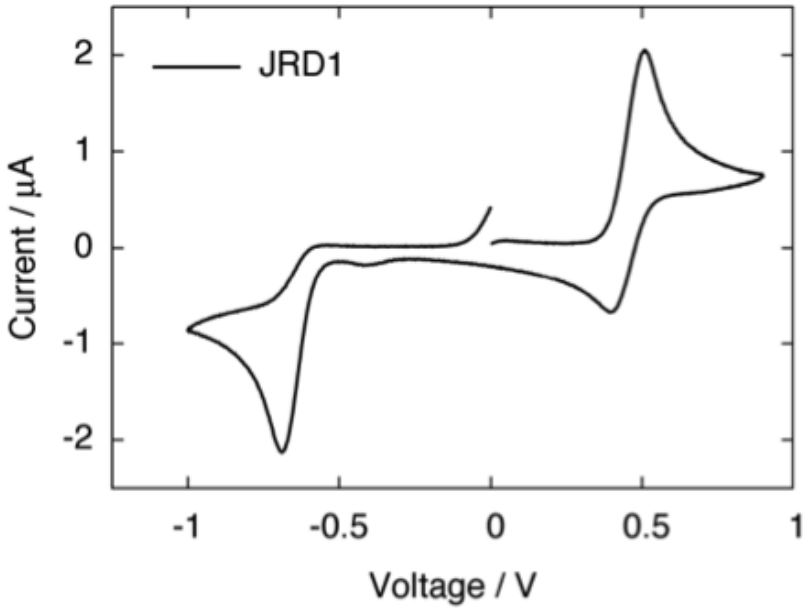

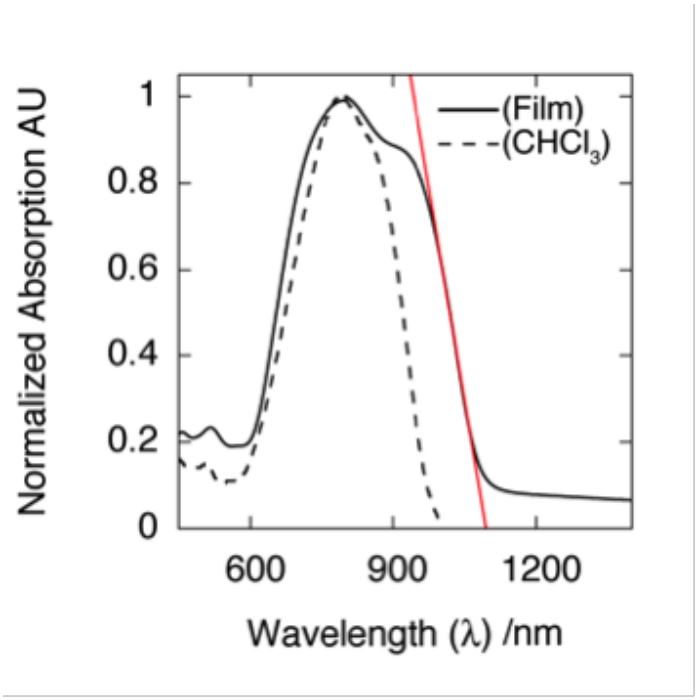

Figure 3.7: The absolute HOMO and LUMO energies and band gap of JRD1 were estimated from cyclic voltammetery and optical absorption according to a previously published procedure. [63] Potentials are plotted relative to Ag/Ag^{+} reference electrode (0.01 M $AgNO_3$ in acetonitrile with 0.1 M Bu_4NPF_6 electrolyte).

as the solvent had no significant effect on the thickness of the BCB layer.

Table 3.3: The thicknesses of fully cured BCB films before and after exposure to TCE

Sample Number	Average Thickness before exposure to TCE / nm	Average Thickness after exposure to TCE / nm
A	114.2 ± 0.3	116.3 ± 0.3
B	94.8 ± 0.4	95.6 ± 0.4
C	77.7 ± 0.6	81.7 ± 0.5

3.8.1 The effect of an adhesion layer

Surface energy mismatch of the EO material and BCB frequently occurred during the spin casting process, resulting in textural inconsistencies in the EO film (i.e., "pinholes". The appearance of pinholes in the films substantially reduced the number of measureable devices in a given batch of samples. PMMA was therefore utilized as an adhesion layer between the BCB layer and the EO layer to improve EO film quality. The thicknesses of the PMMA adhesion layer before and after exposure to TCE are shown in Table SII. The final thickness of the adhesion layer after being exposed to the EO solution (roughly 90% TCE) during spin casting was presumed to be around 20−30 nm; however, the additional PMMA layer was not observed to affect poling efficiencies. To verify this, a batch of samples having acceptable film quality without a PMMA layer between the BCB layer and the EO layer were fabricated and poled. A comparison of the r_{33}/E_p measured on JRD1-based devices with BCB but without a PMMA layer and those with BCB and a PMMA layer shows that the poling efficiencies of these two types of devices were essentially the same (Figure 3.8 Left). To further verify that the increase in observed EO activity could not be attributed to the PMMA layer, the r_{33}/E_p of JRD1-based devices was examined with the PMMA layer directly on top of the ITO/glass substrate (Figure 3.8 Right). The poling efficiencies of samples without a barrier layer were not significantly different than those with a PMMA layer. Finally, to verify that the reduction in device conductance could not be attributed to

the PMMA layer, the change in current and the maximum current were plotted as a function of E_p (Figure 3.9). The PMMA layer only served to improve film quality.

Table 3.4: The thicknesses of PMMA adhesion layer before and after exposure to TCE

Sample Number	Average Thickness before exposure to TCE / nm	Average Thickness after exposure to TCE / nm
A	137.8 ± 0.9	23.6 ± 1.4
B	112.5 ± 1.2	21.8 ± 2.2

3.8.2 Current during poling

The in situ elipsometric technique (Teng-Man) employed to measure r_{33}allows for monitoring of optical and electrical information during the electric field poling process. [13, 19, 21] A typical in situ poling electrical trace generated during poling of an individual JRD1-based device without a barrier layer is shown in Figure 3.10 Left. It can be observed that current increased dramatically after the onset of the glass transition temperature (time ∼350s), from 17.1 μA before poling to a maximum of 336 μA during poling. The $r_{33}$of this particular device was 125 ± 44 $pm\ V^{-1}$. In the presence of the BCB layer, the current only slightly increased from 16.4 μA before poling to a maximum of 23 μA during poling (Figure 3.10 Right). This dramatic drop in current resulted in an $r_{33}$of 556 ± 90 $pm\ V^{-1}$. To evaluate the current suppression in the devices with the BCB layer, we plot the max current and Δcurrent denoted in Figure 3.8 against the average electric field during poling (Figure 3.11).

Reduced device conductance and background current resulted in a higher electric field during poling. Figure 3.12 shows the average electric field during poling as a function of the applied electric field on three different types of JRD1-based devices: with no barrier layer, with a TiO2 layer and with a BCB layer. A perfect correlation between the average electric field during poling and the applied electric field prior to poling would mean that the difference in electric field before poling and during poling was zero. This is clearly not the case for devices without a barrier or those with a TiO_2 barrier; however devices containing a

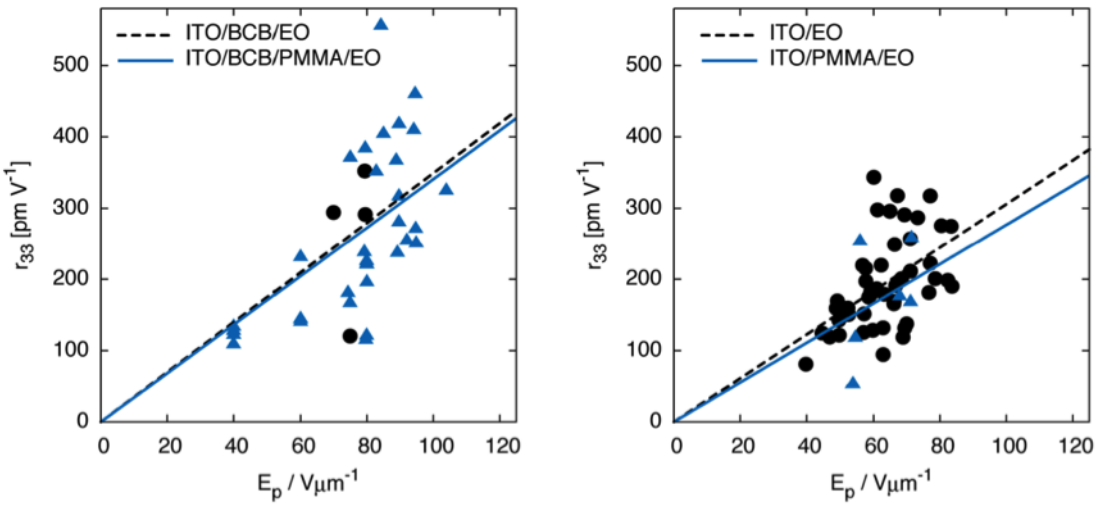

Figure 3.8: Left: The EO coefficient (r_{33}) of JRD1-based devices with a BCB blocking layer, without a PMMA layer (black dot) and with a PMMA layer (blue triangles) is plotted as a function of average electric field strength during poling. Right: The EO coefficient (r_{33}) of JRD1-based devices without a barrier layer, without a PMMA layer (black dots) and with a PMMA layer (blue triangles) is plotted as a function of average electric field strength during poling.

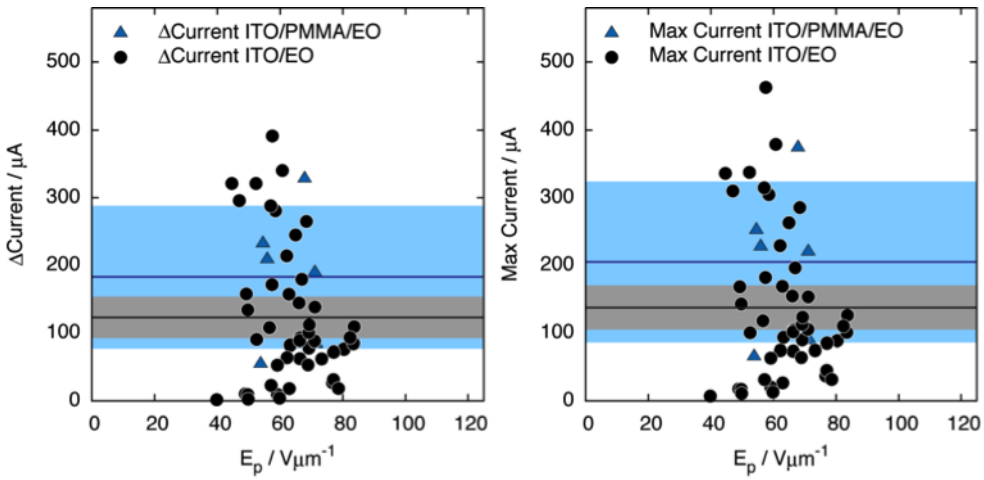

Figure 3.9: The change in current (Δcurrent, left) and the maximum current (right) are plotted as a function of the average electric field strength during poling. Black dots represent samples with a PMMA layer, and blue triangles represent samples without a PMMA layer. The mean and 95% confidence levels are shown in a black line and a grey shaded region for samples with a PMMA layer, and shown in a blue line and a blue shaded region for samples with no PMMA layer. The blue band is wider than the grey band simply because fewer samples are available.

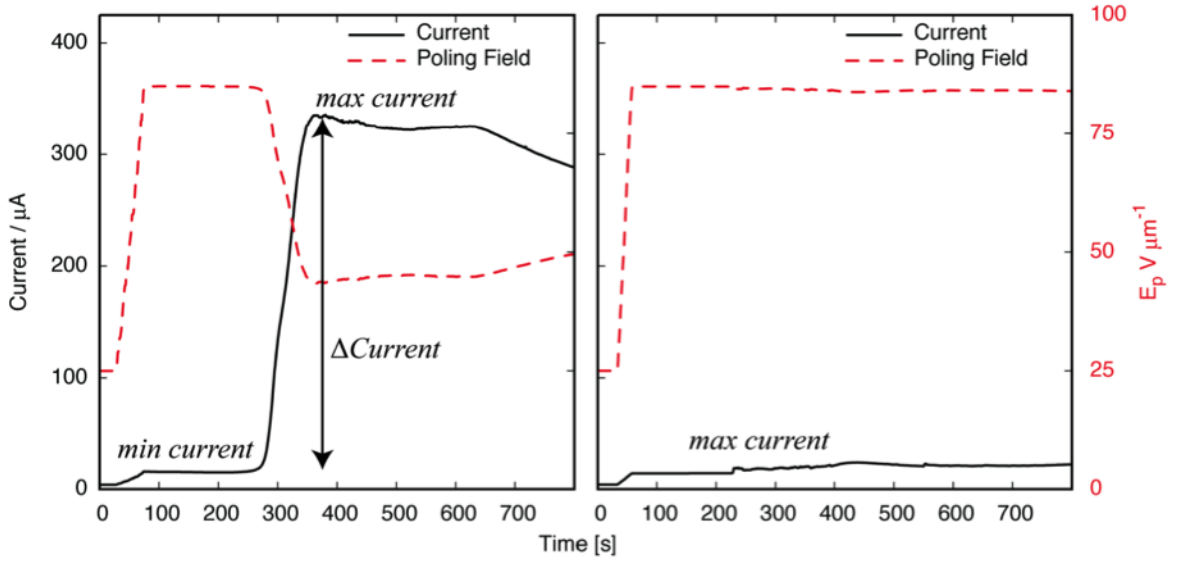

Figure 3.10: Electric field (red dash line) and current (solid line) during the poling process in individual JRD1-based devices Left: without a BCB layer (r_{33}= 125 ± 44 $pm\ V^{-1}$) and Right: with a BCB layer (r_{33}= 556 ± 90 $pm\ V^{-1}$) are plotted as a function of time. Poling occurred between 350 and 600 seconds.

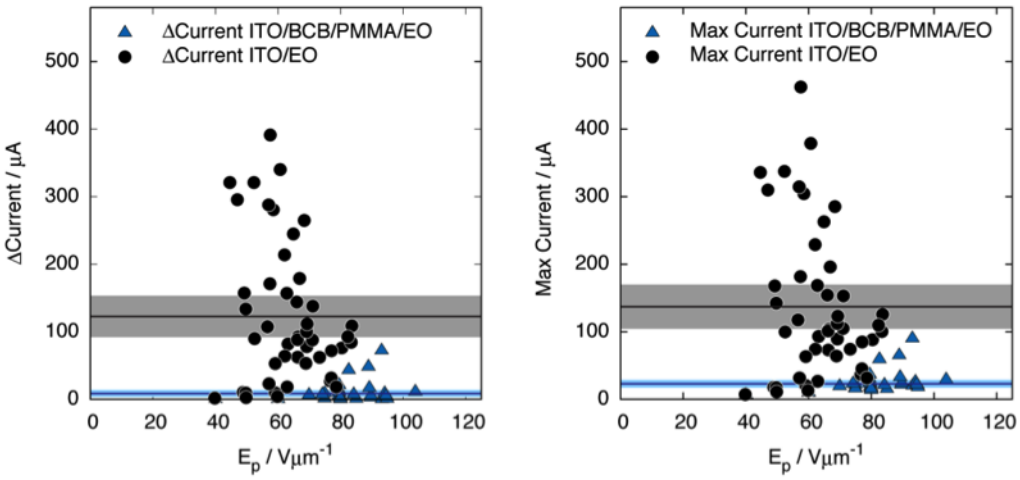

Figure 3.11: The change in current (Δcurrent, left) and the maximum current (right) are plotted as a function of average electric field during poling with no barrier layer (black dots), and with the BCB barrier layer (blue triangles).The statistical mean of each data set is plotted as a solid line and the error in the mean is plotted as a shaded region at the 95% confidence level.

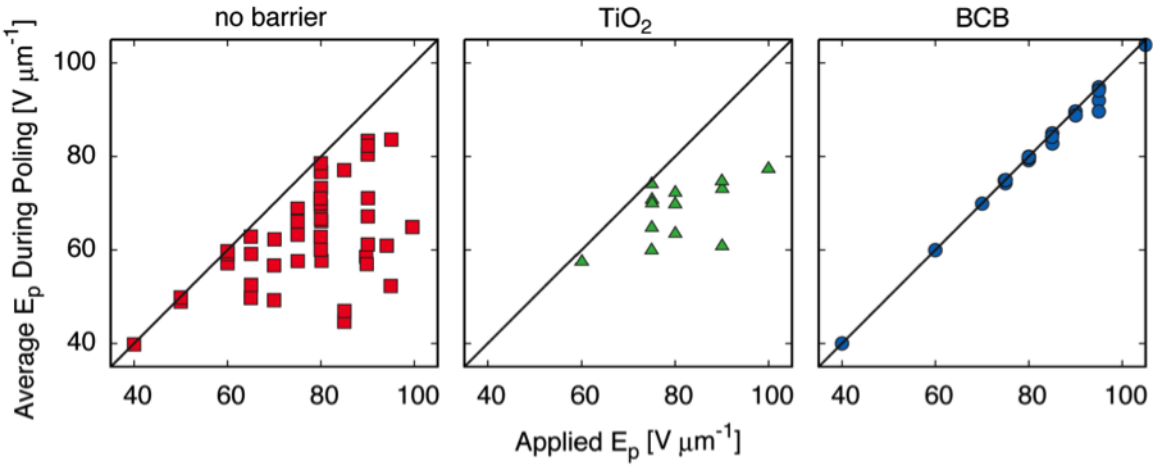

Figure 3.12: The applied voltage and the average voltage during poling from JRD1-based devices with no barrier layer (red squares), with a TiO_2 barrier layer (green triangles) and with a BCB barrier layer (blue dots). The solid line (in all 3 figures) indicates a perfect correlation, Δ E=0.

BCB layer approached a difference of zero. Further optimization of the fabrication process could result in an even better correlation. To quantify this discrepancy for each device architecture the root mean squares of the change in electric field ($\sigma_{\Delta E}$) were determined to be 18.53 $pm\ V^{-1}$, 14.47 $pm\ V^{-1}$, and 1.18 $pm\ V^{-1}$, for no barrier, a TiO_2 barrier, and a BCB barrier layer respectively.

3.8.3 Analysis of average electric field strength during the poling process

The sample temperature is recorded as a function of time (Figure 3.13). The first 30 seconds of the acquisition are discarded. The average (or effective) voltage, $\langle V \rangle$, current, $\langle I \rangle$, and resistance $\langle V/I \rangle$ are calculated from the voltage and current (both functions of time) only over the time window when the sample is at its maximum temperature (just under the glass transition temperature). The poling starts at time t_s (for start time) and ends at time t_e (for end time). The fitting determines t_s and t_e: The temperature profile is fit to a model consisting of three piecewise curves. The first part of the temperature curve is fit to a linear function as the temperature increases at a linear rate up to when it is switched off at time t_s. The second part of the curve is fit to a straight line whose slope, m, is constrained, $0.01 < \mathrm{m} < 0$ degrees/sec, until time t_e, when the sample is allowed to cool. The third region of the curve is fit to an exponentially decaying function. The fitting is done by a Marquard-Levenberg least squares procedure, where the start and end times (t_s and t_e) are adjustable parameters found by the fitting. The actual time window over which the averaging takes place is from $t_s + 16$ sec to $t_e + 16$ seconds. The 16 second delay accounts for some settling time. The set poling voltage is determined as the average voltage well within the first temperature region and well before the maximum temperature is reached.

3.9 The effect of barrier layer thickness

Previous research has shown that current reduction is largely dependent on the thickness of the barrier layer. [102] To optimize the effect of the BCB layer, experiments were conducted on JRD1-based devices with a BCB layer at different thicknesses. No clear correlation with conductance and BCB layer thickness was observed. All devices that survived the poling process showed similarly low conductance.

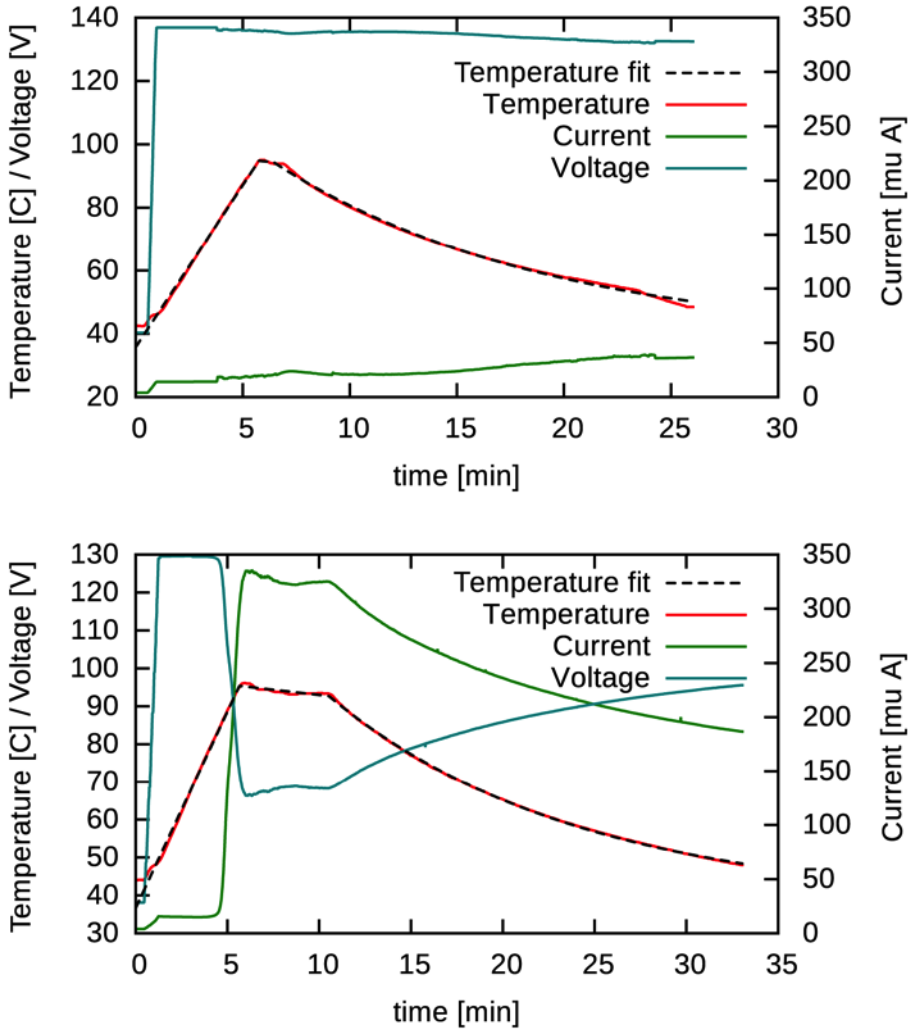

Figure 3.13: The temperature (red solid line), voltage (blue solid line) and current (green solid line) during the poling process with the fit to the temperature (black dash line) on representative JRD1-based devices without a BCB layer (bottom) and with a BCB layer (top) are plotted as a function of time. The fit to the temperature is overlaid on the experimental temperature curve. The fitting times are from $t_s + 16$ sec to $t_e + 16$ seconds where $t_s = 5.75$ min and $t_e = 6.45$ min for the BCB based device and $t_s = 5.65$ min and $t_e = 10.52$ min for the device without a barrier layer.

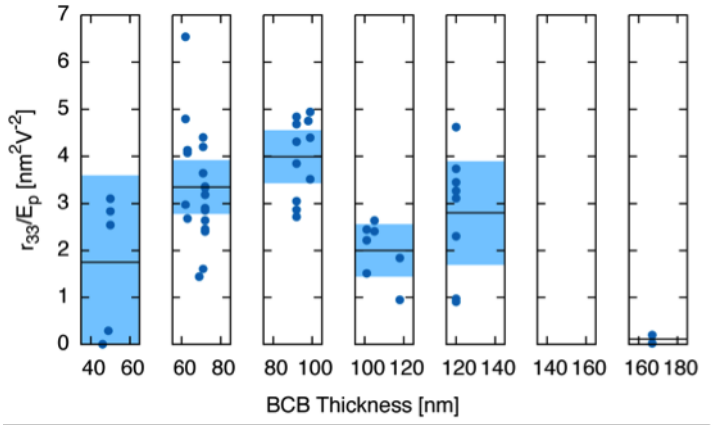

Figure 3.14: Poling efficiency (r_{33}/E_p) of JRD1-based devices with a BCB layer is plotted as a function of BCB layer thicknesses. The blue solid line is the mean value for the samples in the specified thickness range. The blue shaded region is the error reported at the 95% confidence level.

Some data collected from devices that were not structurally sound were discarded. Specifically, a total of 27 samples were fabricated at thicknesses ranging from 40-60 nm, of which only 5 appeared to pole according to the optical data recorded by the Teng-Man instrument. Similarly, large failure rates of 70% were observed on devices with thicknesses above 120 nm. It is not uncommon for samples to fail during poling. In some cases failure could be directly attributed to short-circuiting of the device prior to poling, poor adhesion of the gold electrode or poor adhesion of the lead wires and these data are discarded for all device architectures regardless of thickness measurements. Failure rates for devices in the thickness range of 40-60 and 120-200 nm greatly exceeded the typical failure rate of 30-50% observed in devices without a barrier. Devices with a 60-100 nm BCB layer fell within the typical failure rate of 30-50% and for this reason we assume that this is the ideal thickness for the BCB layer Beyond that, comparing poling data showed that optimal poling efficiency might also be attributed to BCB layer thickness (Figure 3.14). The 60-100 nm window was observed to be significantly more favorable in terms of EO activity. Thus, data in this thickness range was reported in the main text as the optimal barrier layer thickness.

Chapter 4

40 GBD 16QAM SIGNALING AT 160 GB/S IN A SILICON-ORGANIC HYBRID MODULATOR [3]

4.1 Abstract

We demonstrate for the first time generation of 16-state quadrature amplitude modulation (16QAM) signals at a symbol rate of 40 GBd using silicon-based modulators. Our devices exploit silicon-organic hybrid integration, which combines silicon-on-insulator slot waveguides with electro-optic cladding materials to realize highly efficient phase shifters. The devices enable 16QAM signaling and quadrature phase shift keying at symbol rates of 40 GBd and 45 GBd, respectively, leading to line rates of up to 160 Gb/s on a single wavelength and in a single polarization. This is the highest value demonstrated by a silicon-based device up to now. The energy consumption for 16QAM signaling amounts to less than 120 fJ/bit-one order of magnitude below that of conventional silicon photonic 16QAM modulators.[http://dx.doi.org/10.1109/jlt.2015.2394211]

4.2 Introduction

Fast and efficient in-phase/quadrature-phase (IQ) modulators are key elements for high-speed links in telecom and datacom networks. [121] To maximize the data rate that can be transmitted on a single wavelength channel, both large symbol rates and the ability to use higher-order modulation formats are essential. [122] At the same time, minimizing the power consumption of the devices is of utmost importance regarding high-density integration and scalability of interconnect counts.

Silicon photonics is a particularly attractive platform for realizing electro-optic (EO) modulators, leveraging mature complementary metal-oxide-semiconductor processing and enabling high-density integration of photonic devices along with electronic circuitry. However, the inversion symmetry of the silicon crystal lattice inhibits EO effects, thereby mak-

ing high-performance IQ modulators challenging. As a consequence, conventional silicon modulators have to rely on carrier depletion or carrier injection in p-n, p-i-n or metal-oxide-semiconductor structures [123–126]. Using a depletion-type device, generation of quadrature phase shift keying (QPSK) signals was recently shown at a symbol rate of 56 GBd resulting in a total line rate of 112 Gb/s. [127] However, when using more advanced modulation formats, the achievable symbol rates are still significantly lower-record values amount to 28 GBd demonstrated for dual-polarization 16-state quadrature amplitude modulation (16QAM) [128], which leads to a line rate (net data rate) of 112 Gb/s (93.3 Gb/s) encoded on each polarization. The performance of these devices is inherently limited by the underlying depletion-type phase shifters, which exhibit rather low efficiencies with typical voltage-length products $U_\pi L$ of 10 Vmm or more. As a consequence, large drive voltages, on the order of several volts, have to be used, leading to high energy consumption-for 16QAM modulation at 28 GBd, the modulation energy amounts to approximately 1.2 pJ/bit at a peak-to-peak drive voltage of 5 V_{pp}. [128] In addition, phase modulation based on the plasma dispersion effect is inevitably linked to amplitude modulation due to free-carrier absorption. This may eventually hamper the generation of advanced modulation formats with high order, where phase and amplitude of the signals have to be controlled independently of one another.

In this paper we show that silicon-organic hybrid (SOH) integration can overcome these limitations. We use silicon-on-insulator (SOI) slot waveguides [129] and combine them with EO cladding materials to realize Pockels-type phase shifters [74, 130–132]. SOH integration enables remarkably small voltage-length products of down to 0.5 Vmm measured at dc [133], and at the same time avoids unwanted amplitude-phase coupling and thereby enables higher-order modulation formats. [134,135] We demonstrate 16QAM and QPSK signaling at symbol rates of 40 and 45 GBd, respectively, leading to line rates (net data rates) of up to 160 Gb/s (133.3 Gb/s) on a single polarization. [136] This is the highest value achieved by a silicon-based modulator up to now. The energy consumption of our 16QAM device is estimated to be 120 fJ/bit at 40 GBd-one order of magnitude better than for best-in-class 28 GBd 16QAM all-silicon modulators. The work builds upon and expands our earlier experiments, where we have demonstrated energy-efficient on-off-keying [137], generation of multi-level

amplitude modulation at symbol rates of up to 84 Gb/s [134] and 16QAM modulation at 28 GBd. [138]

4.3 SOH Modulator

SOH modulators exploit interaction of the guided light with the EO cladding material under the influence of a modulating RF field. A cross section of an SOH Mach-Zehnder modulator (MZM) is depicted in Fig. 4.1(a). Each phase shifter consists of a silicon slot waveguide which is covered by the organic EO material. Fig. 4.1(b) and (c) show the optical E_x field. The discontinuity and the high refractive index contrast at the silicon-slot interface leads to a field enhancement within the slot and therefore to a large interaction of the light with the organic EO material. [131] The rails of the slot waveguide have a width of $w_{rail} = 240\ nm$ and are connected to a coplanar ground-signal-ground (GSG) transmission line via thin ($h_{slab} = 70\ nm$), slightly conductive, n-doped silicon slabs. A voltage applied to the transmission line will drop predominantly across the $w_{slot} = 80\ nm$ wide slot, thereby generating a large electric field. A plot of the E_x component of the electrical field can be seen in Fig. 4.1(d). This configuration ensures excellent overlap between the modulation field and the optical fields, leading to high modulation efficiency. The RF transmission line comprises the metal traces and the silicon slot waveguides and is designed for a wave impedance of 50 Ω. This is confirmed by measurements-at RF signals of up to 40 GHz, we find wave impedances of 50 ± 5 Ω.

The device was fabricated on an SOI wafer with a 220 nm-thick device layer and a 3 μm-thick buried oxide using electron beam lithography for defining the silicon waveguides and optical lithography for the metallization. The chip is coated with a mixture of the EO multi-chromophore dendritic molecule PSLD41 (75 wt.%) and the chromophore YLD124 (25 wt.%). [5, 133] The cladding material is poled by heating it close to its glass transition temperature while applying a poling voltage across the two floating ground electrodes of each MZM. Half of the voltage drops across each slot, resulting in an orientation of the chromophores in the slot which is antisymmetric with respect to the signal electrode, as indicated in Fig. 4.1(a) by green arrows. The blue arrows indicate the RF field applied to the GSG electrodes after poling, which results in opposite phase shifts in the two arms

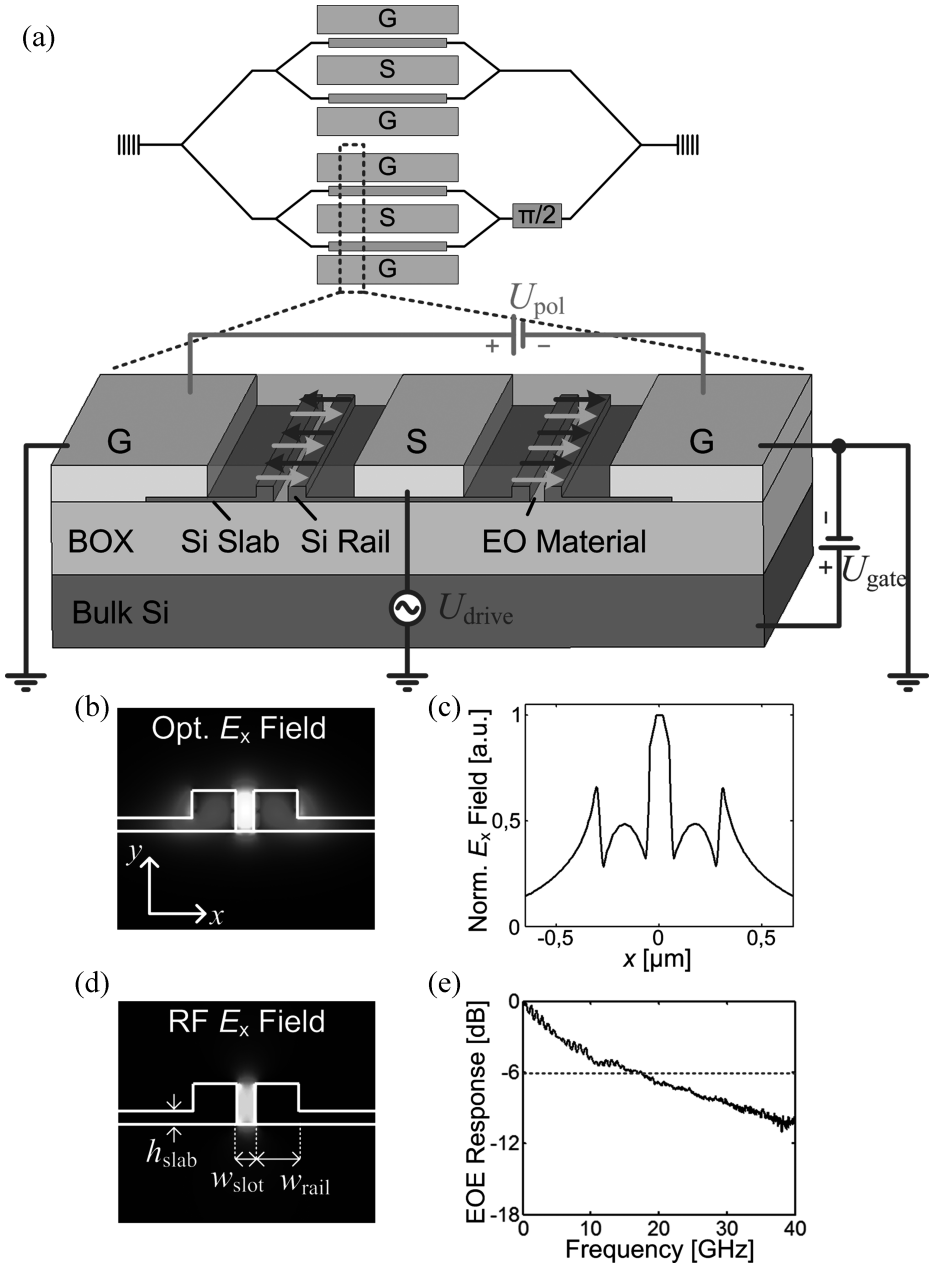

Figure 4.1: SOH modulator. (Continued on the following page.)

Figure 4.2: (a). Schematic of the IQ modulator and cross-section of a single SOH MZM. The slot waveguides have a rail width of $w_{rail} = 240\ nm$ and a slot width of $w_{slot} = 80\ nm$. As an EO cladding, a mixture of the chromophores YLD124 (25 wt.%) and PSLD41 (75 wt.%) is deposited via spin coating. Thin n-doped silicon slabs with ($h_{slab} = 70\ nm$) are used to electrically connect the rails to the metal strips of an RF transmission line in a GSG configuration. A poling process is used to align the chromophores in both waveguides along the same direction. Operating the device via the GSG transmission line results in opposite phase shifts in the two arms of the MZM (push-pull operation). The π-voltage at dc is $U_\pi = 0.9$ V. A gate voltage U_{gate} between the Si substrate and the SOI device layer improves the conductivity of the silicon slab, resulting in an EO bandwidth of the device of 18 GHz. (b) Contour plot of the normalized E_x component of the optical field in the slot waveguide. (c) Plot of the E_x-component of the optical mode field as a function of the horizontal position x at half the waveguide height ($y = 110\ nm$). Discontinuities of the E_x-component at the slot sidewalls lead to strong field enhancement in the slot. (d) E_x component of the electrical RF drive signal below the RC limit. The silicon slabs are doped such that the applied RF voltage drops predominantly across the slot. As a consequence, the RF mode and the optical mode are both well confined to the slot, resulting in strong interaction and hence in an efficient modulation. (e) Measured frequency response of a 1.5 mm-long MZM. The 6 dB electrical-optical-electrical (3 dB EO) bandwidth amounts to 18 GHz.

of the MZM and enables push-pull operation. For dc fields, the π-voltage of one push-pull MZM amounts to 0.9 V. Taking into account the device length of 1.5 mm, this corresponds to a voltage-length product of $U_\pi L = 1.35$ Vmm. This is higher than previously published values of SOH devices [133] and is attributed to different device geometry and the resulting difference in poling efficiency. The bandwidth of the SOH devices is dictated by the RC time constant of the slot waveguide: The slot corresponds to a capacitor which is charged and decharged via the resistive silicon slabs. To increase the conductivity of the slab by a charge accumulation layer and hence to increase the bandwidth, a static gate voltage U_gate is applied between the substrate and the top silicon layer [139], Fig. 4.1(a). A bandwidth measurement of the current MZM results in a 6 dB electrical-optical-electrical (3 dB electro-optical) bandwidth of 18 GHz, see Fig. 4.1(e), with significant potential for further improvement. [140] The roll-off is relatively smooth and resembles that of an RC low-pass, thereby still allowing 40 GBd 16QAM and 45 GBd QPSK signaling using root-raised-cosine Nyquist pulses.

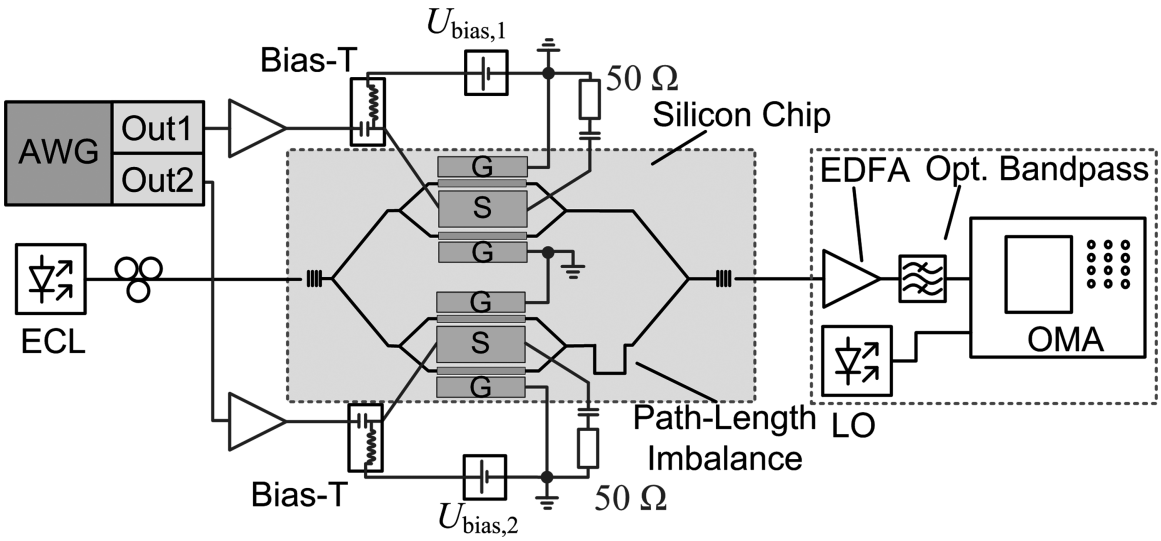

Figure 4.3: Schematic of the experimental setup. Two nested MZM form an IQ modulator. An intentional imbalance allows for adjusting the $\pi/2$ phase offset of the in-phase (I) and the quadrature-phase (Q) component by wavelength tuning. Electrical multilevel drive signals are generated by a Keysight M8195A AWG operating at 65 GSa/s, the outputs of which are amplified and coupled to the silicon chip via RF probes. Bias-Ts are used to connect a dc voltage for controlling the operation point. The optical output is amplified by an EDFA, bandpass filtered and subsequently fed into an OMA for intradyne detection. Standard digital post processing is performed at the OMA for equalization.

For practical applications of SOH devices, the long-term stability of the organic cladding is of high importance. Recently novel materials have become available, featuring glass transition temperatures of more than 130 °C while maintaining EO coefficients in excess of 100 pm/V. [141] The investigation of aging and temperature stability of organic EO materials is subject to ongoing research. It can be expected, that the stability of the materials can be further improved by synthetically modified chromophores that bear specific crosslinking agents for post-poling lattice hardening or by increasing the molar mass of the chromophores. The viability of the first approach has been demonstrated for similar EO compounds [36,142] where material stability of up to 250 °C has been achieved.

4.4 Experiment

The setup for the modulation experiments is depicted Fig. 4.3. Two MZM are nested in an on-chip IQ configuration. The parent Mach-Zehnder interferometer features a path length imbalance, which is used to adjust the $\pi/2$ phase shift between the I and the Q signal via wavelength tuning. The drive signals for QPSK and 16QAM modulation are generated by a Keysight M8195A arbitrary waveform generator (AWG) operated at 65 GSa/s. We use root-raised-cosine pulses with a roll-off factor of $\beta = 0.35$ to reduce the occupied spectral bandwidth and to exploit the benefits of a matched filter at the receiver. The transmitted data are derived from a pseudo-random bit sequence with a length of $2^{11} - 1$. After the AWG, the analog signals are amplified to peak-to-peak voltages of approximately 1.8 V_{pp} by two linear RF-amplifiers, which drive the GSG-electrodes of the on-chip IQ-modulator via microwave probes. A 50 Ω termination is used at the end of each transmission line to avoid back-reflection of the RF signal. For each MZM a dc voltage is applied to the device via bias-Ts to set the operating point of the modulator. To improve the bandwidth of the device, a static gate field of $E_{gate} = 0.1\ Vnm^{-1}$ is applied between the silicon substrate and the device layer. Grating couplers are used to couple laser light at $\lambda = 1550\ nm$ from an external cavity laser (ECL) to the silicon waveguide. After the device, the light is amplified by an erbium doped fiber amplifier (EDFA), followed by an optical band-pass filter (2 nm passband) to suppress out-of-band amplified spontaneous emission. An optical modulation analyzer (OMA) with two real-time oscilloscopes (80 GSa/s) serves as a receiver. A second ECL is used as a local oscillator (LO) for intradyne reception. Digital post-processing comprising polarization demultiplexing, phase recovery, compensation of the frequency offset between signal and LO, and channel equalization is performed by the OMA. The insertion loss of the silicon chip amounts to 27 dB, where 10-12 dB are caused by fiber-chip coupling losses. This rather high loss can be significantly reduced in future devices: By employing optimized grating coupler [143] or photonic wirebonds [144, 145] the coupling loss to the fibers can be reduced from 10 dB to less than 4 dB. The current losses of 5 dB in the 9 mm long access strip waveguide can be reduced to below 1 dB by improving the sidewall roughness and reducing the length. The strip-to-slot converters and multimode interference couplers are

already optimized and contribute only 1 dB to the total loss. To reduce the 11 dB losses of the 1.5 mm long slot waveguide to below 3 dB, asymmetric slot waveguide geometries can be used [146] together with an optimization of the doping profile of the phase shifter sections. We estimate that these measures will permit reducing the total on-chip excess loss of the device to less than 5 dB and the fiber-fiber insertion loss to less than 9 dB.

For testing the performance of the devices, we use QPSK signals up to a symbol rate of 45 GBd and 16QAM signals up to 40 GBd. Measurement of the bit error ratio (BER) allows for direct assessment of the signal quality. However, within our memory-limited record length of 62.5 μs, we can only measure a maximum of 2.8×10^6 symbols, which does not allow a measurement of BER smaller than 1×10^6. As a complementary measure of the signal quality, we therefore use the error vector magnitude ($\mathrm{EVM_m}$), which describes the effective distance of a received complex symbol from its ideal position in the constellation diagram, using the maximum length of an ideal constellation vector for normalization. The $\mathrm{EVM_m}$ can be directly translated into a BER assuming the signal is impaired by additive white Gaussian noise only. [147] In our experiment we find a very good agreement between BER values calculated from the $\mathrm{EVM_m}$ and the measured BER, supporting our assumption that the channel is limited by Gaussian noise.

Fig. 4.4 shows constellation diagrams for the various generated signals. In Fig. 4.4(a)-(d), received QPSK constellation diagrams at data rates between 30 GBd and 45 GBd are depicted. At 45 GBd the $\mathrm{EVM_m}$ amounts to 23% and the measured BER is 1.5×10^{-5}, well below the limit of 4.5×10^{-3} for second-generation hard-decision forward error correction (FEC) with 7% overhead. [148] At 40 GBd the number of measured errors was not sufficient for a reliable BER estimation. At symbol rates of 35 GBd and below, the QPSK signals can be considered error free: No errors were measureable, and the $\mathrm{EVM_m}$ corresponds to a BER well below 1×10^{-9}. The constellation diagrams for 16QAM are depicted in Fig. 4.4(e)-(g). 16QAM signaling is demonstrated up to a symbol rate of 40 GBd. At symbol rates of up to 35 GBd, the measured BER is below the threshold for hard-decision FEC. For 40 GBd, the BER increases significantly, but is still below the threshold of 2.4×10^{-2} for third-generation soft-decision FEC with 20% overhead. [149] The results of the signal generation experiments are summarized in Fig. 4.5, where the $\mathrm{EVM_m}$ is plotted for different symbol

rates. The horizontal dashed lines in Fig. 4.5 indicate the calculated EVM_m [147] of the various BER threshold levels. For QPSK signals in Fig. 4.5(a), the dashed line corresponds to the BER of 1×10^{-9}, below that the signals can be considered error free. This applies to the signals measured at 30 and 35 GBd. All other measured QPSK signals are well below the hard-decision FEC limit which corresponds to an EVM_m of 38.3% and is outside the scale of the vertical axis. For 16QAM signals in Fig. 4.5(b), the horizontal lines indicate the EVM_m corresponding to the BER thresholds for hard-decision and soft-decision FEC, requiring 7% and 20% overhead, respectively. For symbol rates up to 35 GBd the EVM_m is below the threshold for hard-decision FEC; for 40 GBd it is still below the soft-decision threshold, consistent with the directly measured BER indicated in Fig. 4.4(e)-(g). Using 35 GBd 16QAM signals with hard-decision FEC, the line rate amounts to 140 Gb/s, and the net data rate amounts to 130.8 Gb/s. For 16QAM at 40 GBd, the line rate is 160 Gb/s-the highest value hitherto achieved by a silicon photonic modulator on a single polarization with measured BER figures comparable to those achieved in reference experiments. [128] Taking into account the 20% overhead for soft-decision FEC coding, the net data rate amounts to the record value of 133.3 Gb/s. The signal quality in the 40 GBd experiment is limited by the device bandwidth of 18 GHz. We expect that by optimization of the waveguide geometry and of the doping profile in the slabs, the bandwidth of future SOH devices can be significantly increased [140], leading to considerably lower BER.

When using a short SOH modulator at low symbol rates, the device can be operated without a terminal resistance and hence treated as a lumped capacitive load. [25] This is not possible for the high-speed data signals investigated here, for which the symbol duration is of the same order of magnitude as the propagation delay of the RF wave in the device. In this case, we need to model the modulator as a transmission line with a 50 Ω wave impedance, which is fed by a 50 Ω probe and terminated by a matched 50 Ω resistor, Fig. 4.6. This configuration is equivalent to a single 50 Ω load resistor, which is directly connected to the drive amplifier. The power consumption of a single MZM is then given by the power dissipation in this resistor. The output port of the drive amplifier is represented by an ideal voltage source with an internal generator impedance of 50 Ω. The energy per bit for the IQ modulator is obtained by adding the power consumptions of the two MZM and dividing by

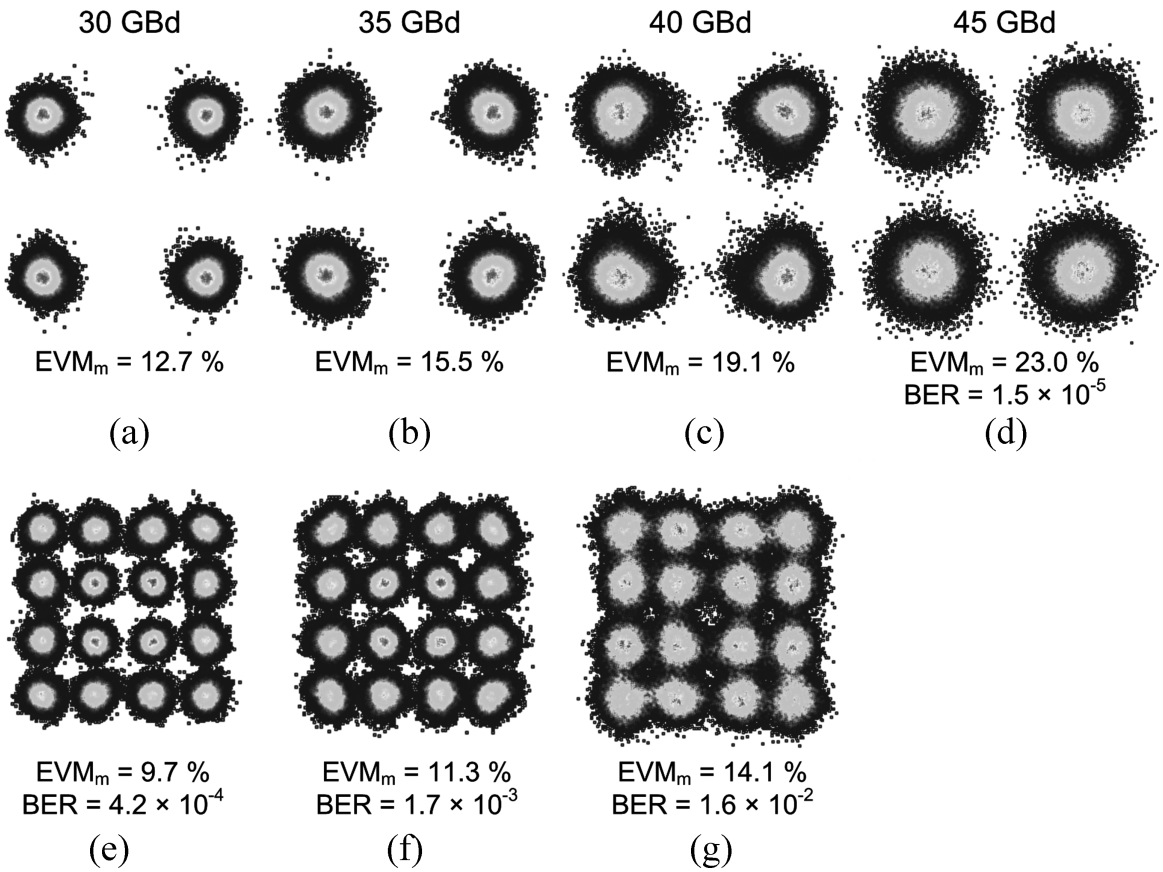

Figure 4.4: Optical constellation diagrams. (a)-(d) QPSK signals at 30, 35, 40, and 45 GBd. No bit errors were detected within our record length of 62.5 Îijs for symbol rates of 30 and 35 GBd, and the EVM_m indicate error free signals with BER $<$ 10âĹŠ9. QPSK signals at 40 and 45 GBd are well below the threshold for hard-decision FEC with 7% overhead. At 40 GBd the number of measured errors was not sufficient for a reliable BER estimation, at 45 GBd the measured BER amounts to 1.5 ÃŮ 10-5. (e)-(g) 16QAM signals for 30, 35, and 40 GBd. At data rates of up to 35 GBd the measured BER is below the hard-decision FEC threshold. For 40 GBd 16QAM signals, the BER is below the threshold for soft-decision FEC with 20% overhead.

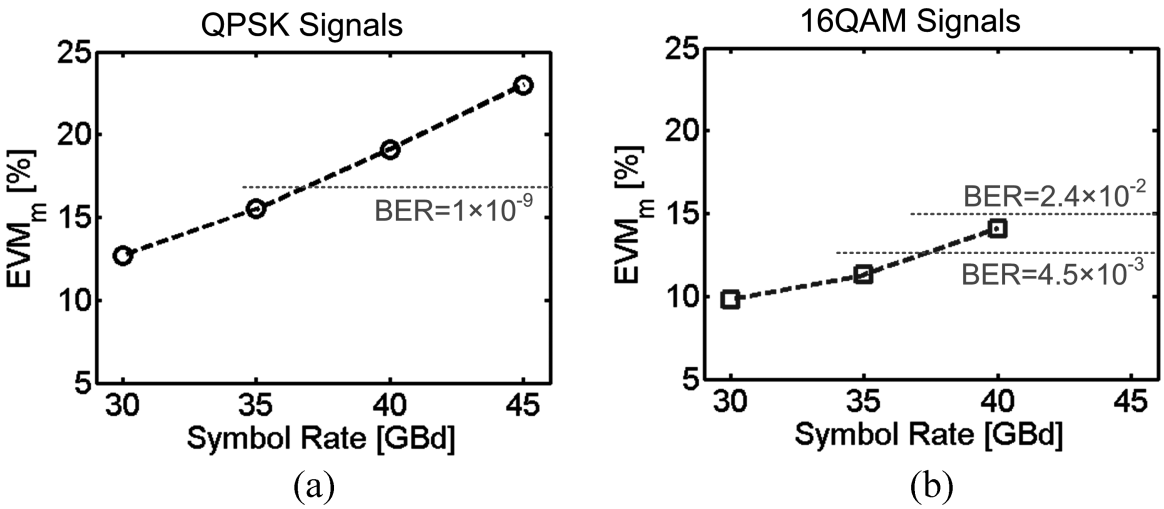

Figure 4.5: EVM_m plotted over the symbol rate, in red the corresponding BER [5] is indicated. (a) Plot for QPSK signals. Up to 35 GBd the signal can be considered error free with a corresponding BER $< 10^9$. The BER limit for hard-decision FEC corresponds to an EVM_m of 38.3%, outside the range of the plot. (b) Plot for 16QAM signals. The horizontal dashed lines indicate the EVM_m that correspond to the BER thresholds for soft-decision and hard-decision FEC in the case of 16QAM.

the total data rate. For 16QAM generation, the electrical drive signal for each MZM consists of two amplitude levels, which differ by a factor of 1/3. Assuming equal probability of the various symbols, the mean power consumption for each MZM can be calculated by averaging over the dissipated power of both amplitude levels. The energy per bit $W_{bit,16QAM}$ is then obtained by taking into account the power consumption of both MZM and by dividing by the data rate. Denoting the peak-to-peak voltages at the input of the $R = 50\ \Omega$ device as U_d, this leads to

$$W_{\mathrm{bit,16QAM}} = 2 \times \frac{1}{2}\left[\left(\frac{U_\mathrm{d}}{2}\right)^2 \frac{1}{R} + \left(\frac{1}{3}\frac{U_\mathrm{d}}{2}\right)^2 \frac{1}{R}\right] \frac{1}{r_{\mathrm{16QAM}}}. \tag{4.1}$$

For $U_d = 1.80\ V$ and a data rate of r_{16QAM} Gb/s, the energy consumption of the modulator is hence found to be 113 fJ/bit. This is one magnitude below current all-silicon 16QAM modulators [128], but still significantly higher than the energy consumption of a 28 GBd, 16QAM SOH device, for which 19 fJ/bit have been demonstrated. [138] It is the goal of ongoing research activity to further decrease the power consumption at high symbol

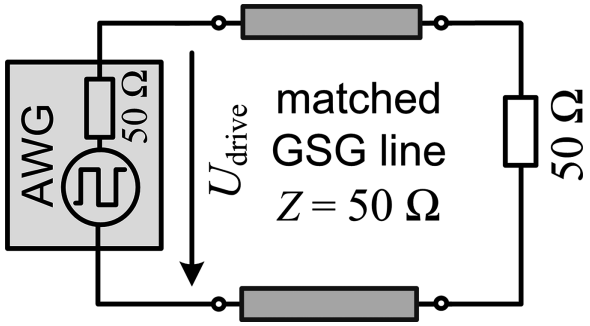

Figure 4.6: Equivalent-circuit diagram of one MZM for calculation of the energy consumption. The AWG which drives the MZM is represented by an ideal voltage source and an internal resistance of 50 Ω. The GSG line of the MZM is matched to the 50 Ω output of the DAC and terminated by an external 50 Ω impedance. To estimate the energy consumption, the transmission line and its termination is replaced by an equivalent resistor of $R = 50\ \Omega$.

rates.

4.5 Summary

We experimentally demonstrate that SOH integration is capable of boosting data rates and energy efficiency of silicon-based IQ modulators to unprecedented values. We show 16QAM modulation at 40 GBd, resulting in line rates (net data rates) of 160 Gb/s (133.3 Gb/s), and QPSK modulation at 45 GBd, leading to 90 Gb/s (84 Gb/s). For 16QAM, the energy consumption is as low as 113 fJ/bit-an order of magnitude below that of comparable all-silicon devices.

This work was supported by the European Research Council (ERC Starting Grant "EnTeraPic," 280145), the Alfried Krupp von Bohlen und Halbach Foundation, the EU-FP7 Projects PhoxTroT and BigPipes, the Helmholtz International Research School for Teratronics (HIRST), the Karlsruhe School of Optics and Photonics (KSOP), the Karlsruhe Nano-Micro Facility (KNMF), and the Initiative and Networking Fund of the Helmholtz Association. This work was also supported by the National Science Foundation (DMR-0905686, DMR-0120967, DMR-1303080) and by the Air Force Office of Scientific Research (FA9550-09-1-0682).

BIBLIOGRAPHY

[1] Wenwei Jin, Peter V. Johnston, Delwin L Elder, Karl T. Manner, Kerry E. Garrett, Werner Kaminsky, Ruimin Xu, Bruce H Robinson, and Larry Dalton. Structure-function relationship exploration for enhanced thermal stability and electro-optic activity in monolithic organic nlo chromophores. *J. Mater. Chem. C*, pages –, 2016.

[2] Wenwei Jin, Peter V. Johnston, Delwin L. Elder, Andreas F. Tillack, Benjamin C. Olbricht, Jinsheng Song, Philip J. Reid, Ruimin Xu, Bruce H. Robinson, and Larry R. Dalton. Benzocyclobutene barrier layer for suppressing conductance in nonlinear optical devices during electric field poling. *Applied Physics Letters*, 104(24):–, 2014.

[3] M. Lauermann, S. Wolf, P.C. Schindler, R. Palmer, S. Koeber, D. Korn, L. Alloatti, T. Wahlbrink, J. Bolten, M. Waldow, M. Koenigsmann, M. Kohler, D. Malsam, D.L. Elder, P.V. Johnston, N. Phillips-Sylvain, P.A. Sullivan, L.R. Dalton, J. Leuthold, W. Freude, and C. Koos. 40 gbd 16qam signaling at 160 gb/s in a silicon-organic hybrid modulator. *Lightwave Technology, Journal of*, 33(6):1210–1216, March 2015.

[4] W.H. Press. *Numerical Recipes: The Art of Scientific Computing*. Cambridge University Press, 1989.

[5] V. Pereverzev, Kim N. Gunnerson, Oleg V. Prezhdo, Philip A. Sullivan, Yi Liao, Benjamin C. Olbricht, Andrew J. P. Akelaitis, Alex K.-Y. Jen, , and Larry R. Dalton. Guest-host cooperativity in organic materials greatly enhances the nonlinear optical response. *The Journal of Physical Chemistry C*, 112(11):4355–4363, 2008.

[6] A. Chen and E. Murphy. *Broadband Optical Modulators Science, Technology, and Applications*. CRC Press: Boca Raton, 2012.

[7] G. Varrel. *Making Telecomms Work: From Technical Innovation to Commercial Success*. Wiley: West Sussex, 1993.

[8] R. Blum. *Characterization and Applications of Polymers with Variable Refractive Index for Components in Optical Telecommunications. Ph.D. Thesis*. Vom Promotionsausschuss der Technischen Universitat Hamburg-Harburg, 2003.

[9] J. Nellist. *Understanding Telecommunications and Lightwave Systems: An Entry-Level Guide*. Wiley: Piscataway, 2002.

[10] Md.) Naval Ordnance Laboratory, (White Oak and E.H. Winkler. *Analytical studies of the Mach-Zehnder interferometer*. Number v. 1-2 in Report (Naval Ordnance Laboratory (White Oak, Md.))). U.S. Dept. of Commerce, Office of Technical Services, 1947.

[11] K. B. Cooper and M. D. Gallagher. A nation online: Entering the broadband age, aug 2004. http://www.ntia.doc.gov/report/2004/nation-online-entering-broadband-age, (accessed August 30th 2013).

[12] L. Dalton. Revisiting organic optical nonlinearity leads to a new class of materials. SPIE Newsroom.

[13] C. C. Teng and H. T. Man. Simple reflection technique for measuring the electrooptic coefficient of poled polymers. *Applied Physics Letters*, 56(18):1734–1736, 1990.

[14] Paresh Chandra Ray and Puspendu Kumar Das. Influence of poling methods on the orientational dynamics of 2-methyl-4-nitro-aniline in poly(methyl methacrylate) studied by second harmonic generation. *European Polymer Journal*, 32(1):51 – 55, 1996.

[15] Martin Sprave, Robert Blum, and Manfred Eich. High electric field conduction mechanisms in electrode poling of electro-optic polymers. *Applied Physics Letters*, 69(20):2962–2964, 1996.

[16] S. Kurtz and T. Perry. A powder technique for the evaluation of nonlinear optical materials. 1968, 39, 3798.

[17] J. Gott. Effect of molecular structure on optical second-harmonic generation from organic crystals. 1971, 4, 116.

[18] David J. Williams. Organic polymeric and non-polymeric materials with large optical nonlinearities. *Angewandte Chemie International Edition in English*, 23(9):690–703, 1984.

[19] K. D. Singer, J. E. Sohn, and S. J. Lalama. Second harmonic generation in poled polymer films. *Applied Physics Letters*, 49(5):248–250, 1986.

[20] C. Zhang. *Novel Phenylpolyene-Bridged Second-Order Nonlinear Optical Chromophores and New Thermally Stable Polyurethanes for Electro-Optic Applications.* PhD thesis, 1999.

[21] B. Olbricht. Characterization and processing of organic nonlinear optical materials using ellipsometric, waveguiding, and absorption spectroscopy techniques, 2010.

[22] S. Benight. Nanoengineering of soft matter interactions in organic electro-optic materials. phd. thesis, 2011.

[23] Jingdong Luo, Su Huang, Yen-Ju Cheng, Tae-Dong Kim, Zhengwei Shi, Xing-Hua Zhou, and Alex K.-Y. Jen. Phenyltetraene-based nonlinear optical chromophores with enhanced chemical stability and electrooptic activity. *Organic Letters*, 9(22):4471–4474, 2007.

[24] Larry R. Dalton, Philip A. Sullivan, and Denise H. Bale. Electric field poled organic electro-optic materials: State of the art and future prospects. *Chemical Reviews*, 110(1):25–55, 2010. PMID: 19848381.

[25] Sebastian Koeber, Robert Palmer, Matthias Lauermann, Wolfgang Heni, Delwin L Elder, Dietmar Korn, Markus Woessner, Luca Alloatti, Swen Koenig, Philipp C Schindler, Hui Yu, Wim Bogaerts, Larry R Dalton, Wolfgang Freude, Juerg Leuthold, and Christian Koos. Femtojoule electro-optic modulation using a silicon-organic hybrid device. *Light Sci Appl*, 4:e255, Feb 2015.

[26] P. Sullivan. Theory guided design and molecular engineering of organic materials for enhanced second-order nonlinear optical properties. ph.d. thesis, 2006.

[27] H. Wolfgang. Personal communication. 2016.

[28] Harry Figi, Mojca Jazbinšek, Christoph Hunziker, Manuel Koechlin, and Peter Günter. Electro-optic single-crystalline organic waveguides and nanowires grown from the melt. *Opt. Express*, 16(15):11310–11327, Jul 2008.

[29] I. V. Kosilkin, E. A. Hillenbrand, P. Tongwa, A. Fonari, J. Zazueta, M. S. Fonari, M. Antipin, L. R. Dalton, and T. Timofeeva. Synthesis, structure, thermal and nonlinear optical properties of a series of novel d-π-a chromophores with varying alkoxy substituents. *Journal of Molecular Structure*, 1006:356–365, December 2011.

[30] I. Kosilkin. Organic materials for electro-optic and optoelectronic applications: Understanding structure-property relationships., 2012.

[31] D.S. Chemla. *Nonlinear Optical Properties of Organic Molecules and Crystals*. Number v. 1. Elsevier Science, 2012.

[32] L.R. Dalton, P. Günter, M. Jazbinsek, O.P. Kwon, and P.A. Sullivan. *Organic Electro-Optics and Photonics: Molecules, Polymers and Crystals*. Cambridge University Press, 2015.

[33] Paresh Chandra Ray. Size and shape dependent second order nonlinear optical properties of nanomaterials and their application in biological and chemical sensing. *Chemical Reviews*, 110(9):5332–5365, 2010. PMID: 20469927.

[34] Colin V. McLaughlin, L. Michael Hayden, Brent Polishak, Su Huang, Jingdong Luo, Tae-Dong Kim, and Alex K.-Y. Jen. Wideband 15thz response using organic electro-optic polymer emitter-sensor pairs at telecommunication wavelengths. *Applied Physics Letters*, 92(15), 2008.

[35] Yannick Salamin, Wolfgang Heni, Christian Haffner, Fedoryshyn, Claudia Hoessbacher, Romain Bonjour, Marco Zahner, David Hillerkuss, Pascal Leuchtmann, Delwin L. Elder, Larry R. Dalton, Christian Hafner, and Juerg Leuthold. Direct conversion of free space millimeter waves to optical domain by plasmonic modulator antenna. *Nano Letters*, 15(12):8342–8346, 2015. PMID: 26570995.

[36] Jingdong Luo, Su Huang, Zhengwei Shi, Brent M. Polishak, Xing-Hua Zhou, and Alex K-Y. Jen. Tailored organic electro-optic materials and their hybrid systems for device applications. *Chemistry of Materials*, 23(3):544–553, 2011.

[37] C. Haffner, W. Heni, Y. Fedoryshyn, J. Niegemann, A. Melikyan, D. L. Elder, B. Baeuerle, Y. Salamin, A. Josten, U. Koch, C. Hoessbacher, F. Ducry, L. Juchli, A. Emboras, D. Hillerkuss, M. Kohl, L. R. Dalton, C. Hafner, and J. Leuthold. All-plasmonic mach-zehnder modulator enabling optical high-speed communication at the microscale. *Nature Photonics*, 9:525–528, 2015.

[38] Kenneth D. Singer, Mark G. Kuzyk, and John E. Sohn. Second-order nonlinear-optical processes in orientationally ordered materials: relationship between molecular and macroscopic properties. *J. Opt. Soc. Am. B*, 4(6):968–976, Jun 1987.

[39] A. W. Harper, S. Sun, L. R. Dalton, S. M. Garner, A. Chen, S. Kalluri, W. H. Steier, and B. H. Robinson. Translating microscopic optical nonlinearity into macroscopic optical nonlinearity: the role of chromophore chromophore electrostatic interactions. *J. Opt. Soc. Am. B*, 15(1):329–337, Jan 1998.

[40] B. H. Robinson and L. R. Dalton. Monte carlo statistical mechanical simulations of the competition of intermolecular electrostatic and poling-field interactions in defining macroscopic electro-optic activity for organic chromophore/polymer materials. *The Journal of Physical Chemistry A*, 104(20):4785–4795, 2000.

[41] C. Weimann, P. C. Schindler, R. Palmer, S. Wolf, D. Bekele, D. Korn, J. Pfeifle, S. Koeber, R. Schmogrow, L. Alloatti, D. Elder, H. Yu, W. Bogaerts, L. R. Dalton, W. Freude, J. Leuthold, and C. Koos. Silicon-organic hybrid (soh) frequency comb sources for terabit/s data transmission. *Opt. Express*, 22(3):3629–3637, Feb 2014.

[42] M. Lauermann, R. Palmer, S. Koeber, P. C. Schindler, D. Korn, T. Wahlbrink, J. Bolten, M. Waldow, D. L. Elder, L. R. Dalton, J. Leuthold, W. Freude, and C. Koos. Low-power silicon-organic hybrid (soh) modulators for advanced modulation formats. *Opt. Express*, 22(24):29927–29936, Dec 2014.

[43] A. Melikyan, K. Koehnle, M. Lauermann, R. Palmer, S. Koeber, S. Muehlbrandt, P. C. Schindler, D. L. Elder, S. Wolf, W. Heni, C. Haffner, Y. Fedoryshyn, D. Hillerkuss, M. Sommer, L. R. Dalton, D. Van Thourhout, W. Freude, M. Kohl, J. Leuthold, and C. Koos. Plasmonic-organic hybrid (poh) modulators for ook and bpsk signaling at 40 gbit/s. *Opt. Express*, 23(8):9938–9946, Apr 2015.

[44] W. Heni, C. Hoessbacher, C. Haffner, Y. Fedoryshyn, B. Baeuerle, A. Josten, D. Hillerkuss, Y. Salamin, R. Bonjour, A. Melikyan, M. Kohl, D. L. Elder, L. R. Dalton, C. Hafner, and J. Leuthold. High speed plasmonic modulator array enabling dense optical interconnect solutions. *Opt. Express*, 23(23):29746–29757, Nov 2015.

[45] Tae-Dong Kim, Jae-Wook Kang, Jingdong org, Sei-Hum Jang, Jae-Won Ka, Neil Tucker, Jason B. Benedict, Larry R. Dalton, Tomoko Gray, Rene M. Overney, Dong Hun Park, Warren N. Herman, and Alex K.-Y. Jen. Ultralarge and thermally stable electro-optic activities from supramolecular self-assembled molecular glasses. *Journal of the American Chemical Society*, 129(3):488–489, 2007.

[46] Larry R. Dalton, Stephanie J. Benight, Lewis E. Johnson, Daniel B Knorr, Ilya Kosilkin, Bruce E. Eichinger, Bruce H. Robinson, Alex K.-Y. Jen, and Rene M. Overney. Systematic nanoengineering of soft matter organic electro-optic materials. *Chemistry of Materials*, 23:430–445, 2011.

[47] Stephanie J. Benight, Daniel B. Knorr, Lewis E. Johnson, Philip A. Sullivan, David Lao, Jianing Sun, Lakshmi S. Kocherlakota, Arumugasamy Elangovan, Bruce H. Robinson, Rene M. Overney, and Larry R. Dalton. Nano-engineering lattice dimensionality for a soft matter organic functional material. *Advanced Materials*, 24(24):3263–3268, 2012.

[48] Delwin L. Elder, Stephanie J. Benight, Jinsheng Song, Bruce H. Robinson, and Larry R. Dalton. Matrix-assisted poling of monolithic bridge-disubstituted organic nlo chromophores. *Chemistry of Materials*, 26(2):872–874, 2014.

[49] Xing-Hua Zhou, Jingdong Luo, Su Huang, Tae-Dong Kim, Zhengwei Shi, Yen-Ju Cheng, Sei-Hum Jang, Daniel B. Knorr, Rene M. Overney, and Alex K.-Y. Jen. Supramolecular self-assembled dendritic nonlinear optical chromophores: Fine-tuning of arene-perfluoroarene interactions for ultralarge electro-optic activity and enhanced thermal stability. *Advanced Materials*, 21(19):1976–1981, 2009.

[50] Raluca Dinu, Dan Jin, Guomin Yu, Baoquan Chen, Diyun Huang, Hui Chen, Anna Barklund, Eric Miller, Cailin Wei, and Jeevan Vemagiri. Environmental stress testing of electro–optic polymer modulators. *J. Lightwave Technol.*, 27(11):1527–1532, Jun 2009.

[51] Cheng Zhang, Larry R. Dalton, Min-Cheol Oh, Hua Zhang, and William H. Steier. Low v_π electrooptic modulators from cld-1: Chromophore design and synthesis, material processing, and characterization. *Chemistry of Materials*, 13(9):3043–3050, 2001.

[52] Tae-Dong Kim, Jingdong Luo, Yen-Ju Cheng, Zhengwei Shi, Steven Hau, Sei-Hum Jang, Xing-Hua Zhou, Yanqing Tian, Brent Polishak, Su Huang, Hong Ma, Larry R. Dalton, and Alex K.-Y. Jen. Binary chromophore systems in nonlinear optical dendrimers and polymers for large electrooptic activities. *The Journal of Physical Chemistry C*, 112(21):8091–8098, 2008.

[53] Scott R. Hammond, Olivier Clot, Kimberly A. Firestone, Denise H. Bale, David Lao, Marnie Haller, Gregory D. Phelan, Brenden Carlson, Alex K.-Y. Jen, Philip J. Reid, and Larry R. Dalton. Site-isolated electro-optic chromophores based on substituted 2,2'-bis(3,4-propylenedioxythiophene) π-conjugated bridges. *Chemistry of Materials*, 20(10):3425–3434, 2008.

[54] Zhong'an Li, Trenton R. Ensley, Honghua Hu, Yadong Zhang, Sei-Hum Jang, Seth R. Marder, David J. Hagan, Eric W. Van Stryland, and Alex K.-Y. Jen. Conjugated polycyanines: A new class of materials with large third-order optical nonlinearities. *Advanced Optical Materials*, 3(7):900–906, 2015.

[55] Yen-Ju Cheng, Jingdong Luo, Su Huang, Xinghua Zhou, Zhengwei Shi, Tae-Dong Kim, Denise H. Bale, Satsuki Takahashi, Andrew Yick, Brent M. Polishak, Sei-Hum Jang, Larry R. Dalton, Philip J. Reid, William H. Steier, and Alex K.-Y. Jen. Donor-acceptor thiolated polyenic chromophores exhibiting large optical nonlinearity and excellent photostability. *Chemistry of Materials*, 20(15):5047–5054, 2008.

[56] F. Michelotti, E. Toussaere, R. Levenson, J. Liang, and J. Zyss. Real-time pole and probe assessment of orientational processes in electro-optic polymers. *Applied Physics Letters*, 67(19):2765–2767, 1995.

[57] D.H. Bale. *Nonlinear Optical Materials Characterization Studies Employing Photostability, Hyper-Rayleigh Scattering, and Electric Field Induced Second Harmonic G.* BiblioBazaar, 2012.

[58] A. F. Tillack. *Electro-Optic Material Design Criteria Derived from Condensed Matter Simulations Using the Level-of-Detail Coarse-Graining Approach.* UW, 2015.

[59] C. A. Walsh, D. M. Burland, V. Y. Lee, R. D. Miller, B. A. Smith, R. J. Twieg, and W. Volksen. Orientational relaxation in electric field poled guest-host and side-chain polymers below T_g. *Macromolecules*, 26(14):3720–3722, 1993.

[60] Takafumi Sato, Dong-Lin Jiang, , and Takuzo Aida. A blue-luminescent dendritic rod: Poly(phenyleneethynylene) within a light-harvesting dendritic envelope. *Journal of the American Chemical Society*, 121(45):10658–10659, 1999.

[61] J. N. Woodford, M. A. Pauley, , and C. H. Wang. Solvent dependence of the first molecular hyperpolarizability of p-nitroaniline revisited. *The Journal of Physical Chemistry A*, 101(11):1989–1992, 1997.

[62] O. K. Song, J. N. Woodford, , and C. H. Wang. Effects of two-photon fluorescence and polymerization on the first hyperpolarizability of an azobenzene dye. *The Journal of Physical Chemistry A*, 101(18):3222–3226, 1997.

[63] Joshua A. Davies, Arumugasamy Elangovan, Philip A. Sullivan, Benjamin C. Olbricht, Denise H. Bale, Todd R. Ewy, Christine M. Isborn, Bruce E. Eichinger, Bruce H. Robinson, Philip J. Reid, Xiaosong Li, and Larry R. Dalton. Rational enhancement of second-order nonlinearity: Bis-(4-methoxyphenyl)hetero-aryl-amino donor-based chromophores: Design, synthesis, and electrooptic activity. *Journal of the American Chemical Society*, 130(32):10565–10575, 2008. PMID: 18642806.

[64] Stephanie J. Benight, Lewis E. Johnson, Robin Barnes, Benjamin C. Olbricht, Denise H. Bale, Philip J. Reid, Bruce E. Eichinger, Larry R. Dalton, Philip A. Sullivan, and Bruce H. Robinson. Reduced dimensionality in organic electro-optic materials: Theory and defined order. *The Journal of Physical Chemistry B*, 114(37):11949–11956, 2010. PMID: 20731406.

[65] Y. H. Kuo, Jingdong Luo, W. H. Steier, and A. K. Y. Jen. Enhanced thermal stability of electrooptic polymer modulators using the diels-alder crosslinkable polymer. *IEEE Photonics Technology Letters*, 18(1):175–177, Jan 2006.

[66] T.-D. Kim, J. Luo, J.-W. Ka, S. Hau, Y. Tian, Z. Shi, N. M. , S.-H. Jang, J.-W. Kang, and A. K.-Y. Jen. Ultralarge and thermally stable electro-optic activities from diels-alder crosslinkable polymers containing binary chromophore systems. *Advanced Materials*, 18(22):3038–3042, 2006.

[67] Mehmet Atilla Tasdelen. Diels-alder "click" reactions: recent applications in polymer and material science. *Polym. Chem.*, 2:2133–2145, 2011.

[68] S. Li. Reverse synthetic methods for making organic non-linear optical materials, December 29 2005. US Patent App. 10/876,322.

[69] Jingdong Luo, Yen-Ju Cheng, Tae-Dong Kim, Steven Hau, Sei-Hum Jang, Zhengwei Shi, Xing-Hua Zhou, and Alex K-Y. Jen*. Facile synthesis of highly efficient phenyltetraene-based nonlinear optical chromophores for electrooptics. *Organic Letters*, 8(7):1387–1390, 2006. PMID: 16562898.

[70] C. G. Overberger, J. C. Salamone, and J. Sebenda. Organic chemistry of synthetic high polymers. robert w. lenz. interscience (wiley), new york, 1967. xvi + 837 pp., illus. *Science*, 159(3820):1224, 1968.

[71] orgsyn.org. Organic synthesis, 2015.

[72] Matthew C. Davis, Richard A. Hollins, and Brad Douglas. Synthesis of a thiophene-based nonlinear optical chromophore. *Synthetic Communications*, 36(23):3515–3523, 2006.

[73] Shanyi Guang, Shouchun Yin, Hongyao Xu, Weiju Zhu, Yachen Gao, and Yinlin Song. Synthesis and properties of long conjugated organic optical limiting materials with different /*pi*-electron conjugation bridge structure. *Dyes and Pigments*, 73(3):285 – 291, 2007.

[74] T. Baehr-Jones, M. Hochberg, Guangxi Wang, R. Lawson, Y. Liao, P. Sullivan, L. Dalton, A. Jen, and A. Scherer. Optical modulation and detection in slotted silicon waveguides. *Opt. Express*, 13(14):5216–5226, Jul 2005.

[75] Mohammad M. Mojtahedi, Mohammad Saeed Abaee, Mohammad Mehdi Zahedi, Mohammad R. Jalali, A. Wahid Mesbah, Werner Massa, Roholah Yaghoubi, and Mehdi Forouzani. Facile solvent-free synthesis and structural elucidation of styrylcyclohex-2-enone derivatives. *Monatshefte fur Chemie - Chemical Monthly*, 139(8):917–921, 2008.

[76] W. Clark Still, Michael Kahn, and Abhijit Mitra. Rapid chromatographic technique for preparative separations with moderate resolution. *The Journal of Organic Chemistry*, 43(14):2923–2925, 1978.

[77] E. J. Corey and A. Venkateswarlu. Protection of hydroxyl groups as tert-butyldimethylsilyl derivatives. *Journal of the American Chemical Society*, 94(17):6190–6191, 1972.

[78] Peter G. M. Wuts and Theodora W. Greene. *Greene's Protective Groups in Organic Synthesis*. Wiley Online Library: Books. Wiley, 2006.

[79] William S. Wadsworth. *Synthetic Applications of Phosphoryl-Stabilized Anions*. John Wiley & Sons, Inc., 2004.

[80] William S. Wadsworth and William D. Emmons. The utility of phosphonate carbanions in olefin synthesis. *Journal of the American Chemical Society*, 83(7):1733–1738, 1961.

[81] Jingdong Luo, Su Huang, Yen-Ju Cheng, Tae-Dong Kim, Zhengwei Shi, Xing-Hua Zhou, and Alex K.-Y. Jen*. Phenyltetraene-based nonlinear optical chromophores with enhanced chemical stability and electrooptic activity. *Organic Letters*, 9(22):4471–4474, 2007. PMID: 17902681.

[82] * Mingqian He, Thomas M. Leslie, , and John A. Sinicropi. α-hydroxy ketone precursors leading to a novel class of electro-optic acceptors. *Chemistry of Materials*, 14(5):2393–2400, 2002.

[83] Gaguik Melikian, Francis P. Rouessac, and Christian Alexandre. Synthesis of substituted dicyanomethylendihydrofurans. *Synthetic Communications*, 25(19):3045–3051, 1995.

[84] H. Meislich and S. Jasne. Reactions of substituted 5,5-di(r)(ar)-2-cyclohexenones. i. sn2 and sn2' reactions of 4-bromoisophorone. *The Journal of Organic Chemistry*, 40(18):2662–2666, 1975.

[85] Bouchra Rissafi, Noureddine Rachiqi, Ahmed El Louzi, Andre Loupy, Alain Petit, and Souad Fkih-Tetouani. Epoxyisophorone ring-opening: an efficient route for the introduction of functional groups at position 2 of isophorone. *Tetrahedron*, 57(14):2761 – 2768, 2001.

[86] Angela Altomare, Maria Cristina Burla, Mercedes Camalli, Giovanni Luca Cascarano, Carmelo Giacovazzo, Antonietta Guagliardi, Anna Grazia Giuseppina Moliterni, Giampiero Polidori, and Riccardo Spagna. *SIR*97: a new tool for crystal structure determination and refinement. *Journal of Applied Crystallography*, 32(1):115–119, Feb 1999.

[87] A. Altomare, G. Cascarano, C. Giacovazzo, and A. Guagliardi. Completion and refinement of crystal structures with *SIR*92. *Journal of Applied Crystallography*, 26(3):343–350, Jun 1993.

[88] G. M. Sheldrick. Program for the refinement of crystal structures. *University of Gottingen*, pages SHELXL–97, 1997.

[89] S. Mackay, C. Edwards, and A. Henderson. a computer program for the solution and refinement of crystal structures from diffraction data. *University of Glasgow*, 1997.

[90] D. Waasmaier and A. Kirfel. New analytical scattering-factor functions for free atoms and ions. *Acta Crystallographica Section A*, 51(3):416–431, May 1995.

[91] M. J. Frisch. Gaussian 09, revision d.01. *Computer Program*, 2013.

[92] Hisayoshi Iikura, Takao Tsuneda, Takeshi Yanai, and Kimihiko Hirao. A long-range correction scheme for generalized-gradient-approximation exchange functionals. *The Journal of Chemical Physics*, 115(8):3540–3544, 2001.

[93] Muneaki Kamiya, Hideo Sekino, Takao Tsuneda, and Kimihiko Hirao. Nonlinear optical property calculations by the long-range-corrected coupled-perturbed kohn-sham method. *The Journal of Chemical Physics*, 122(23), 2005.

[94] Su Huang, Tae-Dong Kim, Jingdong Luo, Steven K. Hau, Zhengwei Shi, Xing-Hua Zhou, Hin-Lap Yip, and Alex K.-Y. Jen. Highly efficient electro-optic polymers through improved poling using a thin TiO_2-modified transparent electrode. *Applied Physics Letters*, 96(24):–, 2010.

[95] Mark Lee, Howard E. Katz, Christoph Erben, Douglas M. Gill, Padma Gopalan, Joerg D. Heber, and David J. McGee. Broadband modulation of light by using an electro-optic polymer. *Science*, 298(5597):1401–1403, 2002.

[96] Alexander M. Sinyukov and L. Michael Hayden. Generation and detection of terahertz radiation with multilayered electro-optic polymer films. *Opt. Lett.*, 27(1):55–57, Jan 2002.

[97] Felipe A. Vallejo and L. Michael Hayden. Design of ultra-broadband terahertz polymer waveguide emitters for telecom wavelengths using coupled mode theory. *Opt. Express*, 21(5):5842–5858, Mar 2013.

[98] F. Fesharaki and Ke Wu. Band-pass non-tem mode traveling-wave electro-optical polymer modulator for millimeter-wave and terahertz application. *Lightwave Technology, Journal of*, 30(23):3586–3596, Dec 2012.

[99] Brent M. Polishak, Su Huang, Jingdong Luo, Zhengwei Shi, Xing-Hua Zhou, Albert Hsu, and Alex K.-Y. Jen. A triptycene-containing chromophore for improved temporal stability of highly efficient guest-host electrooptic polymers. *Macromolecules*, 44(6):1261–1265, 2011.

[100] Jingdong Luo, Xing-Hua Zhou, and Alex K.-Y. Jen. Rational molecular design and supramolecular assembly of highly efficient organic electro-optic materials. *J. Mater. Chem.*, 19:7410–7424, 2009.

[101] Tomoko Gray, Tae-Dong Kim, Jr. Daniel B. Knorr, Jingdong Luo, âĂą Alex K.-Y. Jen, and Rene M. Overney*. Mesoscale dynamics and cooperativity of networking dendronized nonlinear optical molecular glasses. *Nano Letters*, 8(2):754–759, 2008. PMID: 18171095.

[102] Robert Blum, Martin Sprave, Jurgen Sablotny, and Manfred Eich. High-electric-field poling of nonlinear optical polymers. *J. Opt. Soc. Am. B*, 15(1):318–328, Jan 1998.

[103] D. Vuillaume, C. Boulas, J. Collet, J. V. Davidovits, and F. Rondelez. Organic insulating films of nanometer thicknesses. *Applied Physics Letters*, 69(11):1646–1648, 1996.

[104] James P. Drummond, Stephen J. Clarson, John S. Zetts, F. Kenneth Hopkins, and Stephen J. Caracci. Enhanced electro-optic poling in guest-host systems using conductive polymer-based cladding layers. *Applied Physics Letters*, 74(3):368–370, 1999.

[105] Su Huang, Jingdong Luo, Hin-Lap Yip, Ali Ayazi, Xing-Hua Zhou, Michael Gould, Antao Chen, Tom Baehr-Jones, Michael Hochberg, and Alex K.-Y. Jen. Efficient poling of electro-optic polymers in thin films and silicon slot waveguides by detachable pyroelectric crystals. *Advanced Materials*, 24(10):OP42–OP47, 2012.

[106] Su Huang, Jingdong Luo, Zhian Jin, Xing-Hua Zhou, Zhengwei Shi, and Alex K.-Y. Jen. Enhanced temporal stability of a highly efficient guest-host electro-optic polymer through a barrier layer assisted poling process. *J. Mater. Chem.*, 22:20353–20357, 2012.

[107] Philip A. Sullivan and Larry R. Dalton. Theory-inspired development of organic electro-optic materials. *Accounts of Chemical Research*, 43(1):10–18, 2010. PMID: 19663413.

[108] M.J. Alam and D.C. Cameron. Preparation and characterization of TiO_2 thin films by sol-gel method. *Journal of TiO_2 and Technology*, 25(2):137–145, 2002.

[109] Ruchi Agrawal, Pramod Kumar, Subhasis Ghosh, and Ajit Kumar Mahapatro. Thickness dependence of space charge limited current and injection limited current in organic molecular semiconductors. *Applied Physics Letters*, 93(7):–, 2008.

[110] W.R. Salaneck, R.H. Friend, and J.L. Bredas. Electronic structure of conjugated polymers: consequences of electron-lattice coupling. *Physics Reports*, 319(6):231 – 251, 1999.

[111] Ying-Hung So, Phil E. Garrou, Jang-Hi Im, and Karou Ohba. *Benzocyclobutene-Based Polymers for Microelectronic Applications*, chapter 22, pages 279–293. 2004.

[112] V. Dentan, Y. Levy, M. Dumont, P. Robin, and E. Chastaing. Electrooptic properties of a ferroelectric polymer studied by attenuated total reflection. *Optics Communications*, 69(5-6):379 – 383, 1989.

[113] Benjamin C. Olbricht. r_{33} measurements were performed by teng-man at university of washington and by atr at university of delaware. *unpublished*, 2014.

[114] Tom Baehr-Jones, Boyan Penkov, Jingqing Huang, Phil Sullivan, Joshua Davies, Jocelyn Takayesu, Jingdong Luo, Tae-Dong Kim, Larry Dalton, Alex Jen, Michael Hochberg, and Axel Scherer. Nonlinear polymer-clad silicon slot waveguide modulator with a half wave voltage of 0.25v. *Applied Physics Letters*, 92(16):–, 2008.

[115] Michael E. Mills, Paul Townsend, Dan Castillo, Steve Martin, and Albert Achen. Benzocyclobutene (dvs-bcb) polymer as an interlayer dielectric (ild) material. *Microelectronic Engineering*, 33(1-4):327 – 334, 1997. Advanced Materials for Interconnections.

[116] James G. Grote, John S. Zetts, Robert L. Nelson, Frank K. Hopkins, Larry R. Dalton, Cheng Zhang, and William H. Steier. Effect of conductivity and dielectric constant on the modulation voltage for optoelectronic devices based on nonlinear optical polymers. *Optical Engineering*, 40(11):2464–2473, 2001.

[117] M. E. Mills, P. Townsend, D. Castillo, S Martin, and A. Achen. Benzocyclobutene (dvs-bcb) polymer as an interlayer dielectric (ild) material. *Microelectronic Engineering*, 33:327, 1997.

[118] J. Y. Kim, S. H. Kim, H.-H. Lee, K. Lee, W. Ma, X. Gong, and A. J. Heeger. New architecture for high-efficiency polymer photovoltaic cells using solution-based titanium oxide as an optical spacer. *Advanced Materials*, 18(5):572–576, 2006.

[119] M. Gratzel. Photoelectrochemical cells. *Nature*, 414:338–344, 2001.

[120] S. Rentenberger, A. Vollmer, E. Zojer, R. Schennach, and N. Koch. UvâĹŢozone treated au for air-stable, low hole injection barrier electrodes in organic electronics. *Journal of Applied Physics*, 100(5), 2006.

[121] Jason S. Orcutt, Benjamin Moss, Chen Sun, Jonathan Leu, Michael Georgas, Jeffrey Shainline, Eugen Zgraggen, Hanqing Li, Jie Sun, Matthew Weaver, Stevan Urošević, Miloš Popović, Rajeev J. Ram, and Vladimir Stojanović. Open foundry platform for high-performance electronic-photonic integration. *Opt. Express*, 20(11):12222–12232, May 2012.

[122] Peter J. Winzer. High-spectral-efficiency optical modulation formats. *J. Lightwave Technol.*, 30(24):3824–3835, Dec 2012.

[123] G. T. Reed, G. Mashanovich, F. Y. Gardes, and D. J. Thomson. Silicon optical modulators. *Nat Photon*, 4(8):518–526, Aug 2010.

[124] L. Liao, A. Liu, J. Basak, H. Nguyen, M. Paniccia, D. Rubin, Y. Chetrit, R. Cohen, and N. Izhaky. 40 gbit/s silicon optical modulator for highspeed applications. *Electronics Letters*, 43(22), Oct 2007.

[125] Junichi Fujikata, Jun Ushida, Takahiro Nakamura, Yu Ming-Bin, Zhu ShiYang, Ding Liang, Patrick Lo. Guo-Qiang, and Dim-Lee Kwong. 25 ghz operation of silicon optical modulator with projection mos structure. In *Optical Fiber Communication Conference*, page OMI3. Optical Society of America, 2010.

[126] Takeshi Baba, Suguru Akiyama, Masahiko Imai, Takeshi Akagawa, Masashi Takahashi, Naoki Hirayama, Hiroyuki Takahashi, Yoshiji Noguchi, Hideaki Okayama, Tsuyoshi Horikawa, and Tatsuya Usuki. 25-gbps operation of silicon p-i-n mach-zehnder optical modulator with 100-μm-long phase shifter. In *Conference on Lasers and Electro-Optics 2012*, page CF2L.3. Optical Society of America, 2012.

[127] Po Dong, Chongjin Xie, Lawrence L. Buhl, Young-Kai Chen, Jeffrey H. Sinsky, and Gregory Raybon. Silicon in-phase/quadrature modulator with on-chip optical equalizer. *J. Lightwave Technol.*, 33(6):1191–1196, Mar 2015.

[128] Po Dong, Xiang Liu, S. Chandrasekhar, L.L. Buhl, R. Aroca, and Young-Kai Chen. Monolithic silicon photonic integrated circuits for compact 100 plus gb/s coherent optical receivers and transmitters. *Selected Topics in Quantum Electronics, IEEE Journal of*, 20(4):150–157, July 2014.

[129] Vilson R. Almeida, Qianfan Xu, Carlos A. Barrios, and Michal Lipson. Guiding and confining light in void nanostructure. *Opt. Lett.*, 29(11):1209–1211, Jun 2004.

[130] C. Koos, J. Brosi, M. Waldow, W. Freude, and J. Leuthold. Silicon-on-insulator modulators for next-generation 100 gbit/s-ethernet. In *Optical Communication (ECOC), 2007 33rd European Conference and Ehxibition of*, pages 1–2, Sept 2007.

[131] Christian Koos, Luca Alloatti, Dietmar Korn, Robert Palmer, David Hillerkuss, Jingshi Li, Anna Barklund, Raluca Dinu, Joerg Wieland, Maryse Fournier, Jean-Marc Fedeli, Hui Yu, Wim Bogaerts, Pieter Dumon, Roel Baets, Wolfgang Freude, and Juerg Leuthhold. Silicon-organic hybrid (soh) electro-optical devices. In *Advanced Photonics*, page IWF1. Optical Society of America, 2011.

[132] L. Alloatti, D. Korn, R. Palmer, D. Hillerkuss, J. Li, A. Barklund, R. Dinu, J. Wieland, M. Fournier, J. Fedeli, H. Yu, W. Bogaerts, P. Dumon, R. Baets, C. Koos, W. Freude, and J. Leuthold. 42.7 gbit/s electro-optic modulator in silicon technology. *Opt. Express*, 19(12):11841–11851, Jun 2011.

[133] R. Palmer, S. Koeber, D.L. Elder, M. Woessner, W. Heni, D. Korn, M. Lauermann, W. Bogaerts, L. Dalton, W. Freude, J. Leuthold, and C. Koos. High-speed, low drive-voltage silicon-organic hybrid modulator based on a binary-chromophore electro-optic material. *Lightwave Technology, Journal of*, 32(16):2726–2734, Aug 2014.

[134] R. Palmer, L. Alloatti, D. Korn, P.C. Schindler, R. Schmogrow, W. Heni, S. Koenig, J. Bolten, T. Wahlbrink, M. Waldow, H. Yu, W. Bogaerts, P. Verheyen, G. Lepage, M. Pantouvaki, J. Van Campenhout, P. Absil, R. Dinu, W. Freude, C. Koos, and J. Leuthold. Silicon-organic hybrid mzi modulator generating ook, bpsk and 8-ask signals for up to 84 gbit/s. *Photonics Journal, IEEE*, 5(2):6600907–6600907, April 2013.

[135] D Korn, R Palmer, Hui Yu, PC Schindler, L Alloatti, M Baier, R Schmogrow, Wim Bogaerts, SK Selvaraja, G Lepage, M Pantouvaki, JMD Wouters, P Verheyen, J Van Campenhout, BQ Chen, Roel Baets, P Absil, R Dinu, C Koos, W Freude, and J Leuthold. Silicon-organic hybrid (soh) iq modulator using the linear electro-optic effect for transmitting 16qam at 112 gbit/s. *OPTICS EXPRESS*, 21(11):13219–13227, 2013.

[136] M. Lauermann, P.C. Schindler, S. Wolf, R. Palmer, S. Koeber, D. Korn, L. Alloatti, T. Wahlbrink, J. Bolten, M. Waldow, M. Koenigsmann, M. Kohler, D. Malsam, D.L. Elder, P.V. Johnston, N. Phillips-Sylvain, P.A. Sullivan, L.R. Dalton, J. Leuthold, W. Freude, and C. Koos. 40 gbd 16qam modulation at 160 gbit/s in a silicon-organic hybrid (soh) modulator. In *Optical Communication (ECOC), 2014 European Conference on*, pages 1–3, Sept 2014.

[137] R. Palmer, L. Alloatti, D. Korn, P.C. Schindler, M. Baier, J. Bolten, T. Wahlbrink, M. Waldow, R. Dinu, W. Freude, C. Koos, and J. Leuthold. Low power mach zehnder modulator in silicon-organic hybrid technology. *Photonics Technology Letters, IEEE*, 25(13):1226–1229, July 2013.

[138] M. Lauermann, R. Palmer, S. Koeber, P.C. Schindler, D. Korn, T. Wahlbrink, J. Bolten, M. Waldow, D.L. Elder, L.R. Dalton, J. Leuthold, W. Freude, and C. Koos. 16qam silicon-organic hybrid (soh) modulator operating with 0.6 vpp and 19 fj/bit at 112 gbit/s. In *Lasers and Electro-Optics (CLEO), 2014 Conference on*, pages 1–2, June 2014.

[139] L. Alloatti, M. Lauermann, C. SÃijrgers, C. Koos, W. Freude, and J. Leuthold. Optical absorption in silicon layers in the presence of charge inversion/accumulation or ion implantation. *Applied Physics Letters*, 103(5), 2013.

[140] Luca Alloatti, Robert Palmer, Sebastian Diebold, Kai Philipp Pahl, Baoquan Chen, Raluca Dinu, Maryse Fournier, Jean-Marc Fedeli, Thomas Zwick, Wolfgang Freude, Christian Koos, and Juerg Leuthold. 100[emsp14]ghz silicon-organic hybrid modulator. *Light Sci Appl*, 3:e173, May 2014. Original Article.

[141] Y. Enami, J. Luo, and A. K-Y. Jen. Short hybrid polymer/sol-gel silica waveguide switches with high in-device electro-optic coefficient based on photostable chromophore. *AIP Advances*, 1(4), 2011.

[142] Zhengwei Shi, Wenkel Liang, Jingdong Luo, Su Huang, Brent M. Polishak, Xiaosong Li, Todd R. Younkin, Bruce A. Block, and Alex K.-Y. Jen. Tuning the kinetics and energetics of diels-alder cycloaddition reactions to improve poling efficiency and thermal stability of high-temperature cross-linked electro-optic polymers. *Chemistry of Materials*, 22(19):5601–5608, 2010.

[143] D. Vermeulen, S. Selvaraja, P. Verheyen, G. Lepage, W. Bogaerts, P. Absil, D. Van Thourhout, and G. Roelkens. High-efficiency fiber-to-chip grating couplers realized using an advanced cmos-compatible silicon-on-insulator platform. *Opt. Express*, 18(17):18278–18283, Aug 2010.

[144] N. Lindenmann, G. Balthasar, D. Hillerkuss, R. Schmogrow, M. Jordan, J. Leuthold, W. Freude, and C. Koos. Photonic wire bonding: a novel concept for chip-scale interconnects. *Opt. Express*, 20(16):17667–17677, Jul 2012.

[145] N. Lindenmann, S. Dottermusch, M.L. Goedecke, T. Hoose, M.R. Billah, T.P. Onanuga, A. Hofmann, W. Freude, and C. Koos. Connecting silicon photonic circuits to multicore fibers by photonic wire bonding. *Lightwave Technology, Journal of*, 33(4):755–760, Feb 2015.

[146] Ran Ding, Tom Baehr-Jones, Woo-Joong Kim, Bryan Boyko, Richard Bojko, Alexander Spott, Andrew Pomerene, Craig Hill, Wesley Reinhardt, and Michael Hochberg. Low-loss asymmetric strip-loaded slot waveguides in silicon-on-insulator. *Applied Physics Letters*, 98(23), 2011.

[147] R. Schmogrow, B. Nebendahl, M. Winter, A. Josten, D. Hillerkuss, S. Koenig, J. Meyer, M. Dreschmann, M. Huebner, C. Koos, J. Becker, W. Freude, and J. Leuthold. Error vector magnitude as a performance measure for advanced modulation formats. *Photonics Technology Letters, IEEE*, 24(1):61–63, Jan 2012.

[148] F. Chang, K. Onohara, and T. Mizuochi. Forward error correction for 100 g transport networks. *Communications Magazine, IEEE*, 48(3):S48–S55, March 2010.

[149] Deyuan Chang, Fan Yu, Zhiyu Xiao, Yang Li, N. Stojanovic, Changsong Xie, Xiaozhong Shi, Xiaogeng Xu, and Qianjin Xiong. Fpga verification of a single qc-ldpc code for 100 gb/s optical systems without error floor down to ber of 10^{-15}. In *Optical Fiber Communication Conference and Exposition (OFC/NFOEC), 2011 and the National Fiber Optic Engineers Conference*, pages 1–3, March 2011.